

Femtosecond diffraction and dynamic high pressure science

Cite as: J. Appl. Phys. **132**, 080902 (2022); <https://doi.org/10.1063/5.0089388>

Submitted: 25 February 2022 • Accepted: 29 July 2022 • Published Online: 29 August 2022

 Justin S. Wark,  Malcolm I. McMahon and  Jon H. Eggert



View Online



Export Citation



CrossMark

ARTICLES YOU MAY BE INTERESTED IN

[Femtosecond diffraction studies of the sodium chloride phase diagram under laser shock compression](#)

Journal of Applied Physics **132**, 085901 (2022); <https://doi.org/10.1063/5.0094894>

[Experimental and theoretical examination of shock-compressed copper through the fcc to bcc to melt phase transitions](#)

Journal of Applied Physics **132**, 075902 (2022); <https://doi.org/10.1063/5.0088607>

[Quantitative measurements of density in shock-compressed silver up to 330 GPa using x-ray diffraction](#)

Journal of Applied Physics **131**, 015901 (2022); <https://doi.org/10.1063/5.0072208>

Journal of
Applied Physics

Special Topics Open for Submissions

Learn More

Femtosecond diffraction and dynamic high pressure science

Cite as: J. Appl. Phys. **132**, 080902 (2022); doi: [10.1063/5.0089388](https://doi.org/10.1063/5.0089388)

Submitted: 25 February 2022 · Accepted: 29 July 2022 ·

Published Online: 29 August 2022



Justin S. Wark,^{1,a)}  Malcolm I. McMahon,²  and Jon H. Eggert³ 

AFFILIATIONS

¹Department of Physics, Clarendon Laboratory, University of Oxford, Parks Road, Oxford OX1 3PU, United Kingdom

²SUPA, School of Physics and Astronomy, and Centre for Science at Extreme Conditions, The University of Edinburgh, Edinburgh EH9 3FD, United Kingdom

³Lawrence Livermore National Laboratory, 7000 East Avenue, Livermore, California 94550, USA

^{a)}Author to whom correspondence should be addressed: justin.wark@physics.ox.ac.uk

ABSTRACT

Solid-state material at high pressure is prevalent throughout the Universe, and an understanding of the structure of matter under such extreme conditions, gleaned from x-ray diffraction, has been pursued for the best part of a century. The highest pressures that can be reached to date (2 TPa) in combination with x-ray diffraction diagnosis have been achieved by dynamic compression via laser ablation [A. Lazicki *et al.*, *Nature* **589**, 532–535 (2021)]. The past decade has witnessed remarkable advances in x-ray technologies, with novel x-ray Free-Electron-Lasers (FELs) affording the capacity to produce high quality single-shot diffraction data on timescales below 100 fs. We provide a brief history of the field of dynamic compression, spanning from when the x-ray sources were almost always laser-plasma based, to the current state-of-the-art diffraction capabilities provided by FELs. We give an overview of the physics of dynamic compression, diagnostic techniques, and the importance of understanding how the rate of compression influences the final temperatures reached. We provide illustrative examples of experiments performed on FEL facilities that are starting to give insight into how materials deform at ultrahigh strain rates, their phase diagrams, and the types of states that can be reached. We emphasize that there often appear to be differences in the crystalline phases observed between the use of static and dynamic compression techniques. We give our perspective on both the current state of this rapidly evolving field and some glimpses of how we see it developing in the near-to-medium term.

© 2022 Author(s). All article content, except where otherwise noted, is licensed under a Creative Commons Attribution (CC BY) license (<http://creativecommons.org/licenses/by/4.0/>). <https://doi.org/10.1063/5.0089388>

I. INTRODUCTION AND BACKGROUND

A. Background

Over the past decade, we have witnessed impressive developments in both dynamic high-pressure science and x-ray physics that when combined provide future potential to create, study, and diagnose the structure and properties of matter in the laboratory under unprecedented conditions of pressure and temperature. Previously unexplored regimes of the phase diagram will become accessible, giving rise to the opportunity to probe materials in the laboratory that have hitherto only existed deep within planets other than our own, be they within our own solar system or beyond.¹ As well as the final states achieved, the deformation pathways that materials take to reach these conditions, and which are of interest in their own right,

will also be amenable to interrogation and indeed need to be understood if the results of dynamic compression experiments are ultimately going to be meaningfully related to planetary systems.

The pertinent development in dynamic high-pressure science has been the crafting of techniques, based on short-pulse (typically nanosecond) laser-ablation, that afford in a reasonably controlled way, the creation of high-pressure states of solid-state matter beyond the TPa (~10 Mbar) regime. We note at the outset of our discussions that it is important to recognize that the rate at which the sample (usually a solid foil, of order micrometers to tens-of-micrometers thick) is dynamically loaded plays a pivotal role in determining its conditions at peak pressure: if the compression wave formed by the nanosecond laser ablation process is allowed to steepen into a shock, then the sample's state will lie on



FIG. 2. An aerial view of the Linac Coherent Light Source (LCLS) at SLAC National Accelerator Laboratory showing the location of the various parts of the machine such as the injector, linac, undulator, x-ray transport, and the experimental hall. Credit: SLAC National Accelerator Laboratory.

between shock and ramp compression are less pronounced: indeed, to date the vast majority of dynamical compression experiments at FELs have utilized shock compression. We discuss below developments of these facilities to attain the multi-TPa regime via ramp compression at repetition rates such that many thousands of individual compression-diffraction experiments can be performed in a reasonable timeframe. The scientific opportunities that such facilities will offer motivate much of the thinking behind our discussions of future directions.

Within this paper, we provide our perspective on how this area of research has developed over the past decade in the context of both the development of ramp-compression techniques and the rapid development of FELs, what we perceive to be some of the major science drivers, and how we view prospects for future developments. Given the huge breadth of the field of high energy density science, we will restrict our comments to studies of matter in the solid (and occasionally molten) state. While hot, dense plasmas can also be created by both high-power optical and x-ray illumination,¹⁴ their study requires a description of matter from a different physical perspective, which is beyond the scope of this work. As the title of the paper suggests, we restrict our discussion almost exclusively to diagnosis via x-ray diffraction, though briefly mention other x-ray techniques that may aid in ascertaining the temperature of the dynamically compressed matter.

The paper is laid out in the following manner. Following this brief introduction, in Sec. I B, we place the field of femtosecond

diffraction using FELs as a tool for the study of matter under high pressure into a broader historical perspective of dynamical compression of matter combined with diffraction in general, taking care to highlight those experiments where shock compression was employed, and those more recent ones where the material was kept closer to an isentrope. In Sec. II, we provide an outline of the basic physics of how dynamic pressure is applied via laser ablation, measured via interferometric techniques, and briefly discuss the types of targets studied. Following this in Sec. III, we give a brief overview of work in this field to date, before in Sec. IV outlining what we perceive to be at least some of the major outstanding problems that need to be addressed in the future. Much of our thinking is based, as noted above, on the need to understand the heating mechanisms that pertain, and temperatures that can be reached, via these dynamic compression techniques. Given that the rate at which pressure is applied in these experiments plays a crucial role in the final state of the material, Sec. IV A concentrates on the basic pertinent physics, as presently understood, between dynamically compressing samples so rapidly that a shock wave is produced, and compressing them with a temporal pressure profile that, while still rapid (nanosecond timescales), is sufficiently slow that the compression path is cooler, lies closer to the isentrope, and potentially keeps the sample solid even at ultrahigh pressures. After presenting our perspectives, we note in Sec. V that future directions will rely to a large degree on further technical developments in FEL and driver technology. We summarize and conclude in Sec. VI.

B. Historical perspective

The beginning of the study of solid-state matter under high pressure in a controlled way under static conditions is usually ascribed to the pioneering and Nobel prize winning work of Percy Bridgman,¹⁵ whose invention of a novel type of seal, which ensured that the pressure in the gasket always exceeded that in the sample under pressure (thus leading to self-sealing), immediately enabled him to subject samples to pressures up to several GPa, and ultimately 40 GPa.^{16,17} The so-called static high-pressure research has advanced significantly since those early studies, with almost all work at pressures above several tens of GPa now making use of Diamond Anvil Cells,^{18–20} conventional forms of which can reach pressures of order 400 GPa,²¹ while novel anvil shapes and two-stage forms can now achieve pressures of 500–600 GPa^{22,23} and close to and above 1 TPa,^{24–26} respectively. On the other hand, the rise of dynamic compression of solids can in a large part be traced back to the work performed during the second world war at Los Alamos National Laboratory, and independently in Russia,^{27,28} which provided scientists with an unprecedented capability to shock-load materials explosively—but precisely—to several 10 s of GPa, and accurately to diagnose their pressure and density. The decade following the war saw the publication of a number of seminal papers,^{29–32} with these works introducing the scientific community at large to this new branch of physics including the review by Rice *et al.*³³ in 1958, and the classic texts of Zel'dovich and Raizer³⁴ introducing the scientific community at large to this new branch of physics.

Importantly, the pressures reached under such dynamic (shock) compression could be gauged accurately because the material conditions in front of, and directly behind, a shock front must be related by the simple conservation equations derived in the 19th century by Rankine and Hugoniot.^{35,36} These equations, that express conservation of mass, momentum, and energy link conditions upstream of the shock (with subscript 0), to those behind the shock front,

$$\rho_0 U_S = \rho(U_S - U_P), \quad (1)$$

$$\sigma_{zz} - \sigma_0 = \rho_0 U_S U_P, \quad (2)$$

$$e - e_0 = \frac{1}{2}(\sigma_{zz} + \sigma_0) \frac{\rho \rho_0}{\rho - \rho_0}, \quad (3)$$

where ρ is the density, U_S and U_P are the shock and particle velocity, respectively, σ_{zz} is the longitudinal stress, and e is the energy per unit mass. As one knows the initial density, stress, and energy, these three equations have five unknowns (ρ , e , σ_{zz} , U_S , and U_P), thus requiring a measurement of two parameters for closure. Typically, these were chosen for experimental reasons to be U_S and U_P , obtained by the shock transit time, and measurements of surface or interface velocities upon shock breakout. We note also that if it is assumed, as in the original work at Los Alamos,³³ that the relationship between U_S and U_P can be approximated as linear, i.e., that $U_S = C_0 + sU_P$, where C_0 is roughly equal to the zero-pressure bulk sound speed, then the pressure on the Hugoniot is

given by

$$P_H(\rho) = \rho_0 C_0^2 \kappa / (1 - s\kappa)^2, \quad (4)$$

where $\kappa = 1 - \rho_0/\rho$. While such a linear relationship between shock and particle velocity is often posited, and indeed widely used to characterize the shock response of materials, care should be taken in its employment, as it is by no means a universal law.³⁷ The locus of states that can be reached via shock compression is known as the Hugoniot. For a given compression, owing to shock heating, the pressures reached lie above both the isotherm and the isentrope, as shown schematically in Fig. 3, where this is illustrated in the case of aluminum.

The original static experiments of Bridgman studied the compressibility of matter by monitoring the motion of the compressing piston, as well as measuring electrical and thermal conductivities,¹⁵ while early measurements of shock-compressed materials relied almost exclusively on a study of the wave profiles within them, as evinced by measurements of the movement of the rear surface of a sample as the waves released from it. As such, no direct structural information was ever obtained *in situ* from either technique, which could lead to some dispute as to how the sample had actually deformed or changed phase. For example, perhaps one of the most renowned early results in shock physics was the observation by Bancroft *et al.* in 1956 of a two-wave structure in iron when shocked above 13 GPa, which they attributed to a polymorphic phase transition.³⁰ In the absence of any direct measurement of structure, Bridgman disputed the claim, noting that he could find no evidence of any change in electrical resistivity in his studies of the same element up to 17.5 GPa.³⁹ In the paper reporting those studies, Bridgman stated that “...it seems to be a widely held opinion

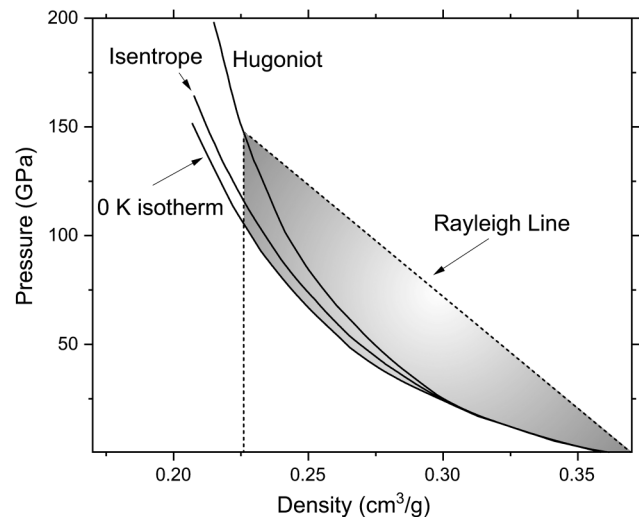


FIG. 3. The Hugoniot, isentrope, and 0 K isotherm of Al from the initial specific volume of the crystal to specific volumes near 150 GPa. The shaded area between the Rayleigh line and the 0 K isotherm shows the work that is dissipated on shock compression. After McMahan.³⁸

that transitions involving lattice type would be unlikely to occur in times as short as a few microseconds.” Fortunately for the field of dynamic compression, and indeed for the authors of this current paper, Bridgman would, in this regard at least, be proven to be incorrect, although we shall return at a later juncture to what differences may remain between static and dynamic experiments.

The next few years heralded several key developments. Improvements in electrical measurements in pressure cells by Balchan and co-workers eventually led to confirmation that there indeed was a step change in the resistivity of iron⁴⁰ at precisely the pressures seen in the dynamic work of Bancroft, and the field of shock physics was vindicated. This confirmation of a change in electrical properties of iron at 13 GPa took place around the same time as the development of the DAC in 1958,²⁰ and its subsequent adaptation to allow it to be used in conjunction with x-ray diffraction in 1960, paving the way for a true study of structure under high pressure, and building on techniques developed at lower pressures.⁴¹ X-ray diffraction could also be used in amorphous boron compression cells, and indeed these were used by Jamieson and Lawson to indicate that the transition seen by Balchan was indeed the bcc-hcp ($\alpha - \epsilon$) transition⁴²—the evidence being the appearance of a single diffraction line, the position of which was inconsistent with a bcc or fcc lattice (given the known volume), but could be reconciled as being the (1011) line of the hcp form.

The capability to study dynamically (at that time shock) compressed matter via x-ray diffraction was only developed close to a decade after its use by the static high-pressure community. Quintin Johnson at LLNL developed an x-ray diode that could produce flashes of x-rays tens of nanoseconds in duration, sufficiently bright for single-shot diffraction,⁴³ and he later obtained diffraction from explosively shocked LiF three years later,⁴⁴ proving that crystalline order was preserved behind the shock front, and subsequently used the same techniques to provide the first *in situ* x-ray diffraction evidence for a shock-induced phase transition, observing new diffraction lines when pyrolytic boron nitride, which has a structure similar to that of graphite, was shocked to 2.45 GPa, with the new lines being consistent with the wurtzite phase.⁴⁵ This was a landmark achievement in dynamic compression science, and the consensus had clearly moved on from the original views of Bridgman: as the authors of the work themselves stated “...*shock-wave Hugoniot measurements have established as a virtual certainty that shock pressures can induce crystal structure transformations within 10^{-7} s. Until now, however, it has not been possible to inspect the actual crystal structure existing under dynamic conditions.*”

The next significant developments in the field came with the realization, very soon after the invention of the laser, that they could be used to generate shock waves in materials.^{46,47} Subsequent development of the use of high-powered nanosecond optical lasers led to the capability both to shock crystals via laser ablation, but also, via a separate arm of the laser, to provide a synchronous quasi-monochromatic x-ray source. This laser-based diffraction technique was first demonstrated in the mid-80 s at pressures of just a few tens of GPa, when Wark and co-workers used a nanosecond laser to shock single crystals of silicon,^{48,49} and has subsequently been developed and adapted for diffraction from polycrystalline materials⁵⁰ far into the TPa regime.⁵¹ Indeed, the application of transient pressure via laser ablation—where a thin

surface layer of the target is vaporized and turned into a plasma by the high-intensity laser, introducing a pressure wave via Newton’s third law—is now a standard technique for dynamic compression combined with pulsed x-ray diffraction and is the basis for the majority of the science discussed within this paper. We, thus, provide a short, basic description of the underlying physical process in Sec. II A.

As noted, the x-ray source used alongside the early laser-ablation work was itself produced by a separate arm of the same laser, the energy contained within it focused on a very small spot, of a diameter of order tens to hundreds of micrometers, onto a foil mounted some mm to cm from the shocked sample. Typical laser irradiances on this foil are of order a few times 10^{14} to 10^{15} Wcm⁻². Irradiation of the foils at such intensities creates a laser-produced plasma that emits x-ray radiation isotropically. The temperatures within these plasmas are sufficiently high that for mid-Z elements there is copious emission of the resonance line radiation of helium-like ions of the element of concern, which can be used to diffract from the compressed material. While the highest pressures at which x-ray diffraction has been successfully employed to date have utilized these laser-plasma x-ray sources, these experiments suffer from several disadvantages. Most notably, the x-ray source itself is far from spectrally pure and is employed in a highly inefficient manner. The resonance lines of the helium-like ions that are used as the x-ray source are accompanied by a spectrally broad pedestal of bremsstrahlung emission. Furthermore, the x-rays are emitted isotropically, resulting in only a small fraction of them being used for diffraction after appropriate collimation (in the case of powder diffraction) or associated divergence (in the case of diffraction from single crystals). Furthermore, the natural bandwidth of the resonance line is of order 0.5%, as it actually comprises two main lines—the main resonance line itself [associated with the $1s2p$ (1P) \rightarrow $1s^2$ (1S) transition] and a strong intercombination line [associated with the $1s2p$ (3P) \rightarrow $1s^2$ (1S) transition]. Stark broadening and spectrally close transitions from doubly excited lithium-like ions (dielectronic satellites) also contribute to the linewidth, broadening it to 1.0%–1.5%.⁵² In addition, as well as thermal bremsstrahlung radiation, the optical laser intensities required to produce the mid-Z helium-like ions are sufficiently great that often copious quantities of “hot” electrons are produced, with energies significantly greater than the thermal average. The bremsstrahlung radiation from these hot electrons can produce an additional source of x rays that is hard to filter out. As a result, considerable effort needs to be made to remove background effects from any recorded diffraction pattern.⁵³

Despite the difficulties associated with laser-plasma x-ray sources, the fact that they can be produced by some of the largest and most powerful lasers on the planet, such as the National Ignition Facility (NIF)^{53,54} at Lawrence Livermore National Laboratory and the OMEGA Laser Facility at the University of Rochester,⁵⁵ has resulted in them being used to provide diffraction information on solid-state matter at extremely high pressure, well into the TPa regime, and far beyond what is achievable with DACs, with experiments at slightly lower pressures being performed on other facilities world-wide such as the LULI system in France^{56,57} and the GEKKO laser^{58,59} in Japan. As noted previously, keeping a material solid while compressing to such high pressures cannot be

achieved via shock compression, but only if the material is loaded more slowly. Much of the capability that has led to this being possible is a result of the development of exquisite temporal pulse shaping techniques of the output of these large laser systems,^{60,61} with such sculpting itself being necessary to control the amount of entropy produced when compressing laser-fusion targets,⁶² that being the primary goal of the NIF and OMEGA systems.

Such developments have led to a host of studies, in both the shock and ramp-compression regime, primarily on metals and materials of planetary interest,^{63–69} with the highest pressure at which diffraction signals have been obtained to date being 2 TPa in a study of diamond,³ showing that it does not change phase even when ramp compressed to such conditions. Furthermore, to give some degree of closure to the long-standing debate on the response of iron to shock compression, given the importance of this element in the history of dynamic compression, it is worth noting that it was experimented employing laser-plasma x-ray sources that led to the first conclusive measurement of its structure under shock conditions above 13 GPa, confirming that it does indeed transform from the bcc α to the hcp ϵ phase.^{70–72}

As noted above, laser-plasma x-ray sources have distinct disadvantages in terms of bandwidth and efficiency (being emitted isotropically), but perhaps most notable is the considerable bremsstrahlung background. In contrast, the spectrally pure, highly collimated and high-energy x-ray beams available at third generation synchrotrons have many advantages over plasma-generated x-ray sources. As a result, recent years have seen the development of a number of laser-compression experiments at synchrotrons, such as SPring-8, the APS, and the ESRF. Such experiments use a single bunch of electrons in the storage ring to generate an ~ 100 ps pulse of x rays, which is well matched to the ns-lifetimes of the compressed states. Single pulse diffraction data from laser compressed samples have been obtained at the ESRF,^{73,74} Photon Factory,^{75,76} and Photon Factory Advanced Ring.⁷⁷ At the Advanced Photon Source, a dedicated laser-compression hutch has recently been completed at the Dynamic Compression Sector (DCS) (which also includes high-explosive and gas-gun compression hutches) specifically for diffraction and imaging experiments.⁷⁸ To date, the laser-compression hutch has been used to study a number of compressed metals to pressures as high as 383 GPa.^{79–83}

Given the success of laser-plasma and synchrotron-based sources to study dynamically compressed matter, when hard x-ray FELs were starting to be planned close to two decades ago, it was evident that the study of dynamically compressed matter would be a prime area of scientific interest: indeed, the study of shock compressed materials was mentioned in some of the earliest design reports for LCLS.⁸⁴ X-ray FELs have characteristics that provide them with certain distinct advantages over synchrotron and laser-plasma sources. Typical pulse lengths are below 100 fs—this is shorter than even the fastest phonon period—providing a true snap-shot of the state of the lattice at a given instant. The output from such systems is also close to being fully spatially coherent, providing exquisite control over the size of the x-ray spot that can be used to interrogate the sample (although explicit use of the coherence has yet to be exploited). Furthermore, while the inherent bandwidth of the SASE source is close to 0.5%, recent developments in seeding technology^{85,86} have reduced this to a few times

10^{-5} without a significant reduction in the total energy in the beam which is typically of order 1 mJ. As a result, FELs have peak spectral brightnesses (photons $\text{s}^{-1} \text{mrad}^{-2} \text{mm}^{-2} \text{Hz}^{-1}$) about a billion times greater than any synchrotron.

Thus, during the planning stages of FELs such as LCLS, it was evident that siting a high-power optical laser alongside the FEL facility would provide the potential to provide novel insights into dynamically compressed matter. This realization ultimately led to the construction of the Materials in Extreme Conditions (MEC) end-station at LCLS.⁸⁷ This beamline started operations with an optical laser that could produce several 10 s of Joules of $0.53 \mu\text{m}$ light in a pulse length of order 10 ns. Each arm of this two-beam system can operate at a repetition rate of one shot every 6 min. Many of the results from the intervening period that we present in Sec. III have been obtained on this facility, although other facilities, such as one at SACLA in Japan,⁸⁸ have also yielded interesting results,^{89,90} and the High Energy Density (HED) Science end-station at the European XFEL has recently started operation,⁹¹ with the optical lasers alongside it, which will be used for dynamic compression, currently being commissioned.

At the present time, dynamic compression studies have reached an interesting juncture. The highest pressures at which solids can be diagnosed via diffraction, presently around 2 TPa,³ can at the moment only be reached with the extremely high-power nanosecond lasers such as NIF and OMEGA, which have energies per pulse in the 10 s of kJ to MJ regime, and have sophisticated pulse-shaping capabilities that allow greater control over the rate at which pressure is applied. Although these lasers can achieve such pressures, they are large, stand-alone facilities, not sited alongside FELs, and diagnosis of crystalline structure is reliant on the far-from-optimum laser-plasma sources discussed above. Furthermore, these facilities typically have very low shot rates—of order once or twice per hour for OMEGA, and perhaps a similar number of shots per day in the case of NIF: exploring the phase diagram of even a single compound at such facilities is a time-consuming and hugely expensive endeavor. In contrast, the nanosecond optical lasers that have hitherto been sited alongside FELs, for example at the MEC end-station at LCLS, have contained only a few tens of Joules in a pulse length of several nanoseconds. Given that this optical laser energy is many orders of magnitude lower than those available at NIF and OMEGA, the pressures that can be produced in the diffraction experiments are somewhat lower, although it should be noted that the spot into which the optical laser is focused at the FEL facilities is typically of order $300 \mu\text{m}$ in radius, whereas at NIF and OMEGA this dimension is often several times greater: this offsets somewhat the differences in beam energy, as it is irradiance (to the $2/3$ power—see Sec. II A) that determines pressure. The ability to use smaller focal spots at FELs is largely related to the fact that the x rays themselves can be positioned and also focused on diameters of just a few micrometers or tens of micrometers within the optical focal spot, in contrast to the situation with the divergent laser-plasma generated x rays which must be collimated in powder diffraction geometries. Furthermore, to date, the optical lasers used at FELs have not employed the impressive pulse-shaping characteristics of the larger laser systems. Clear developments in the technical capabilities of the optical lasers sited alongside the FEL

facilities will be an important driver for future scientific directions—a point to which we shall return in Sec. V.

While dynamic compression experiments at FELs have yet to attain the multi-TPa pressures in solids achieved at the other stand-alone facilities, the higher shot rate and purity of the diffracting x-ray beam have led to a series of impressive results that have improved our understanding of several areas of this important field, and which, in turn, provide further signposts to how it might develop in the future. In particular, there are promising indications that FEL-based experiments are starting to provide crucial information on the deformation pathways taken by materials under dynamic compression and, hence, an understanding of the plasticity mechanisms that determine the temperature of the compressed sample. Furthermore, several ideas have emerged that show some promise for making *in situ* temperature measurements. We also discuss these developments in Sec. IV. Before giving a short overview of the FEL experiments that have hitherto been performed, we first provide a brief description of the basic physics and current measurement techniques that underpin dynamic compression.

II. TECHNIQUES FOR ACHIEVING DYNAMIC COMPRESSION AND PRESSURE MEASUREMENTS

A. Laser ablation

Within this overview, we restrict ourselves to the dynamic application of pressure via laser ablation and we concentrate on techniques to compress matter on the timescale of several nanoseconds. Note that typical sound velocities in solids are in the km s^{-1} regime—equivalent to $\mu\text{m ns}^{-1}$. The absorption length of mid-Z elements to x rays, which will limit the useful thickness of a target for diffraction in transmission geometry, is of order a few-tens of micrometers, and thus we note how the nanosecond timescale for dynamic compression arises as a natural choice.

High-power lasers with nanosecond pulse lengths have been developed over many years, and much of the motivation for the development of lasers with the largest energies (with total energies in the 10 s of kJ to MJ regime), such as the NIF and OMEGA referred to earlier, has been the quest for the demonstration of inertial confinement fusion (ICF).^{92,93} As noted above, to date the lasers placed alongside FELs deliver smaller energies in their nanosecond pulses, typically in the regime of several tens of Joules. These solid-state lasers are usually based on Nd:Glass or Nd:YAG technology and have traditionally been flash-lamp pumped. For dynamic compression experiments, the laser light is focused in vacuum onto the target of interest, with a spot size that is typically several times the thickness of the target (to minimize the effects of rarefaction of the compression wave from the edges of the irradiated region). We are, thus, dealing with intensities such that we have several tens to hundreds of Joules in a few nanoseconds in spot sizes of order a $100\mu\text{m}$ —that is to say irradiances of interest are of order 10^{12} – 10^{14} W cm^{-2} .

The detailed physics of how such intense laser light is eventually converted to a compression wave is a highly complex process; however, simple scaling arguments can be derived from a few basic assumptions.^{94,95} At these intensities, a plasma is formed on the surface of the irradiated target, which expands into the vacuum, decreasing in density with increasing distance from the as-yet

unablated material. The light that propagates through this expanding plasma is mostly absorbed via inverse bremsstrahlung,⁹⁶ whereby the ordered oscillatory motion of the electrons in the electric field of the laser is randomized by multiple small angle collisions with the ions. However, the real part of the refractive index, μ of this plasma is dominated by the electron response such that for light of frequency ω ,

$$\mu = \sqrt{1 - \frac{\omega_p^2}{\omega^2}}, \quad (5)$$

where $\omega_p = \sqrt{n e^2 / (\epsilon_0 m_e)}$ is the plasma frequency, determined by the local electron density. Thus, light can only propagate up to a certain electron number density, n_c , which we call the critical density, given by $n_c = \epsilon_0 m_e \omega^2 / e^2$, at which point it will be reflected. Thus, the laser light deposits energy up to the critical surface, producing a hot plasma up to that point. Energy must be thermally transported down from the critical surface to the target to keep ablating material. We assume a steady-state situation ensues, by assuming that the flow velocity of the material at the critical surface is equal to the sound speed—that is Mach 1. That is to say, $v_c \approx \sqrt{P/\rho_c}$. All the pieces are now in place to construct a simple model. We equate a fraction, α , of the laser intensity I to flow down the temperature gradient to sustain the ablative flow and give rise to the outflow rate of energy at the critical surface. That is to say,

$$\alpha I \approx \rho_c v_c^3 = \rho_c \left(\frac{P}{\rho_c} \right)^{3/2}, \quad (6)$$

where

$$\rho_c \approx 2m_p n_c \approx \frac{2m_p m_e \epsilon_0 \omega^2}{e^2}, \quad (7)$$

and where v_c , ρ_c and n_c are the flow velocity, mass density, and electron density at the critical surface, respectively, and m_p and m_e are the masses of a nucleon and electron, respectively [and the factor of 2 on the left hand side in Eq. (7) is roughly approximating the number of nucleons in an ion as twice the atomic number]. From Eqs. (6) and (7), we find

$$P = \left(\frac{8\pi^2 m_p m_e \epsilon_0 c^2}{e^2} \right)^{1/3} (\alpha I / \lambda)^{2/3}. \quad (8)$$

For example, for light of wavelength $1\mu\text{m}$, an irradiance of 10^{13} W cm^{-2} , and assuming $\alpha = 0.5$, the above equation gives a pressure estimate of 200 GPa, which is surprisingly close to the experimental result, given the crudeness of the model.⁹⁷ We also see from this rather hand-waving approach the motivation for, whenever possible, efficient conversion of the laser light (which for the Nd systems has a wavelength of order $1\mu\text{m}$) to its second or third harmonic. The increase in pressure that is obtained via the $\lambda^{-2/3}$ scaling can usually more than offset the conversion efficiency losses.⁹⁸ We also note that we predict a $I^{2/3}$ scaling of the pressure

with intensity, and this lower than linear scaling will impact the design of facilities aimed at providing access to the TPa regime at FELs.

B. Pressure measurements using VISAR

In dynamic compression experiments, information about the density can be obtained directly by measurement of the lattice parameters via x-ray diffraction and, as will be discussed, x-ray spectroscopic methods are being developed to constrain temperature. For measuring the pressure conditions within the target (or more accurately, longitudinal stress), we resort to measurements of the velocity of a surface—normally the rear surface of the target. We previously commented in Sec. I B on the Hugoniot equations, noting that closure can be achieved by the measurement of two quantities, which are usually the shock and particle velocities. Via such measurements over many years, there now exists a series of equation of state (EOS) tables, such as the SESAME database,⁹⁹ linking these quantities for a particular material.

The most straightforward measurement in the situation of a steady shock is a measurement of the rear surface of the target. When the shock reaches the rear surface a rarefaction wave travels back into the target and if the isentropic release wave is approximated as a reflection of the shock wave the free surface is equal to twice the particle velocity.³¹ More accurately, the free surface velocity, U_{fs} , is given by

$$U_{fs} = U_p + \int_{V(P_H)}^{V(P_0)} \left(\frac{dP_S}{dV} \right)^{1/2} dV, \quad (9)$$

where P_H is the shock pressure and P_S is the pressure along the release path.

Such interface velocity measures are generally performed by use of the well-established Velocity Interferometer System for Any Reflector (VISAR).^{100–102} Various implementations of the technique exist: the line VISAR allows velocity profiles of a sample interface in one dimension (1D) to be measured so that drive planarity or more spatially complex samples (e.g., those with steps in their thickness) can be characterized.¹⁰¹ An implementation of the line VISAR commonly used is shown in Fig. 4. Other useful implementations of the VISAR are the 0D point VISAR^{102,103} and the 2D high-resolution VISAR.^{104,105}

The line VISAR is a high-resolution optical system that projects a two-dimensional magnified image of the target onto a streak-camera detector as shown in Fig. 4. The reflected laser-light signal passes through a pair of velocity interferometers before being recorded on the streak cameras. The interferometers superimpose a sinusoidal spatial modulation on the image: Doppler shifts in the reflected probe are manifested as shifts of these fringes at the interferometer outputs. The streak cameras record the central slit region of the field of view and sweep this signal in time across the output detector. An optical delay is achieved by a combination of the refractive delay in the etalon and an additional translational offset of the etalon–mirror combination along a direction perpendicular to the mirror plane. The translation distance, $d = h(1 - \frac{1}{n})$, is calculated to place the image of the mirror plane as viewed through the etalon coincident with its initially determined null position

(i.e., zero path delay with the etalon removed). The resulting optical time delay is $\tau = \frac{2h}{c} (1 - \frac{1}{n})$, where h is the etalon thickness, n is the index of refraction of the etalon, and c is the speed of light. The end mirror and the etalon in the delay arm of the interferometer are both mounted on a motorized translation stage.

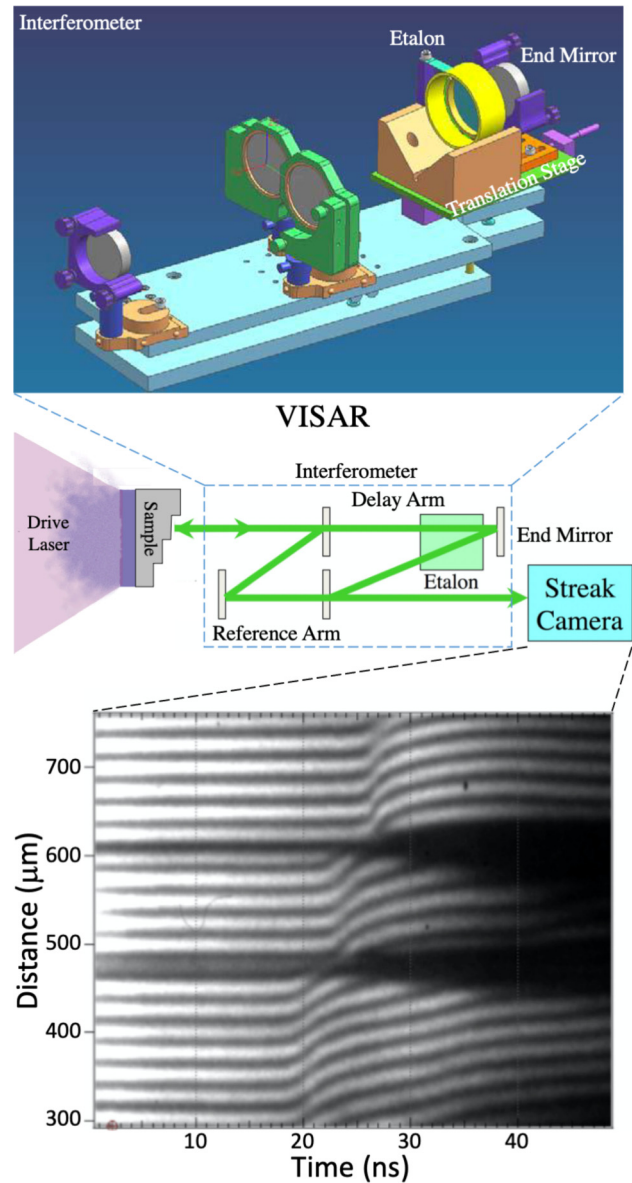


FIG. 4. The line VISAR diagnostic takes reflected laser light and runs it through a Mach–Zehnder interferometer. The spatial imaging properties of the line VISAR are essential to laser-driven compression experiments where shock planarity needs to be evaluated or where the velocity history varies with the sample position. The figure shows a typical experimental setup,¹⁰⁶ and raw streak camera data for a compression wave breaking out from a target comprising steps of three different thicknesses.

When perfectly aligned (parallel output beams), the Mach-Zehnder interferometer has a uniform output intensity; a single phase across the output. For the line-imaging application, a fringe pattern is imposed on the output by slightly tilting the output beam splitter, thus imposing a linear ramp in relative optical-path difference across the output field. Doppler shifts in the light passing through the interferometer result in changes in the optical phase at the output. These, in turn, appear as shifts in fringe position. The spatial frequency of the fringe pattern is arbitrary and is usually set to provide from 20 to 30 fringes across the output image (see Fig. 4). The apparent velocity can be related to the phase shift as

$$u_{app}(t) = \frac{\lambda}{d\tau(1+\delta)} \frac{\phi_v(t + \tau/2)}{2\pi}, \quad (10)$$

the constant, $\frac{\lambda}{d\tau(1+\delta)}$, defines the velocity per fringe (VPF) for the VISAR and $(1+\delta)$ accounts for an additional phase shift caused by dispersion in the delay etalon ($\delta = 0.0315$ at 532 nm in a fused silica etalon).^{101,102}

This apparent velocity is accurate for Doppler shifts observed from free surfaces moving in vacuum, and we have already noted that for the break out of a steady shock, the free surface velocity measurement can readily provide a stress measurement based on previous tabulated measurements. In practice, many dynamic compression experiments are more complex than this simple scenario. For example, in many cases, a transparent window is placed at the rear surface of the target such that the shock propagates into it, rather than breaking out into vacuum. Such windows may be required to sustain the pressure in the material of interest for some time, to maintain interfacial reflectivity, or to better characterize a reflecting shock. In these situations, reflections will occur at the sample-window or reflecting-shock interface and an impedance-matching analysis is required to determine the pressure-velocity relationship, as shown in Fig. 5.

Furthermore, Hayes¹⁰⁷ showed that for a complex windowed target system, Eq. (10) is equivalent to $u_{app}(t) = \frac{dZ}{dt}$, where Z is the total optical thickness between the reflecting surface and the interferometer beam splitter (the only time-dependent path lengths are within the driven portion of the target). This expression is particularly useful for understanding the index correction for two specific cases of window compression: (i) a single reflecting shock front moving at the shock velocity and (ii) an interface viewed through a dynamically compressed transparent window with a known refractive-index dependence on density, $n(\rho)$. (i) A reflecting shock is often used to determine the shock pressure as well as assess the shock stability with time, applications that have been extensively studied for quartz.^{108–110} By considering $Z(t)$ for a reflecting shock, Hayes' expression¹⁰⁷ directly leads to the correction, $u_s = \frac{u_{app}}{n_0}$, where n_0 is the refractive index of the initial (un-shocked) state. (ii) Hayes¹⁰⁷ further showed that if the refractive index of a dynamically compressed, transparent window can be written as $n(\rho) = a + b\rho$ then the true interface velocity viewed through such a window is $u_{interface} = \frac{u_{app}}{a}$, independent of the time or position dependence of the compression wave. Since the refractive index of many sample windows can fit relatively well to $n(\rho) = a + b\rho$, it is

often assumed that the apparent and actual velocities are proportional to each other.^{111–113} In these special cases, the “actual” VPF is $VPF_{act} = \frac{\lambda}{2\tau(1+\delta)n^*}$, where n^* is n_0 for a reflecting shock or a is for a transparent window with an index defined by $n(\rho) = a + b\rho$. However, for some transparent windows, the refractive index is not linearly dependent on density, and in these cases, the index correction is much more complex.^{114,115}

Thus far, we have discussed the case of a steady shock, but we have already noted that ramp compression is an area of growing interest, as it keeps the material cooler. In this situation, the velocity of the reflecting surface will rise more gradually than in the case of the shock. For such situations, and for non-steady shock compression, more complex analyses using hydrocode simulations or characteristics analysis are needed to completely determine the stress state within the sample at any given time.^{51,53}

C. Target design

Traditional HED science campaigns using large-laser drivers at facilities like NIF, OMEGA, Orion, GEKKO, LULI, or Laser Megajoule (LMJ) generally consist of 4–20 shots scheduled over several shot days. Once the shots are granted, a campaign places great significance on the success of every shot that requires ongoing modifications to the target and experimental design based on the results of previous shots. Preparing targets and the requisite shot reviews at these facilities require months of planning so that completion of a single campaign generally takes several years.¹¹⁶ By contrast, 3–5 day campaigns at a FEL consist of hundreds of shots taken every 5–10 min, and with the advent of high-repetition-rate lasers tens of thousands of shots taken at 0.1–10 Hz. Target fabrication methods have been, and are being, developed to meet these target needs.¹¹⁷

Laser-compression targets require an ablator layer designed to efficiently convert the intense laser energy into pressure and transmit this pressure to the sample; a sample layer to be compressed and probed; likely, a tamper (window) layer to equilibrate and maintain the sample pressure; and an appropriate interface for VISAR to measure the time-dependent velocity wave profile and accurately determine the sample pressure. The conversion of laser energy into pressure, discussed in Sec. II A, is most efficient for low atomic number (Z) ablators so that plastic (CH), diamond, and beryllium ablators are commonly used. Another advantage of low- Z ablators is that the x-ray emission generated by the ablation plasma is at lower energy and can often be effectively absorbed by the ablator itself or by an additional pre-heat layer. Samples are generally solid, but have included pre-compressed fluids or liquids on large laser facilities.^{118–120} Solid samples can be powdered,^{121,122} single crystal,^{48,49,70} highly textured polycrystals,¹²³ or even microscopic grains encased in an epoxy slurry.¹²⁴

Selection of appropriate ablators and tampers for specific samples and experimental goals generally requires many considerations. The ablator material must be chosen to enable the compression type (shock, shock/ramp, pure ramp) and the maximum pressure required. The ablator thickness is critical to enable sufficient transverse smoothing of the pressure drive and to eliminate unwanted reverberations that can adversely affect the pressure history in the sample. At every interface within the sample package,

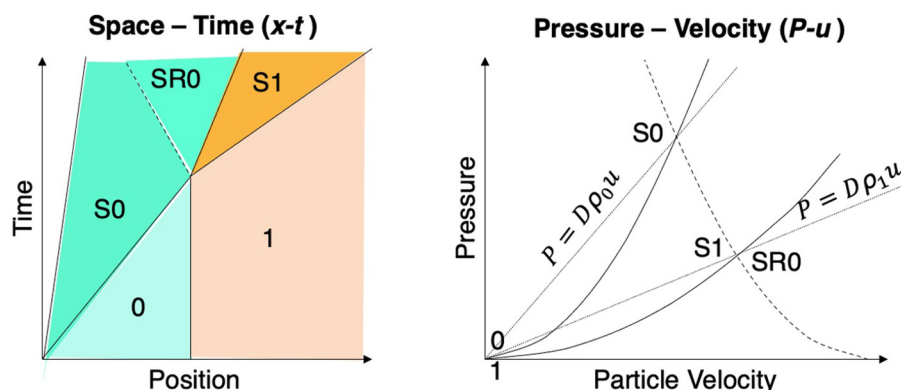


FIG. 5. Impedance matching: space-time ($x-t$) and pressure-velocity ($P-u$) plots of a sample (0) and window (1) interface. A shock takes the sample from state 0 to a shocked state S0. When the shock S0 reaches the window another shock takes the window from state 1 to S1 and a release wave (SR0) is reflected back into the sample. The corresponding states are shown in the $P-u$ plot by the forward-moving solid Hugoniot curves S0 and S1 and by the backward-moving dashed release wave SR0.

a portion of the compression wave will be reflected and a portion transmitted. Standard impedance-matching (Fig. 5) considerations can be used to simulate, calculate, or estimate the effect material choices, but invariably the choices must be checked using a hydrodynamics-code simulation that solves the equations of mass and energy transport¹²⁵ to ensure that the target package is consistent with the experimental goals of the campaign.

The need for economic and efficient production of so many targets has spurred creative fabrication techniques. Occasionally, it is economical to directly deposit a textured sample onto the ablator or to coat a CH film onto a sample film. More often the ablator, sample, and tamper layers are bonded together using a low viscosity epoxy such as Stycast 1266 (650 cP) or ÅngströmBond 9110LV (500 cP). If epoxy bonds are used, they should be carefully impedance matched to one of the bonded materials. If the epoxy layers cannot be impedance matched, they must be considered as independent layers and shock or ramp reflections at each interface will impose a stepwise “ring-up” that must be minimized to optimize control of the thermodynamic state in the sample. Even very thin epoxy layers ($\leq 2 \mu\text{m}$) are comparable to target layer thicknesses and must be explicitly considered in the target design and analyses. Through careful sample manipulation and construction, several hundred samples can be produced in under a week by talented technicians or scientists. Alternatively, elaborate robotic-controlled target fabrication procedures have been pioneered commercially,^{126–128} and bonded or shaped extended tape targets using precision rollers can produce targets that can subsequently be cut or diced.¹²⁴

In the very near future, high repetition rate lasers will be deployed at FEL facilities.¹²⁹ In order to take advantage of these new facilities, a significant change is needed in target fabrication. Tape targets 10 s of meters in length have been proposed and tested that may enable rapid target alignment and economic production, although much development remains before they are deployed routinely.^{117,124} Of particular interest for their potential for general application and economy are slurry targets where microscopic ($\leq 500 \text{ nm}$) sample grains are encased in a medium such as epoxy.¹²⁴ Significant work remains to be done to understand the energy partitioning and thermodynamic state attained in slurry targets and it is unclear whether Hugoniot states will even be possible.¹³⁰

III. WORK TO DATE ON FEMTOSECOND DIFFRACTION ON FELS

A. Plasticity and deformation

Having given some historical perspective to the field of femto-second diffraction from dynamically compressed solids, in this section we give a brief overview of some of the experiments that have been performed to date. Our overarching aim in this paper is to give our perspective on various directions and avenues of study that may be pursued in the future, and the reasons for doing so. As such, we emphasize that the work outlined here has been chosen to be representative of the status of the field and is by no means comprehensive.

The experiments that have been performed to date in this field broadly fall into two distinct categories: (i) those that interrogate plastic deformation under uniaxial shock compression and (ii) those that seek to understand the phase diagram of matter at high pressures—although as we shall discuss in further detail below, there are important overlaps between these two areas of endeavor.

In the first of the above categories, one of the initial experiments performed at LCLS that illustrated the unique capability that the platform affords was a measurement of the ultimate compressive strength of a copper crystal—that is to say, the point at which a perfect crystal would yield under uniaxial compression, with the plastic yielding occurring due to the spontaneous generation of so-called homogeneous dislocations owing to the huge shear stresses present. The challenge in demonstrating such an effect is that metallic crystals have pre-existing defects and dislocations, and when subjected to uniaxial compression these defects can alleviate the shear stress, with the associated plastic flow, an effect that is enhanced by dislocation multiplication. Given that the shear is released in this way, the ultimate strength of the material to uniaxial elastic compression cannot be tested at low strain rates. However, it had long been conjectured that if the surface of a crystal was instantaneously subjected to uniaxial stress below some theoretical limit, then on some ultrashort timescale the material would still respond purely elastically, as the strain rate would be so high that any pre-existing dislocations would be insufficient to relieve the stress, even as their number multiplied during the short compression.^{131–133} That is to say, a simple application of Orowan’s equation of plasticity,¹³⁴ $\dot{\epsilon}_p = Nv|b|$, where $\dot{\epsilon}_p$ is the plastic strain

rate, N is the number of mobile dislocations, v is their mean velocity (assumed to be subsonic), and \mathbf{b} is their Burgers vector, would indicate that the relief of shear strain would be negligible on the relevant pertinent short timescale.

There has long been evidence for the above picture in the following sense. The elastic wave [the so-called Hugoniot Elastic Limit (HEL)] that is initially seen in samples when they are shocked below the strong shock limit (defined as when the shock velocity of the plastic wave is greater than that of the elastic wave) increases in strength for thinner crystals,¹³¹ and for thicknesses in the sub-micrometer region appears to tend toward what is believed to be the ultimate strength of the sample.¹³² Indeed, a prediction was made for copper based on MD simulations by Bringa *et al.*:¹³³ within the paper describing their work using MD simulations to model shocked single crystals of copper they specifically stated “On the basis of our simulations... we predict that prompt 3D relaxation would not be observed in copper, provided that diffraction

measurements could be made at time intervals of a few picoseconds behind the shock front, which is now feasible experimentally.” Further MD simulations indicated that copper, when rapidly compressed along (111), would ultimately yield when lattice had been uniaxially compressed by of order 16%–20%.¹³⁵

A schematic diagram of the LCLS experiment¹³⁶ to test this hypothesis is shown in Fig. 6. While specific to this experiment, the setup is typical of that used in the majority of dynamic compression experiments performed to date on FELs. As can be seen from the diagram, the experiment is in the Debye–Scherrer geometry. Thin ($1\ \mu\text{m}$) layers of copper were deposited on Si wafers (in contrast to many experiments, the target did not have a sacrificial ablator on its surface, as is normally the case for target design, as outlined in Sec. II C). A compression wave, with peak pressure close to 1 Mbar, was launched in them by a laser pulse that had a roughly Gaussian temporal shape with an FWHM of 170 ps. The laser was focused on a spot slightly greater than $250\ \mu\text{m}$ in

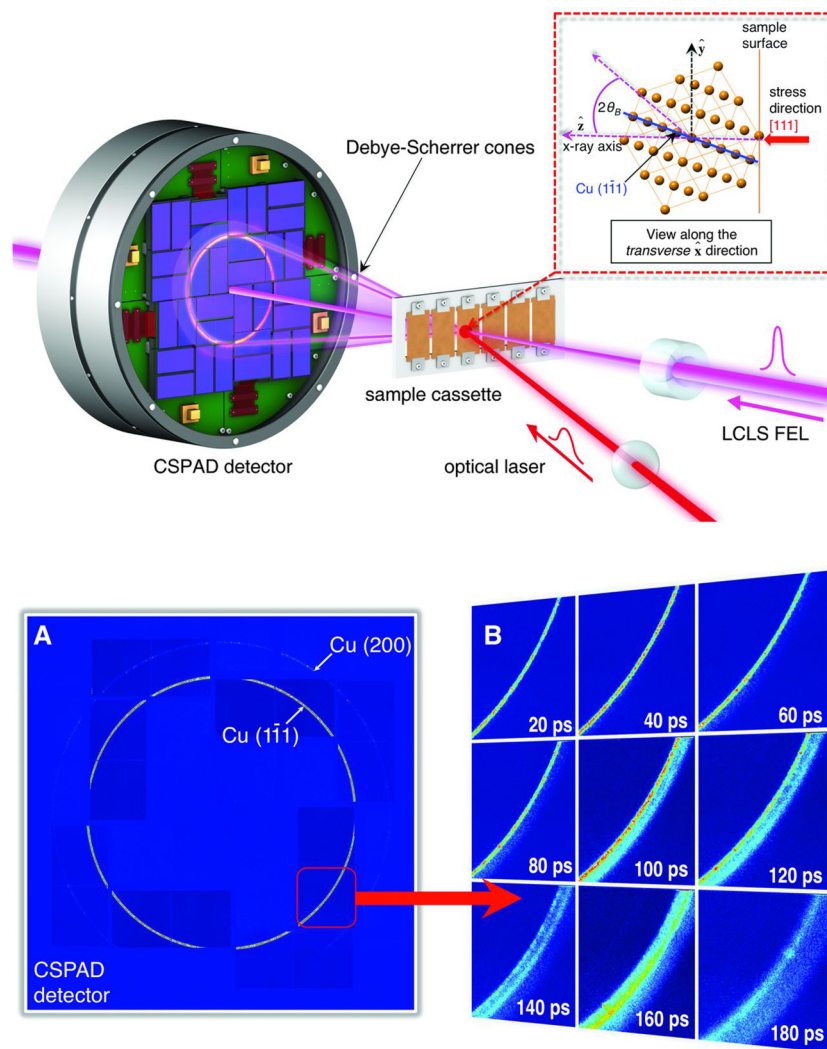


FIG. 6. (Upper image) A schematic diagram of the experimental setup to measure the ultimate compressive strength of copper, with (lower image) raw diffraction data as a function of delay time between the x-ray pulse and the optical laser pulse. Reprinted with permission from D. Milathianaki *et al.*, *Science* **342**, 220–223 (2013). Copyright 2013 AAAS.

diameter. X-ray pulses from the FEL of energy 8 keV and pulse length under 50 fs were focused by beryllium lenses to a spot of order $30\text{ }\mu\text{m}$ diameter, co-centric with the optical laser pulse. These x rays were, thus, diffracted from the shocked region and could be timed with respect to the shock pulse to better than a picosecond. The diffracted x rays were detected using an in-vacuum, 2.3-megapixel array detector [the Cornell Stanford Pixel Array Detector (CSPAD)¹³⁷] (for a detailed description of these detectors, see elsewhere¹³⁸).

A series of successive shots were then taken with the delays between the optical and x-ray pulses changed at each step by 20 ps, and a fresh target was translated into the beams for each laser shot. Importantly, the grains within the copper layers were not randomly oriented. As they had been grown by deposition, the copper targets were fiber textured—that is to say normal to the target they had sub- μm grains that were preferentially oriented $\pm 3^\circ$ along the [111] direction, but random azimuthally about it. Diffraction then took place from the $[1\bar{1}1]$ planes.

The raw diffraction data are shown alongside the experimental setup in Fig. 6. The unshocked material scatters x rays close to

39.5° and diminishes in intensity as the wave traverses the sample. As the surface of the target starts to become compressed, diffraction at higher angles occurs, and in Fig. 6(b) a second diffraction ring of larger radius can clearly be seen to emerge. At early time, this new peak occurs at around 40.25° , which corresponds to 1D elastic compression of about 17%, as predicted. Note that, given the compression wave is moving slightly faster than the speed of sound, it takes of order 180 ps for the compression wave to traverse the $1\text{ }\mu\text{m}$ thick sample, and thus early on the x rays are diffracting from both the compressed region of the target at the surface and the yet-to-be compressed region below it. On a timescale of about 60 ps, again in good agreement with original predictions, diffraction at higher angles occurs, consistent with the lattice relaxing in all three dimensions, but with a lower strain in each. Lineouts of the data are shown alongside the simulated diffraction signals¹³⁹ in Fig. 7. Excellent agreement between the experimental data and the simulations can be seen. The simulations use quite a simple model where the plasticity essentially follows Orowan's equation, and the number of dislocations in the system rise copiously once the ultimate strength of the material is exceeded. Thus, one of the first

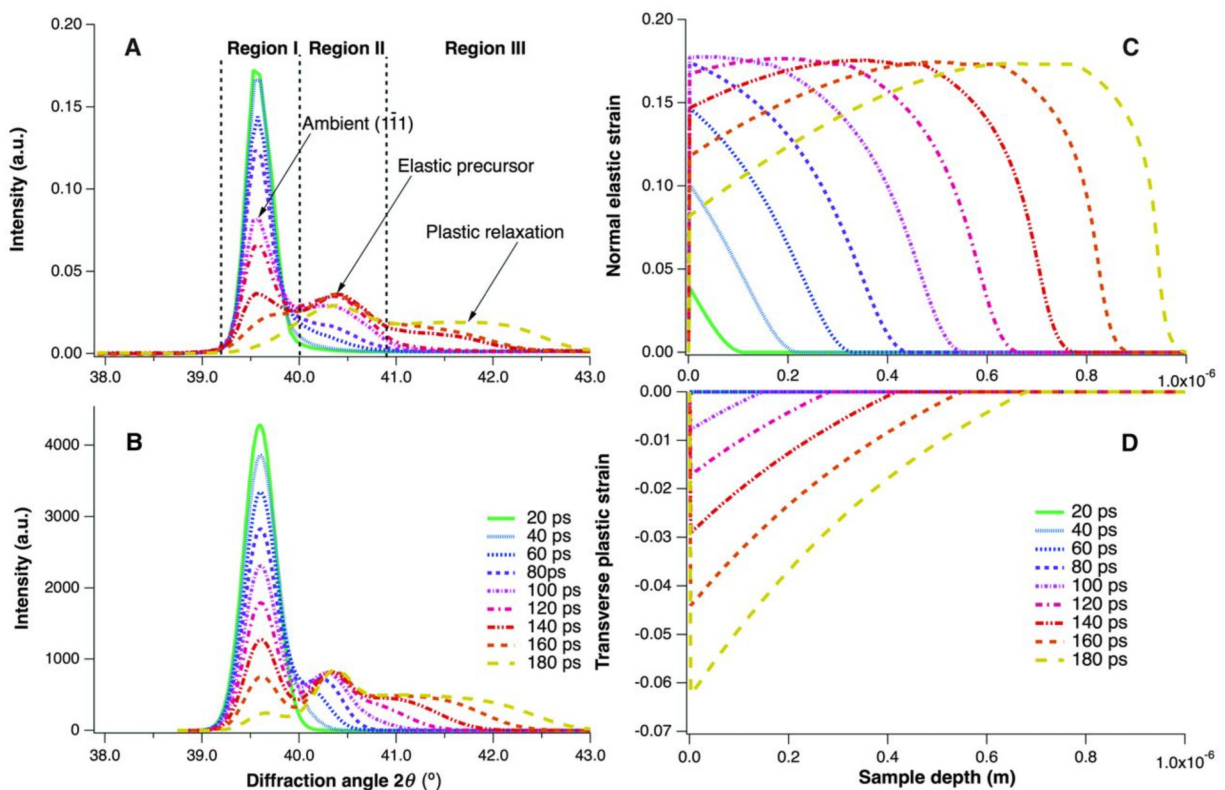


FIG. 7. Experimental diffraction data from the experiment depicted in Fig. 6 resulting from the azimuthal integration around the Debye–Scherrer ring. The diffraction profiles are divided into three regions to illustrate the characteristic lattice response: region I, the unstrained lattice; region II, the elastically compressed lattice; and region III, the lattice exhibiting three-dimensional relaxation. (B) Simulated diffraction data resulting from the calculated strain profiles, showing good agreement with the experiment. (C) The modeled time-dependent normal elastic strain and (D) transverse plastic strain profiles vs sample depth using the code described in the work of Wark *et al.*¹³⁹ Reprinted with permission from D. Milathianaki *et al.*, Science **342**, 220–223 (2013). Copyright 2013 AAAS.

dynamic compression experiments performed at LCLS successfully measured the ultimate compressive strength of a single crystal and confirmed MD predictions made several years prior to its execution.

As noted above, in the experiment of Milathianaki, the targets were fiber-textured, and the experiment was performed in a Debye-Scherrer transmission geometry. A further feature of this experiment was that the surface normals of the targets were aligned anti-parallel to the incoming x-ray beam. A further seminal experiment in this first category of plasticity studies investigated lattice rotation and twinning under shock compression in tantalum crystals. In many aspects, the experimental setup was very similar to that shown in Fig. 6, but with several important differences. In this experiment,¹²³ tantalum targets were used. Their thickness ($\sim 6\mu\text{m}$) was greater than that in the copper experiment. Furthermore, these targets had a $50\mu\text{m}$ thick kapton ablator glued to their surface. They were irradiated with an optical laser pulse which had a 5–10 ns pulse length and focused on spots varying from 100 to $250\mu\text{m}$ diameter and enabled dynamic pressures within the Ta target ranging from 10 to 300 GPa to be created. One effect of the ablator was to ensure that the compression wave that was launched into the Ta had formed into a steeply rising shock. Finally, unlike in Fig. 6, the normal to the target surface was not anti-parallel to the direction of propagation of the FEL x-ray beam: the target was tilted so that its surface normal made an angle to the x-ray beam axis. Given that the targets were again fiber-textured [in this case with grains having the normals to their (110) faces along the surface normal] symmetry is broken, and because of this symmetry breaking complete Debye-Scherrer rings are not observed, but arcs of diffraction are seen, the azimuthal position of

which encodes the angle that the lattice planes make to the surface normal. Thus, by monitoring the position of the arcs, both compressive elastic strains and the angles that distinct lattice planes make to the surface normal can be interrogated.¹⁴⁰

The key results from this experiment can be seen in Figs. 8 and 9. The first of these, Fig. 8, shows the observed diffraction patterns for four shots at four different pressures (as determined by the VISAR measurements). Diffraction from certain members of two families of planes, {110} and {200}, can be seen at certain azimuthal angles. Also shown are the angles, χ , that the specific planes make with respect to the target normal—in this case, we can observe two members of the {110} family of planes, one that is perpendicular to the surface normal and another that makes an angle of 60° with respect to it. As diffraction is taking place when the shock has only traversed part of the crystal, diffraction takes place from both the shocked region and the unshocked regions of the target, and this can be seen by noting the shift in diffraction angle, and the expansion of the Debye-Scherrer ring, which increases with shock pressure, gives a measure of the change in the lattice spacing. However, what can also be observed, and is most noticeable at the highest pressure of 169 GPa, is that the diffraction coming from the plane that makes an angle of 60° to the surface normal splits into two, indicating that these planes have rotated significantly.

Analysis of the diffraction patterns over a wide range of pressures showed that the lattice planes rotated under compression, rotating by up to 14° at shock pressures of 250 GPa. Deformation of the sample due to twinning could also be directly observed, as the twins could be identified owing to their differing position azimuthally in the diffraction pattern, and the fraction of the sample

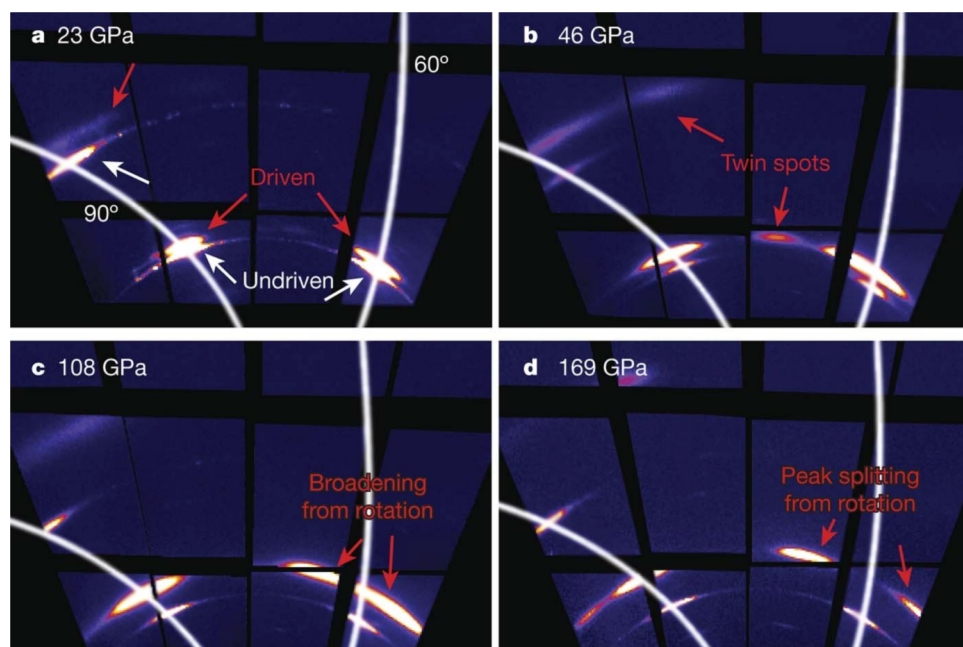


FIG. 8. Diffraction patterns from tantalum shocked to the pressures shown. The spots corresponding to the driven portion of the sample (highlighted by red arrows) appear at higher diffraction angles than those corresponding to the undriven portion (highlighted by white arrows), appearing as a shift upwards in this view. Lines of constant χ (angle between the lattice plane and sample normal) are shown at 60° and 90° to illustrate the reorientation of the texture spots in driven tantalum. (a) At 23 GPa, no reorientation is observed, because the diffraction spots for the driven and undriven samples have the same azimuthal location. (b) At 46 GPa, new texture spots arise that correspond to twinning across a 112 mirror plane and an additional 2.5° rotation. (c) and (d) At higher pressures [108 GPa (c); 169 GPa (d)], large lattice rotations are observed, causing the $\chi = 60^\circ$ (110) spot (highlighted by red arrows) to broaden and then split. Figure reproduced with permission from the work of C. Wehrenberg *et al.*, *Nature* **550**, 496–499 (2017). Copyright 2017 Springer Nature.

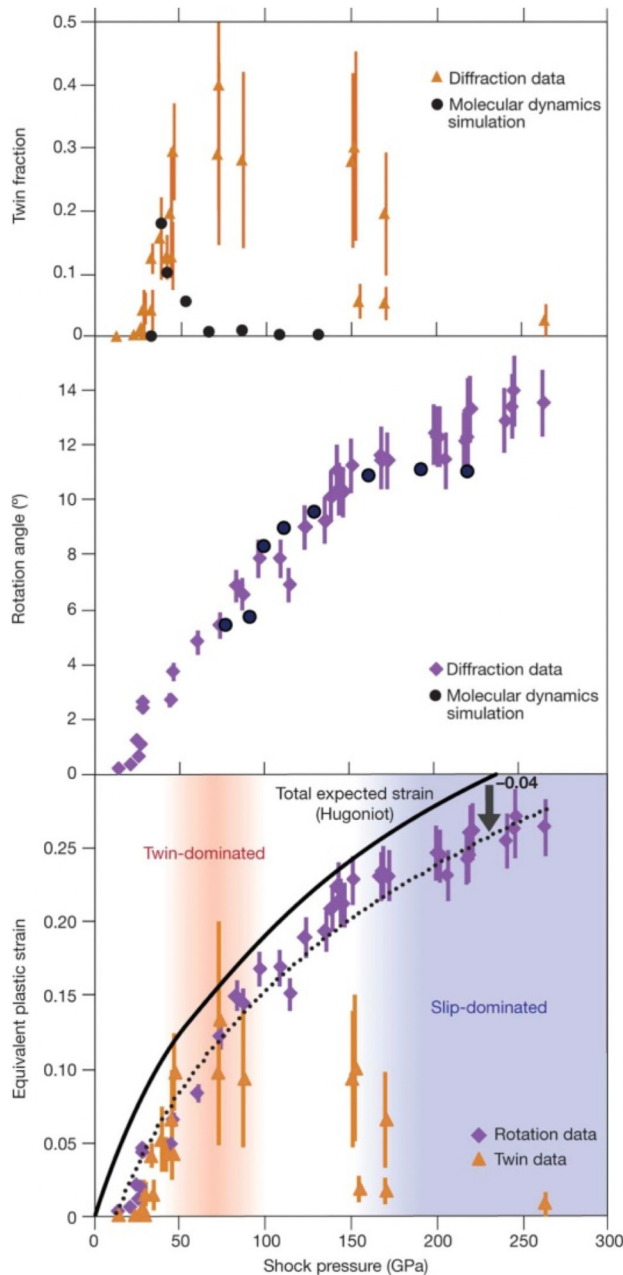


FIG. 9. Twin fraction, rotation angle, and plastic strain computed from the diffraction data such as that shown in Fig. 8. Upper plot: twin fraction as a function of shock pressure, measured from diffraction data by the ratio of texture spots (orange triangles) and from molecular dynamics simulations (black circles). Middle plot: lattice rotation angle from x-ray diffraction data (purple diamonds) and from molecular dynamics simulations (black circles). Lower plot: equivalent plastic strain inferred from lattice rotation (purple diamonds) and twin fraction (orange triangles). The equivalent plastic strain for a material subject to hydrodynamic shock ("on the Hugoniot") is also plotted (black curve). Figure reproduced with permission from the work of C. Wehrenberg *et al.*, *Nature* **550**, 496–499 (2017). Copyright 2017 Springer Nature.

that had twinned could be deduced from the associated diffraction intensity. The experiments found a peak in the twin fraction at pressures of order 75 GPa, as shown in Fig. 9, where the rotation angle as a function of shock pressure is also shown. Reasonable agreement with MD simulations was found for the observed rotation angles, though the experiments were undertaken with fiber-textured polycrystalline material, and the MD simulations were of single crystals oriented along (110).

In the original paper describing this work, the rotation angle was used to predict the total amount of plastic strain using a model that assumed two things: first, that the plasticity at each point in the crystal was due to the activation of a single slip plane, and second, that the rotation angle and plasticity were related in a way originally determined by Schmid.^{141,142} If we denote by ϕ_0 and ϕ the angles made by the slip plane normal with the compression direction before and after compression, then the rotation angle $\omega_{\text{Schmid}} = \phi_0 - \phi$ is given by

$$\omega_{\text{Schmid}} = \phi_0 - \arccos\left(\frac{\cos \phi_0}{\ell/\ell_0}\right), \quad (11)$$

where the quantity ℓ/ℓ_0 coincides with the total engineering strain along the loading direction.

Under these assumptions, the plastic strain inferred from the rotation angles could be compared with that predicted to be present on the Ta Hugoniot (assuming a complete loss of strength). It can be seen from the lower plot of Fig. 9 that within this framework the rotation measurement underestimates the plastic strain by about 4% (dotted curve) and that twinning accounts for the majority of the Hugoniot plastic strain in the 40–80 GPa range (pink shaded region); however, twinning-induced strain falls well below the total plastic strain above 150 GPa (blue shaded region), indicating that the response is slip-dominated in this regime.

The causes for the discrepancy between the plasticity inferred from rotation, and that expected on the Hugoniot, could be thought to be due to either more than one slip system being activated or some other discrepancy in the model (especially as the MD data seem to predict the rotations reasonably well). Indeed, both of these issues are pertinent, and we will return to them in Sec. IV B, where we discuss how measurements such as this are influencing the direction in which plasticity studies on FELs are taking, and our perspectives on future directions being taken in the field.

This same experiment also showed that the lattice rotations and twinning imparted by the shock were largely reversed when the shock broke out from the rear free surface of the target.¹⁴³ This is a particularly important result for the field of shock physics as a whole: it had long been known that very high dislocation densities must be present at and behind the shock front in order to explain the plastic strain rates observed (again as dictated by Orowan's equation), but such very high defect densities are not seen in recovered samples. While previous MD simulations had indicated that dislocation annihilation could occur upon shock release and rarefaction, the LCLS data, demonstrating de-twinning and the rotation of the lattice back toward its original position, provide some of the first experimental insight into such an effect happening in real

time. While the fact that the lattice rotated largely back to its original position is not itself full proof of defect annihilation, it is consistent with such a microstructural effect, and in the MD simulations the lattice reorientation and defect density reduction were seen together.

As well as observation, upon release, of a reversal in the lattice rotation, these experiments also showed that while the rarefaction wave traveling back into the sample did so at an ever-decreasing strain rate (producing a classic rarefaction fan), close to the surface the plastic strain rates were still so high that significant plastic work was being performed.¹⁴⁴ This plastic work led to heating upon release of the surface of sample, counteracting the cooling brought about by the thermo-elastic effect. It is only the latter of this that is normally taken into account in a textbook description of shock release from a free surface, where the release process is assumed to be isentropic. These experiments showed that this is an oversimplification of the processes that are taking place within the first few micrometers of the surface, and on the nanosecond timescale—i.e., precisely the time and length scales of typical laser shock experiments.

The work on tantalum discussed above also illustrates how FEL-based experiments can enable the exploration of relatively high-pressure states with what might be deemed modest optical laser energies, to which we alluded in Sec. I B. In these uniaxial compression experiments, the rarefaction from the edges of the optical focal spot generally means that compression cannot be sustained in the central region of the target over shock propagation distances greater than those comparable to the diameter of spot, although this will be very target specific. However, as the FEL x rays can be focused on a very small spot (down to 20 μm in these experiments), and non-planarity of the center of the compressed region monitored with the VISAR diagnostic, significantly smaller optical spots can be employed in these experimental setups than those using laser-plasma based x rays. As it is the laser intensity that determines pressure, lower optical energies can be employed. Indeed, in the work of Wehrenberg *et al.*, optical spot diameters of 100 μm were used, and high quality data hence obtained up to pressures of 250 GPa with optical laser energies of just 30 J in a 10 ns pulse.¹²³

In conclusion of this section, we note that the experiments discussed above have investigated classic face-centered and body-centered cubic metals, and even in these cases we are only just starting to discover how materials act at the lattice level to such rapid compressions. Other types of materials are clearly also of interest, and particular attention is being paid to the response of diamond above its elastic limit,¹⁴⁵ given that it is often used as a confining material in ramp-compression experiments.

B. Shock-induced phase transitions

In Subsection III A, we have described some of the experiments that have taken place to date using femtosecond diffraction to directly study plasticity and deformation. The second area that has received significant attention is that of the observation of shock-induced phase transitions. Within Sec. I B, we described how in many ways the whole field of the determination of the structure of crystalline matter was vindicated by the α - ϵ transition in iron

being deduced by shock wave measurements that were later confirmed by static measurements, with good agreement regarding the transition pressure being found. However, it is clear that there is by no means always such a simple relationship between what is seen (or predicted to be seen) under long-term static conditions, and what is seen dynamically—again in Sec. I B we described how diamond is predicted to transform to a BC8 structure above 1 TPa, but appears to remain in the cubic diamond phase in the dynamic experiments performed to 2 TPa.³ As we will indicate in Sec. IV D, understanding such discrepancies between static and dynamic measurements will be necessary in the context of relating the two—i.e., making inferences about the long-term behavior of materials within planets, and how they behave on nanosecond timescales when generated by laser compression.

One material that has received considerable attention over many years is elemental silicon. Indeed, as this material can be made in an almost defect-free single-crystal form, one might initially envisage that its response to rapid compression would be relatively straightforward to predict. In practice, the converse has been true. Studies of shock-compressed single crystals of silicon date back over many decades, to the seminal work of Gust and Royce,¹⁴⁶ where the multiple waves observed in samples shocked along various crystallographic directions were interpreted in terms of a plastic response, followed by a phase transition, with the Hugoniot Elastic Limit (HEL) being observed to vary from 5.9 GPa (along $\langle 110 \rangle$) to 5.4 GPa ($\langle 111 \rangle$) and 9.2 GPa ($\langle 100 \rangle$). As noted in Sec. I B, silicon was also the first material to be studied on nanosecond timescales using a laser-plasma x-ray source.^{48,49} Such nanosecond laser-based experiments found the response remained elastic to much higher pressures than those seen in the μs explosively driven experiments of Gust and Royce and also observed two elastic waves in silicon shocked along $\langle 100 \rangle$, which were at the time difficult to explain,¹⁴⁷ and were followed by a significant number of studies of the material on different platforms.^{148–150} On the basis of MD simulations, it was suggested that the first wave, identified as an elastic-plastic transition by Gust and Royce, was in fact the onset of a phase transition to the tetragonal β -Sn or the orthorhombic *Imma* phase.¹⁵¹ The response of the crystal is termed inelastic, rather than plastic, in the sense that conventional plasticity under uniaxial strain leads to a situation where there are more unit cells of the material per unit length transverse to the shock direction. However, Moggi *et al.* posited that the relief of the shear stress due to the phase transition did not alter the number of (primitive) unit cells in this transverse direction—the new phase has a larger lattice vector perpendicular to the shock than that of the ambient lattice, and thus its generation within the material leads to a reduction in the lattice spacing perpendicular to the shock of the unconverted silicon, thus letting it relax toward the hydrostat (given the lattice spacing along the shock direction is already reduced).

This picture was largely confirmed in a series of laser-plasma based x-ray diffraction experiments that agreed qualitatively with the MD simulations.¹⁵² Furthermore, these experiments finally provided an explanation for the two elastic waves seen in the nanosecond laser experiments, but apparently absent in dynamic experiments on longer timescales: the double elastic wave structure was found to be consistent with a phase transformation taking

place over a few nanoseconds and with the transformation leading to a volume collapse. Before the transformation takes place, the elastic response is large (if the applied stress is large), but the delayed volume collapse upon transformation, which starts at the irradiated surface of the crystal, leads to a rarefaction wave traveling forward into the elastically compressed material, lowering the elastic compression, and eventually outrunning the shock front of the large elastic response, and thus leading to a single elastic wave at lower stresses. It is for this reason that the very large elastic response was not seen in longer timescale experiments.

The utility and versatility of x-ray FELs in providing novel information is evident in the way that such experiments have been able to confirm much of the picture painted above. Given the few nanosecond timescale of the phase transformation, corresponding to length scales of tens of micrometers, in laser-based experiments both the elastic waves, and the subsequent regions of the crystal undergoing phase transitions due to the rapid compression, co-exist. It has been argued that this co-existence complicates the diffraction pattern, as the diagnostic x-ray beam is diffracted from a range of different phases, all of which have strain gradients along the shock direction associated with them. To overcome this problem, McBride *et al.* developed a geometry, shown in Fig. 10, where the focused x-ray beam is incident on the target perpendicular to the shock propagation direction,¹⁵³ which ensures that in the majority of cases a single wave within the multi-wave profile is probed, aiding greatly in the data interpretation.

While referring the interested reader to the original paper for more details, the conclusion of this study was that the wave following the elastic wave was indeed due to a phase transition. Importantly, the onset of the transition to β -tin was seen at a longitudinal stress as low as 5.4 GPa, consistent with the HELs seen in the original Gust and Royce work. Of further note is that this figure should be compared with the pressure of 11.7 GPa at which the same transition is seen in static DAC experiments.¹⁵⁴ The fact that both strain rate and high shear stresses could have a large influence on the transition pressure had been noted previously in nano-indentation experiments at loading rates of order 0.1 GPa s^{-1} , where some evidence for the transition occurring around 8 GPa was found for silicon loaded along [111].¹⁵⁵

Additional evidence for the mechanism underlying the transition has recently been put forward by experiments at LCLS utilizing single crystals.¹⁵⁶ This work supports the picture put forward by Mogni, but is at odds with models for the transformation mechanisms put forward by Turneaure *et al.* in shock experiments, but on longer timescales than the nanosecond laser-ablation experiments.¹⁵⁷ It is believed that this indicates that even once the transformation has taken place, relieving some of the shear stress, further relaxation can alter the orientational relationships between the initial and final phases.

In any event, the series of experiments cited above leads to an important conclusion: owing to the high shear stresses that are present in dynamic compression experiments, or the timescale of the kinetics of the transition, or indeed both, we cannot automatically assume that the phase diagram of matter that we might deduce from dynamic compression experiments is the same as that which pertains under static conditions, and this fact must be borne in mind when making claims that attempt to relate dynamic

experiments to fields where the relevant timescales are considerably different—e.g., the state of matter within the interior of planets. Furthermore, given that nucleation rates and the surmounting of transition barriers (and hence kinetics) are likely to be highly temperature dependent, it is evident that accurate measurements of the temperature of the sample will also be important, a theme to which we shall return in Sec. IV C.

The above statements have also been shown to be pertinent in another class of materials. We recall the words of Bridgman quoted in Sec. I B where he questioned whether lattice rearrangement could indeed take place under the short timescales of shock compression. Even though such modifications can indeed be made, it is still of interest to question whether quite complex new phases can form on nanosecond timescales. It is in this context that we note that a major and unexpected discovery in static high-pressure science at the turn of the millennium was the discovery of both modulated and composite incommensurate phases in elements such as barium,¹⁵⁸ bismuth,¹⁵⁹ iodine,¹⁶⁰ and tellurium.¹⁶¹ Similar phases were subsequently found in other Group 1,^{162–164} 2,¹⁵⁹ 15,¹⁶⁵ 16,^{161,166,167} and 17 elements,^{168,169} as well as in Sc¹⁷⁰ and Eu.¹⁷¹

The most exotic of these structures is the composite host–guest structures that comprise a tetragonal or monoclinic “host” structure with 1D channels running along the *c*-axis. Within these channels are chains of “guest” atoms, which crystallize in structures with a *c*-axis incommensurate with that of the host structure. The diffraction patterns from such structures comprise diffraction peaks that come from the host structure alone, from the guest structure alone, or from both. Such structure can be described within the formalism of 4D superspace where diffraction peaks are indexed using four Miller indices (*hk₁l₁m*) rather than the traditional three indices.¹⁷² Reflections from the host component of the basic composite structure have indices (*hkl*0), those from the guest have indices (*hk₀m*), and the (*hk*00) reflections are common to both host and guest. In both Rb and K, a “chain melted” phase of the host–guest structures was observed in DAC experiments where the (*hk₀m*) peaks from the guest structure disappeared on either pressure decrease¹⁷³ or temperature increase.¹⁷⁴ In such a structure, the atoms within the guest chains have no long-range order and might, therefore, be regarded as 1D chains of liquid within the crystalline host structure.

When FEL diffraction experiments began at the LCLS, an obvious question to address was whether such complex structures would form on the nanosecond timescales of dynamic compression experiments. As the incommensurate phase in Bi, Bi-III, is stable at pressures as low as $\sim 3 \text{ GPa}$ in DAC experiments,¹⁵⁹ and is easily accessible along the Hugoniot, such experiments were expected to be straightforward. However, Bi is well known to have phase boundaries that are different in static and dynamic experiments and that are strain dependent.¹⁷⁵

A detailed series of experiments at LCLS revealed that while the Bi-I \rightarrow Bi-II transition is observed under shock compression in Bi [Fig. 11a(ii)], the incommensurate Bi-III phase is *not* seen on further compression¹²¹ (Fig. 11), although the equivalent incommensurate phase is seen to form in Sb¹⁷⁶ on nanosecond timescales. The non-existence of incommensurate Bi-III on shock compression was confirmed in a subsequent shock experiment at the ESRF synchrotron.¹⁷⁷ While the guest chains in Sb were found to form the same crystalline structure within the host as was

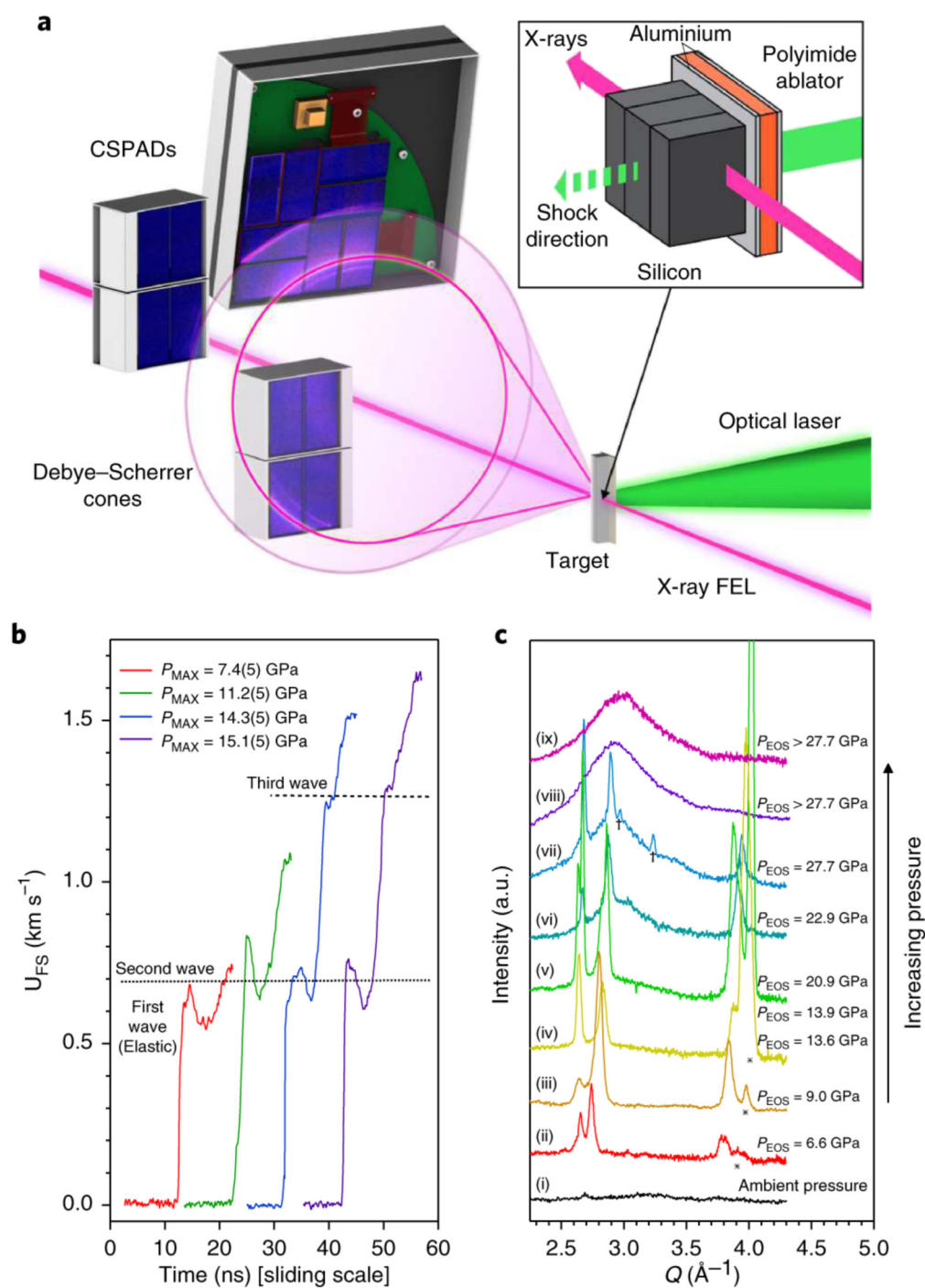


FIG. 10. (a) The transverse probe setup used by McBride *et al.* whereby the compression laser was perpendicular to the x-ray beam. (b) VISAR lineouts showing the free surface velocity (UFS). Dashed lines indicate the onset of the second and third wave. P_{MAX} denotes the maximum pressure reached as inferred from VISAR. (c) Azimuthally integrated one-dimensional diffraction patterns as a function of increasing laser intensity, and hence increasing pressure, as determined from the equation of state (PEOS) in both the transverse (i), (ii), (iv), (v), (ix) and collinear (iii), (vi), (vii), (viii) configurations. Peaks marked with the * symbol belong to the compressed cubic diamond phase. Peaks marked with the † symbol cannot be described by the cubic diamond, β -tin, *Imma*, or simple hexagonal phases. Figure reproduced with permission from the work of E. McBride *et al.*, Nat. Phys. **15**, 89–94 (2019). Copyright 2019 Springer Nature.

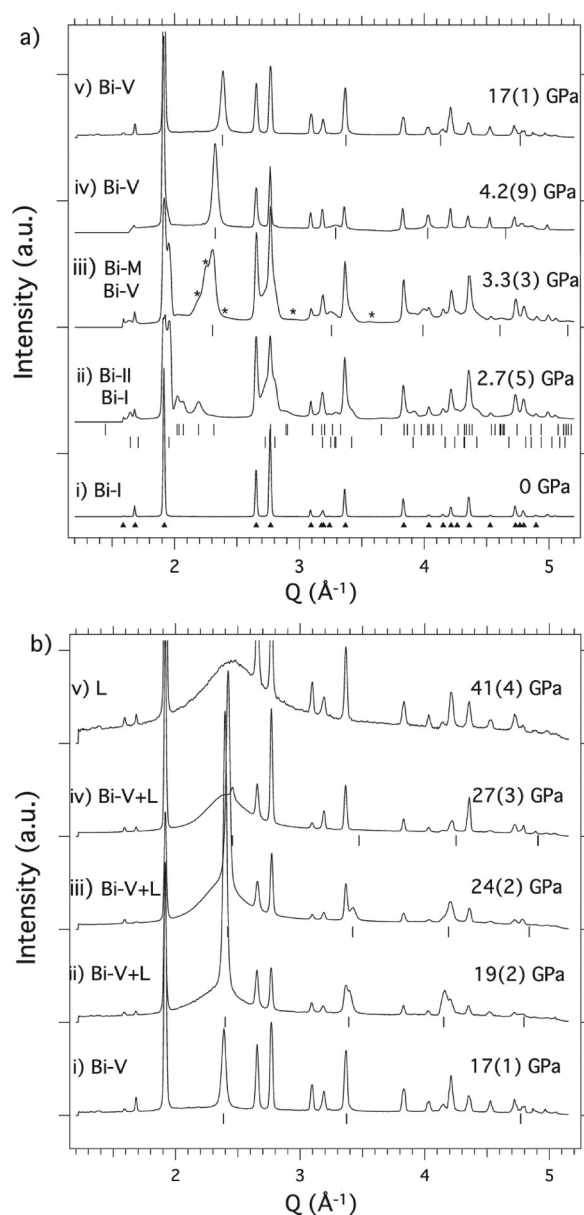


FIG. 11. Diffraction profiles from the different solid and liquid (L) phases of Bi seen on shock compression, as obtained on the MEC beamline at the LCLS.¹²¹ Bi-I [profile a(i)] first transforms to Bi-II [profile (ii)] at 2.5 GPa (upper tick marks). Rather than then transforming to incommensurate Bi-III, a transition to a metastable phase (Bi-M, and whose peaks are marked with asterisks), not seen in static compression studies, is then observed at 3 GPa [profile a(iii)]. Bi-M is always accompanied by diffraction peaks from the higher pressure bcc Bi-V phase, the locations of which are indicated by tick marks. Above 4 GPa, only peaks from Bi-V are observed [profiles a(iv,v)]. In static compression studies, Bi-V is seen only above 7 GPa. Scattering from liquid-Bi first appears at 19 GPa [profile b(ii)] and the liquid phase-fraction increased with pressure [profiles b(iii, iv)] until only diffraction from the liquid phase is observed above 27 GPa [profile b(v)]. From M. G. Gorman *et al.*, *Sci. Rep.* **8**, 16927 (2018). Copyright 2018 Author(s), licensed under a Creative Commons Attribution (CC BY) license.

previously seen in static compression experiments, this was *not* the case in dynamically compressed Sc, where the chains of guest atoms were found to have no long-range order, as determined by the absence of the $(hk0m)$ “guest-only” diffraction peaks¹⁷⁸—as illustrated in Fig. 12.

While the host-guest Bi-III phase was not observed in Bi, a new high-pressure metastable phase, Bi-M, the structure of which remains unknown, was observed [see Fig. 11a(iii)].^{121,177} Also, the higher-pressure Bi-V phase was seen at pressures above only 3.3 GPa on compression [Fig. 11a(iii)], while it is not seen below 7 GPa in static compression studies,¹⁵⁹ and as low as ~ 1.6 GPa on release.¹⁷⁷ On further compression, Bi-V was observed to melt at 19(2) GPa [see Fig. 11b(ii)], and the diffraction data from shock-melted Bi were also of sufficient quality [see Fig. 11b(v)] to follow the structural changes in liquid-Bi for the first time.¹²¹

These experiments perfectly demonstrated the quality of the diffraction data that is available from dynamic compression experiments at FELs such that multi-phase profile refinement of incommensurate structures and the extraction of coordination changes in liquids are possible. More recent experiments have extended such studies to 80 GPa and 4000 K in Sn.¹⁷⁹

The key result from the Bi studies at LCLS, thus, reveals that on nanosecond timescales not only are the boundaries between different phases potentially found at different regions of the phase diagram, but it is possible that phases seen statically are completely absent in the dynamic case and vice versa. This stresses the importance of knowing the crystal structure along the compression path and determining exactly where it changes. It also raises the

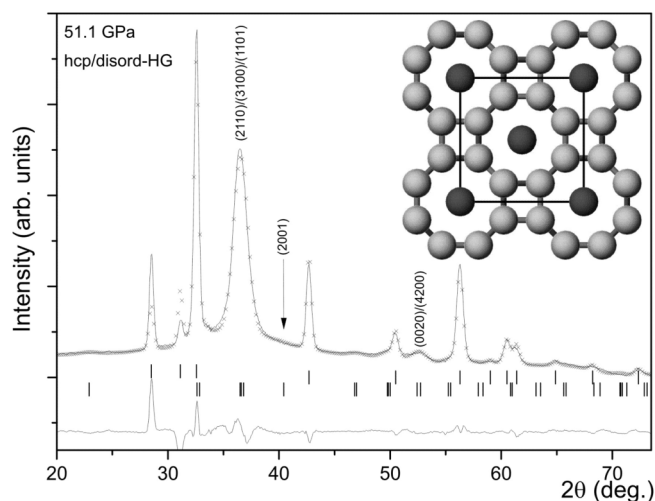


FIG. 12. A two-phase hcp:host-guest Rietveld fit to a diffraction profile obtained from shocked Sc at 51.1 GPa, with the most intense peaks indexed. The best fit to the profile is obtained when the 1D chains running along the c -axis of the incommensurate host-guest structure (shown as darker atoms in the structural figure in the inset) are disordered and liquid-like. If the chains were ordered, then the (2001) reflection at $\sim 40^\circ$, marked with an arrow, would be clearly visible. Figure reproduced with permission from R. Briggs *et al.*, *Phys. Rev. Lett.* **118**, 025501 (2017). Copyright 2017 APS.

possibility that the phases seen under extreme P-T conditions in short-lived laser compression experiments are not necessarily the equilibrium phases existing under the same P-T conditions within planets: a fact that reinforces the weight of our view that a degree of circumspection is advised when attempting to directly relate dynamic experiments to static contexts. We are only starting to make progress in this area, where the results from static compression, dynamic DAC,¹⁸⁰ impactor, and laser compression experiments will be required in order to probe sample behavior over strain rates spanning nine orders of magnitude.

IV. PERSPECTIVES ON FUTURE DEVELOPMENTS

In Secs. I–III, we have outlined some of the relevant history of the field of dynamic compression combined with x-ray diffraction techniques and given some examples of the sorts of experiments that have taken place at FEL facilities in recent years. We now turn our attention to providing our perspective on what we believe to be important lines of development in the near to medium term. It will be evident that from the comments we have made thus far that we consider an understanding of the potential differences between the response of matter on nanosecond timescales to those that pertain on geological timescales to be of import, at least if claims of relevance of the former to the latter are to be made with any coherent degree of credence. Broadly speaking, the themes that we see as being ripe for investigation (and in many cases studies have already started) are as follows:

- An improved understanding of the boundaries and differences between shock and so-called quasi-isentropic compression.
- Investigations, across the length scales, of the mechanisms that underpin the plasticity that invariably accompanies uniaxial compression of solids, leads to substantial heating, and is associated with the dynamic strength of the material.
- The development of techniques to measure directly temperature during dynamic compression.
- An improved understanding of under what conditions phase boundaries seen under dynamic compression differ from those seen on longer timescales.
- The development of the study of liquids at high pressures.
- The use of dynamic compression in novel material synthesis.
- The use of small angle x-ray scattering (SAXS) and line-profile analysis to monitor crystallite sizes, voids, and defect densities.
- The development of experiments that use convergent, rather than uniaxial, geometries.
- The exploration of x-ray techniques that complement diffraction such that they give information about the electronic structure of matter, as well as its crystalline structure.
- Using advances in high-power optical laser technology to increase the repetition rate at which material can be studied, leading both to improved statistics, but also increased throughput and associated access for users.

We provide our views on the above issues below.

A. Shock and ramp compression

As outlined in Sec. I, initial dynamic studies of matter have concentrated on shock loading of materials. While there are very

good reasons to study matter under shock compression, compressing a material by a single shock does not allow the study of solids at the highest pressures, and in this regime will generally not be directly relevant to the study of matter within planetary cores. This is because the shock process itself is highly entropic, with the material behind the shock front being heated to very high temperatures. Indeed, even though, as a rule of thumb most metals have a melting point that increases as a function of pressure, we find that the Hugoniot (the locus of states that can be reached via shock compression) typically crosses the melt curve in the region of up to a few hundreds of GPa, as we have shown in our depiction of a generic material in Fig. 1 (as examples of real materials, Pb starts to melt under shock loading at just above 50 GPa¹⁸¹ and Ta at 300 GPa¹⁸²). Thus, in order to study solid-state matter at high pressure, compression via a single shock may not be appropriate. Indeed, as a reasonable approximation, if one follows the compression path toward a planet whose interior is believed to be convecting, the temperature gradient is constrained to be close to isentropic,¹⁸³ although it is acknowledged that in many cases a fully adiabatic model is overly simplistic.¹⁸⁴ Very crude arguments show that in the vast majority of cases, the temperature rises along an isentrope more gradually than the melt curve.¹⁸⁵ Therefore, to compress materials to the highest pressures, while keeping them solids, requires us to compress them quasi-isentropically, rather than via shock compression.

We take care to specifically use the term isentropic, rather than adiabatic compression: both the rapid compression of a shock and a far slower isentropic compression are adiabatic, in that only compressive work is done on the system, and the external driving force does not of itself directly supply heat. However, the shock adiabat results in significantly more heating than compressing more slowly along the isentropic adiabat.

The above realization immediately leads to the question of how slowly must we compress matter if we are to regard the process as close to isentropic? In the absence of plastic flow, the difference between a shock and dynamic compression that is close to an isentrope is simple to understand. In this case, uniaxial compression can be visualized in terms of a single chain of atoms. In the case of an elastic shock, the shock-front is at the atomic scale such that an atom in front of the shock has no interaction with it until its neighbor is accelerated toward it, imparting considerable kinetic energy in the compression process—i.e., it “overshoots,” with atoms at the shock front itself for a time shorter than a single oscillation having a closer interatomic distance than the mean distance between atoms behind the shock front. This simple picture of the difference between an elastic ramp and an elastic shock has been confirmed by MD simulations.¹⁸⁶

However, once the material starts to yield owing to the high shear stresses induced by the compression, the situation becomes more complex, and the demarcation between a shock and a ramp is less well understood. In this context, it is important to note that for the vast majority of experiments performed to date using optical laser ablation to compress materials for diffraction studies, the compression process, whether ramped or as a shock, is uniaxial in strain. That is to say, the total deformation of the material (deformation being comprised of elastic and plastic components) only changes along the compression direction. This requires that the

so-called deformation gradient matrix, F , be diagonal,

$$F = F_e F_p = \text{diag}(1, 1, \eta), \quad (12)$$

where F_e and F_p are the elastic and plastic deformation gradient matrices, respectively, and $\eta = V/V_0$ is the volumetric compression experienced by the crystal.

Once uniaxial compression of the material exceeds the yield point of the material (in the case of a shock, this is known as the Hugoniot Elastic Limit, or HEL), then the material will start to plastically flow to relieve the shear stress. Importantly, the plastic work performed (dictated by the time-integrated product of the relevant plastic stresses and strains) will give rise to heating of the material. Strictly speaking, therefore, it is impossible to uniaxially compress a material to the ultrahigh pressures (above the HEL) and keep the material on an isentrope—there will always be some degree of plastic work performed, and thus heat dissipated in the system,¹⁸⁷ and this is why the ramp-compression path depicted in Fig. 1 lies between the isentrope and the Hugoniot. In the case of a shock, the amount of work that must be dissipated is, to a good approximation, dictated by the integral of PdV between the Rayleigh line (this is the straight dashed line connecting the initial to final state, as shown in Fig. 3) and the cold compression curve. The dissipated work is, thus, represented by the shaded area in Fig. 3. Note this is only an approximation, as this neglects any residual strength that the material may still exhibit on the Hugoniot. However, and importantly, within this approximation, we see from the Hugoniot relations that if two shock parameters are measured, we know the increase in energy of the shock compressed material and, thus, when combined with knowledge of the cold compression curve, we can make reasonable estimates of the temperature.¹⁸⁸

For ramp compression, however, the situation is very different. Unless we know the integral of the plastic work done in relieving the shear strains built up during uniaxial compression, we have no information whereby we can plausibly estimate the temperature rise. Thus, crucially, we find that we need to understand strength at high pressure, and at high strain rates, if we are to predict where in temperature space, between the isentrope and the Hugoniot, we may lie. Indeed, this leads us to understand one of the major problems facing this field: uniaxial compression is favored (in large part as we then have tried and tested methods to determine the longitudinal stress via VISAR), but this inevitably means that plastic flow takes place, and this, in turn, means that plastic work is dissipated as heat. Quite how much plastic heating occurs depends on the time history of the plastic stresses and strains—a history that itself will depend on the time-dependent strength of the material. In the absence of knowledge of this plastic work history, we have no means to reliably estimate the final temperature of the material and, thus, do not know exactly where we lie in a (P, V, T) phase diagram. We return to this point in Sec. IV C, where we discuss current efforts to develop methods for temperature measurements, and Sec. IV B where we indicate possible directions of enquiry that may lead to an improved study of strength at these ultrahigh strain rates.

What we can assume, however, is that if we wish to keep the degree of plastic work, and thus heating, to a minimum, the

material must be compressed on a timescale that is long compared with that taken for an element of the same material to be compressed by a shock of the same strength. This, in turn, leads us back to our original discussion of the underlying differences between shock and ramp compression, but now in the presence of plasticity. It is at this juncture that we appeal to the empirical result, known as the Swegle–Grady relation,^{189–191} that when a plot is made of the Hugoniot stress, σ_H , behind the shock vs the maximum strain rate, $\dot{\epsilon}_m$ within the front for a given material, then for a vast array of different materials we find the relation $\dot{\epsilon}_m = A\sigma^4$, where A is a constant that depends on the material. Furthermore, for a wide range of materials $\dot{\epsilon}_m$ is found to be in the region of 10^9 s^{-1} once Hugoniot stresses reach values of order 10–100 GPa. As the peak strains themselves in this region are of order tens of percent, we readily deduce that even in the presence of plasticity the shock rise time in this pressure range is short compared with a nanosecond and surmise that, therefore, if the material is compressed on nanosecond or longer timescales, then the material will not undergo the same degree of heating as it does under shock compression.

There is compelling evidence that underpins the above picture. First, the diffraction experiments that have been performed using laser-plasma x-ray sources on the NIF and OMEGA facilities have readily demonstrated that, when ramp compressed on the timescale of several nanoseconds, the material remains solid into the TPa regime.^{3,53} Second, MD simulations also indicate that ramp compression, even on rapid timescales (but slower than shock compression) keeps the material cool.¹⁹² In those simulations, single crystals of Cu were compressed up to 250 GPa with a ramp of rise time of 300 ps, and it was shown that the temperature could be kept well below that produced by a shock, at least for the short period of time before the ramp steepened up to the strain rate determined by the S–G relation.¹⁹² This meant that only a few tens of nm of material at the surface of the crystal remained solid, but the basic concept was proven.

Further insight into when compression is in the ramp rather than shock regime can be gained from monitoring the rate of compression from a VISAR signal (if afforded by the temporal resolution of the instrument). The local Lagrangian sound speed, C_L is a function of the particle velocity, U_p , and we can define the strain rate as $\dot{\epsilon} = [1/C_L(U_p)] * [dU_p/dt]$.¹⁹³ The expectation is that a compression wave is in the ramp regime if the strain rate at a specific stress increases with samples of thickness for the same compression rate on the front surface—that is to say that the wave steepens as it propagates, and if the target were thick enough, would lead to shock formation. We illustrate this concept in Fig. 13, where we show an analysis of data obtained in an experiment where thin foils of Al, of thicknesses of 10, 20, and 30 μm , were ramp compressed up to 80 GPa.¹⁹³ The foils were mounted on a LiF window, which was well impedance-matched to the Al, and the response of the rear surface of the Al monitored via VISAR, providing a time-dependent particle velocity of the rear surface of the Al via an iterative characteristic method.¹⁹⁴ Figure 13 shows the local strain rate (as defined above) as a function of stress for the ramp waves in the three foils. Also shown in open circles is the maximum steady-shock strain rate measured by Swegle and Grady, and the green shaded area represents regions of stress and strain rate where we would expect quasi-isentropic behavior to hold, with

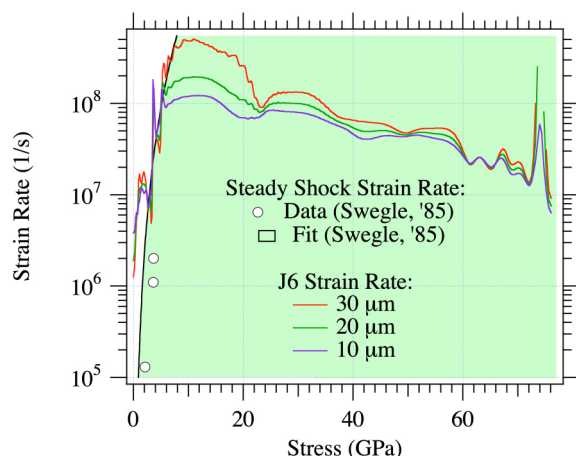


FIG. 13. A plot of strain rate (as defined in the text) as a function of stress for ramp-compression waves in a laser-shocked Al target of the three thicknesses shown. All three traces were measured in a single laser shot on a three-step target that was identified as “J6.” Data taken with permission from the experiment of Smith *et al.*¹⁹³

the demarcation line between the shaded and unshaded areas being determined by the S–G relation. It can be seen that in these experiments, at the higher stresses above approximately 10 GPa, the strain rates are below those expected in a shock, indicating true ramp compression. It is interesting to note that the experiments from which these data are taken indicate that compression along the quasi-isentrope revealed a stiffer response than models consistent with static and shock results, highlighting once more the importance of understanding strain rate-dependent strength. Indeed, if the rate-dependent strength was fully understood, and the total plastic work could be deduced, then accurate predictions of the temperature of ramp-compressed matter could be made.¹⁹⁵

We further note that owing to the non-linear response of materials, care is required in designing the pressure (and thus laser) profiles required for ramp compression, to ensure that portions of the ramp do not steepen up into a shock during the process. Examples of how this might be done for several ablators and materials have been undertaken by a study of the flow characteristics of materials under compression (i.e., as a function of their strength).¹⁹⁶

We end this section by noting that even if the compression of the target is not performed by means of a continuous ramp, off-Hugoniot states, lying closer to the isentrope, can also be reached by a series of shocks, rather than a single shock, and indeed a double-shock technique was the means by which Kraus and co-workers created diamonds from laser-shocked hydrocarbons at pressures around 150 GPa and confirmed their formation by femtosecond diffraction.¹⁹⁷

B. Strength and plasticity

A recurrent theme throughout our discussions has been the fact that in order to keep matter solid at high pressures, the rate of

dynamic compression should be such that the thermodynamic path followed is close to that of an isentrope, rather than the sample being shocked. Given that (at least to date) most dynamic studies employ uniaxial compression, such that the total strain (plastic plus elastic) transverse to the compression direction is zero, the sample potentially experiences high levels of shear stress, which must be relieved either via plastic flow, or via the process of polymorphic phase transitions, or both. The plastic work experienced during the relief of this shear stress will, to a large part, dominate the temperature rise of the sample (although temperature changes due to phase transitions also play a role). Some plastic work on the sample will also be expended in the generation of defects, with the fraction converted to heat being known as the Taylor–Quinney factor,¹⁹⁸ with the thermal component thought to dominate, even at high strain rates and high defect densities,¹⁹⁹ and as seen in MD simulations.¹⁴⁴ The temperature rise during dynamic compression is, thus, intimately linked to material strength.

The incorporation of strength models into hydrodynamic descriptions of material response under dynamic compression has a long history. The main thrust of early implementations has been to determine expressions for the yield strength, Y , in the von Mises sense, and of the shear modulus G , as a function of the relevant parameters, i.e., strain, strain rate, temperature, and pressure. Two well-known models of this form are those due to Steinberg *et al.*²⁰⁰ and Preston *et al.*²⁰¹

Ultimately, one would like to understand the physics of plasticity across a multitude of scales. The motion of one atom with respect to another and, thus, the stresses required for plasticity, is ultimately linked to the strength of atomic bonds, which break during dislocation motion. At another level, the velocity at which dislocations move as a function of shear stress plays a significant role, as does their number, given that the plastic strain rate is governed by Orowan’s equation. Dislocations can also interact with each other, leading to hardening effects. This approach, whereby information about bonding at the atomic level is determined via, for example, density functional theory, and dislocation mobility by classical molecular dynamics calculations and so forth, is known as the multiscale approach, and a review of such methods has been provided by Rudd *et al.*,²⁰² and one detailed form of this approach has been constructed for tantalum, and has become known as the Livermore Multiscale Model,²⁰³ discussed further below.

We note that if a given strength model can be trusted, then a calculation of the plastic work expended under ramp compression can be made and, thus, the temperature rise predicted. For example, in work on the NIF where Ta was ramp compressed to approximately 600 GPa, the wave profiles determined from VISAR and the iterative Lagrangian analysis were compared with those from LASNEX hydrocode simulations, where the hydrocode incorporated the Steinberg–Guinan model,¹⁹⁵ good agreement between predicted and observed wave profiles enabled the temperature rises to be deduced. In these experiments, after an initial small shock, the Ta target was compressed on a timescale of order 10 ns. As the ramp wave steepens during the compression, different parts of the target experience different compression rates and, thus, have their temperatures raised by differing amounts. As an example, for compression to 600 GPa, the code indicated that shock compression would take the material above the melting point, and to a

temperature of 24 000 K, whereas under ramp compression, at a position $63\text{ }\mu\text{m}$ from the surface at which pressure is applied, the temperature would have been 3850 K, keeping the material solid.

As said, a more sophisticated model than the Steinberg–Guinan model referred to above has been developed by workers at LLNL and is known as the Livermore Multiscale Model (LMS).²⁰³ It is designed to bridge various length scales by, for example, obtaining data about dislocation mobility from molecular dynamics simulations and then using an analytic form based on these data as input to the model. In this model, thus far applied to tantalum, a number of slip systems α are taken into account, and the rate of an amount of slip on each system, $\dot{\gamma}^\alpha$ assumed to follow Orowan's equation: $\dot{\gamma}^\alpha = \rho^\alpha b^\alpha v^\alpha$, where ρ^α is the mobile dislocation density, b^α is the magnitude of the dislocation density, and v^α is the average velocity of mobile dislocations on the relevant slip system, with this velocity being a function of the effective resolved shear stress, τ_{eff}^α , with this relationship being fitted to MD simulations of screw dislocation mobility. The multiplication and annihilation of dislocations is taken into account by assuming

$$\dot{\rho}^\alpha = R \left(1 - \frac{\rho^\alpha}{\rho_{\text{sat}}^\alpha(\dot{\gamma}^\alpha)} \right), \quad (13)$$

where R is specific to the material, and ρ_{sat}^α a saturation dislocation density that depends on the strain rate, and is constrained by larger scale dislocation dynamics models. The model has been used in hydrodynamic simulations with some success to predict the growth rate of the Rayleigh–Taylor hydrodynamic instability in laser-driven targets.^{204,205}

Ideally, as noted above, one would like to be able to use such models to predict temperature rises in ramp-compressed targets and compare those calculated with values deduced experimentally. However, as we discuss further in Sec. IV C, accurate temperature measurements are proving challenging and remain an area for further investigation and development. That said, direct links between models such as the LMS model and experimental results can be made, in that as the model takes into account specific slip systems and the degree of plasticity active on each of them, it as such encodes information on the way in which plastic flow changes the texture of the target. It is in this context that recently a version of the LMS model has been incorporated into a crystal plasticity finite element code by Avraam *et al.*²⁰⁶ and then used to predict the lattice rotation observed in the Ta experiments of Wehrenberg discussed in Sec. III A. As the finite element code keeps track of the orientation of lattice planes with a spatial resolution much smaller than the size of a grain, but can incorporate multiple grains, simulated diffraction patterns can be generated that can be compared directly with the experimental data.

In order for the predicted lattice rotations to match the experimental data, Avraam *et al.* needed to add a further term to the LMS model in order to take into account the homogeneous nucleation of dislocations. When this term was included, excellent agreement was found, as can be seen in Fig. 14. In model 2 shown in the figure, nucleation of dislocations occurs when a threshold stress of 5.5 GPa is reached at the shock front. It can be seen that this model correctly predicts the “knee” in the graph of the rotation angle vs

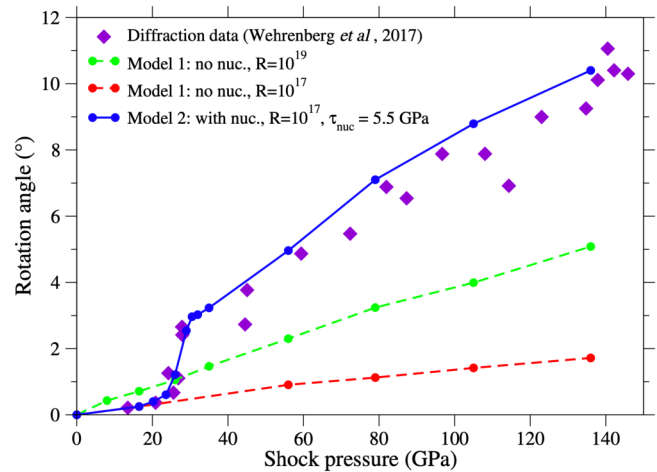


FIG. 14. The predictions of lattice rotation from the crystal plasticity finite element modeling of Avraam *et al.*²⁰⁶ Model 2 is able to capture the low- and high-pressure regimes. Model 1 is based on the LMS model and accounts for dislocation multiplication and annihilation, with multiplication rate controlled by parameter R . Model 2 additionally incorporates a nucleation process, with nucleation threshold $T_{\text{nuc}} = 5.5$ GPa, as described in the text. Figure reproduced from P. Avraam *et al.*, arXiv:2108.05166v2 [cond-mat.mtrl-sci] (2021). Copyright 2018 Author(s), licensed under a Creative Commons Attribution (CC BY-NC-ND 4.0) license.

shock pressure, occurring around 27 GPa. What the authors find is that in the lower pressure regime the kinetics are relatively slow resulting in two competing slip systems acting in a balanced way, giving rise to a relatively small net lattice rotation, whereas above the nucleation threshold the kinetics are faster, with one slip system dominating, leading to a larger net lattice rotation, though significant plasticity occurs in both regions.

It is also worth noting that even prior to the work of Avraam, it had been pointed out that the models used originally to model the Wehrenberg data were somewhat deficient, in that they assumed that only a single slip system was active in each grain, and relied on the classic Schmid model^{141,142} for lattice rotation discussed in Sec. III A. This model assumes that line elements of the material parallel to the compression axis remain conserved. In previous laser-plasma shock experiments that viewed rotation in single crystals,²⁰⁷ the Taylor model was used,¹⁹⁸ where line elements perpendicular to the compression axis are conserved. However, it can easily be shown that the situation is more complex for single slip when the deformation of the crystal takes place under the boundary conditions of uniaxial compression, and Heighway and Wark have shown that neither of these classic models correctly predicts the degree of rotation for a single crystal subject to uniaxial compression and undergoing single slip;²⁰⁸ furthermore, there is good evidence from MD simulations that multiple slip systems are active in these experiments.²⁰⁹ Of course, in real polycrystalline materials, such as those observed in the Wehrenberg experiments, while the condition of uniaxial strain must hold globally, it need not hold locally owing to grain–grain interactions.²¹⁰ It is here that

the finite element crystal plasticity model shows its advantages, in that it can model a large number of realistically sized grains, something that is at present still beyond the computational capabilities of MD simulations.

In our view, the work referenced above is only just beginning to give us an insight into deformation processes that give rise to temperature rises under ramped dynamic compression. Where some insight has been gained thus far it is mainly in simple metallic systems. Little attention has yet been given to the underlying plasticity mechanisms that come into play in more complex materials, and perhaps particularly materials that are covalently bonded, where different processes may be at play. For example, in the ramp compression of diamond targets to 2 TPa, discussed in Sec. I B, the authors note that the observation of solid diamond at these pressures implies that the material is less strong than they initially thought. While some work has been performed to investigate this, it still largely relies on the input of empirical parameters,²¹¹ and possibilities such as a low Taylor–Quinney factor have also been suggested.²¹²

In conclusion of this section, therefore, we would maintain that an increased understanding of plasticity at the lattice level is not only necessary from the perspective of those interested in the fundamentals of rapid deformation for its own sake, but is a necessary prerequisite for providing a capability of predicting the temperature rises to which materials will be subject under uniaxial loading at different strain rates.

C. Temperature measurements

Under dynamic compression, the density of the target can be determined from the diffraction pattern, and the pressure (or more accurately, the component of the stress along the shock propagation direction) can be deduced from VISAR. However, as mentioned in several places above, accurate measures of the temperature have yet to be developed. This problem is particularly acute in the case of ramp compression, where the degree of plastic work experienced by the sample is hard to quantify. In contrast, in the case of shock compression, one has some measure of the total internal energy imparted to the sample by the shock, as this is the difference between the Rayleigh line and the low temperature isotherm, as shown in Fig. 3. Indeed, such a knowledge of the energy budget, along with other experimental parameters, has recently been used to constrain the melting temperature of Ta under shock compression.²¹³

One method that has been pursued for many years in the field of shock physics is optical pyrometry,²¹⁴ whereby the thermal emission from the rear surface of a sample is recorded (often through a window that is transparent). However, it has been shown that these experiments are hampered by small optical depths and thermal conduction effects such that the surface temperature observed may not be representative of the bulk temperature.²¹⁵ The technique requires not only very accurate calibration, but also a knowledge of the wavelength-dependent emissivity of the sample, which itself may change upon compression. That said, at high enough temperatures, above several thousand Kelvin, a combination of reflectivity measurements with pyrometry can allow good temperature measurements to be made at the relatively high

temperatures found along the Hugoniot,²¹⁶ though the technique is less suitable for ramp compression, where the sample is kept much cooler and thermal diffusivity effects are always present.

It has been proposed that temperature could, in principle, be deduced via elastic scattering by monitoring the relative intensity of Bragg peaks and utilizing the Debye–Waller (DW) effect. This effect exhibits itself in a relative reduction of the intensity of the diffracted x rays as a function of the reciprocal lattice vector associated with the Bragg scattering such that, in a simplified form of the DW effect for a material with a monatomic basis, the scattered intensity is given by

$$I \propto I_0 \exp(-2B \sin^2 \theta / \lambda^2), \quad (14)$$

where $B = 8\pi^2 \langle u^2 \rangle$, with $\langle u^2 \rangle$ being the mean squared displacement of the atom from its average position. The physics of the effect is that thermal motion implies an rms deviation of an atom from its lattice point and, thus, the x rays are not scattering from a perfect lattice. When the momentum transfer of scattered x rays increases (as it does within increasing reciprocal lattice vector, or $\sin \theta / \lambda$), a given displacement of an atom from its ideal position induces a larger random phase into each scattered x ray, reducing the overall observed intensity. The displacement of the atoms from their perfect positions is a function of both the temperature and the Debye temperature, θ_D of the material (given that the Debye temperature is related to the speed of sound and, hence, bond stiffness). This, in turn, means that the exponent in Eq. (14) is proportional to $G_{hkl}^2 T / \theta_D^2$, where G_{hkl} is the reciprocal lattice vector of the relevant Bragg reflection.

Very few studies of how the Debye–Waller effect might exhibit itself in dynamic compression experiments have been undertaken using femtosecond x-ray diffraction, although some initial computational analysis has been embarked upon.^{217,218} Some work has been performed in using the same phenomenon in absorption spectroscopy experiments, given that the same physical effect occurs in Extended X-ray Absorption Fine Structure (EXAFS). In such experiments, the absorption coefficient above an x-ray absorption edge is modulated due to scattering of the photo-ejected electrons from surrounding atoms, and their deviation from perfect lattice positions exhibits itself in a similar temperature-dependent damping of the modulations in the absorption coefficient. This technique has been used to deduce the temperature of iron ramp compressed to 560 GPa,^{219,220} although the relative errors in the measurement in those experiments were quite high, often exceeding $\pm 20\%$.

It could be argued that using the DW approach in elastic Bragg scattering to measure temperature may be hampered by texturing effects: the texture of a target will evolve under compression, as lattice planes can rotate under compression due to slip. How this occurs under uniaxial conditions is only just starting to be investigated,²⁰⁸ but if the degree of texturing can be understood, and indeed retrieved from the diffraction data, the non-random orientation of the grains within the sample could then be accounted for any DW analysis. We note that texture should not be such an issue in EXAFS measurements, as here the DW effect is occurring at the local level, and the absorption is independent of orientation.

However, in both cases, the extraction of temperature relies on accurately knowing the effective Debye temperature of the system, which is itself a function of compression—that is because what is actually deduced from the relative intensity of the Bragg peaks is $G_{hkl}^2 T / \theta_D^2$, rather than the absolute temperature itself. However, information about θ_D is implicit in the knowledge of the pressure-density curve (given that the Debye temperature is also related to the local speed of sound). That said, several static studies on highly defective nanocrystalline material have shown that the defects themselves can modify the effective Debye temperature by some considerable margin, further complicating this approach to temperature measurement,²²¹ and this has been confirmed in the case of materials under shock compression.²²² While further investigations are required, using the relative intensity of Bragg peaks to provide temperature information remains an attractive prospect, as such measurements could in principle be made on a single-shot basis.

We mention in passing one potentially interesting aspect of the DW effect in the context of ramp compression. While the temperature and length of the reciprocal lattice vector will increase under ramp compression, in general so will the Debye temperature, owing to the curvature of the PV hydrostat. It is, thus, pertinent to ask which effect dominates—because if the increasing θ_D is most important, it is possible that higher order diffraction peaks will actually get relatively brighter under compression. Indeed, it can be shown that was the compression perfectly isentropic (which it will not be, owing to plastic work), then in a simple Grüneisen model of a solid, this effect will occur for most solids, as it merely requires a Grüneisen parameter greater than $2/3$.^{185,218}

In the context of the difficulties in extracting temperatures using the methods discussed above, a novel method (for dynamically compressed solids) that has been proposed is that of the inelastic scattering of x rays from phonons.²²³ As well as the elastic scattering observed when x rays meet the Bragg condition, incident x rays of energy $\hbar\omega_i$ and of wavevector \mathbf{k}_i can scatter from phonons of wavevector \mathbf{q} and energy $\hbar\omega_{ph}$, with the scattered x-ray photon having wavevector $\mathbf{k}_s = \mathbf{k}_i + \mathbf{G}_{hkl} \pm \mathbf{q}$, and frequency $\omega_s = \omega_i \pm \omega_{ph}$, with the \pm denoting the absorption or creation of a phonon during the process. We note that the most energetic phonons in the sample will have energies of order $k_B\theta_D$, which, given typical Debye temperatures are of the same order of magnitude as room temperature, implies phonon energies of up to a few 10 s of meV. In contrast, the incident x rays have energies of many keV and, thus, the change in energy of the x ray upon scattering is extremely small, and the spectral resolution required for such a measurement must be high, with $\Delta E/E$ better than 10^{-5} by some margin.

However, given that the relative intensity of the Stokes and anti-Stokes peaks of inelastically scattered x rays (i.e., photons during the scattering process have either created or annihilated a phonon) is determined by the principle of detailed balance for a system in thermodynamic equilibrium,^{224–227} if such a technique could be employed during dynamic compression it would give an absolute temperature measurement, and not be reliant, for example, on knowledge of θ_D .^{223,228} However, the transient nature of the compression process means the crystal is only in the state of interest for a few nanoseconds at most. Owing in part to the very high resolutions required, inelastic x-ray scattering measurements

are “photon-hungry,”²²⁶ and it might seem that the prospect of retrieving information about the phonon modes on such timescales is unfeasible. Nevertheless, despite the considerable challenges that such measurements pose, progress is being made toward the development of inelastic scattering techniques on these short timescales. As noted above, FELs have an enormous peak spectral brightness. Indeed, recent work on both the Linac Coherent Light Source (LCLS)²²³ and at the European XFEL (EuXFEL)^{228,229} has demonstrated inelastic scattering from static, unshocked samples of almost perfect diamond single crystals. The temperature of samples at both ambient and elevated levels could be determined with an error of less than 8%. In these experiments, the photon numbers were low and just a few photons were collected for every FEL shot, but this signal level can be increased significantly by seeding of the FEL.^{230,231}

These initial experiments at LCLS and EuXFEL were conducted at an x-ray energy of 7.49 keV, utilizing a Si (533) analyzer crystal. The resolution of the setup was approximately 44 meV. As with inelastic scattering measurements performed at synchrotrons, this can, in principle, be improved further (at the expense of a further reduction in photon numbers) by, for example, using a higher x-ray energy and, given the analyzer operates with a Bragg angle of close to $\pi/2$ in order to maximize dispersion, an analyzer crystal with a smaller lattice spacing.^{225,232} For example, resolutions better than 3 meV have been achieved at synchrotrons using the Si (999) reflection at 17.8 keV.²³³

While the static measurements performed at FELs cited above show promise, there are other complications that may need to be born in mind. In these inelastic scattering measurements, the x rays are collected between the Bragg peaks. However, there will still be some elastic scattering present at this position due to defects in the sample, and the dynamic compression process itself will introduce significant defects owing to the plastic deformation processes incurred. To date, little consideration has been given to this problem—it could be that the intensity of this quasi-elastic scattering could overwhelm any inelastic signal, unless the resolution of the setup is sufficient. Preliminary computation work has started in this area, and MD simulations of shocked single crystals of Cu have demonstrated the effects of the copious stacking faults on the observed signals.²³⁴

Even with seeding it is likely that inelastic scattering experiments will need multiple shots to accumulate sufficient signal for accurate temperature measurements. Thus, this technique will require combination with a high-repetition-rate high-energy nanosecond optical laser for compressing samples if experimental data are to be acquired on realistic experimental timescales. Indeed, this is one of the motivations for the building and placement of the DiPOLE laser²³⁵ at the EuXFEL, DiPOLE being a 100 J diode-pumped laser capable of delivering pulses of a few nanoseconds duration at 10 Hz. As noted above, it may be that useful temperature information could be extracted more easily by use of the DW effect, which only requires a single shot, but in any event inelastic scattering experiments could prove extremely useful in that they should allow extraction of some information about phonon dispersion curves under compression (which themselves could provide information on the effective value of θ_D). It has also been pointed out that very high inelastic scattering, if employed away from a

forward scattering geometry, would be sensitive to the bulk (particle) velocity of ramp-compressed material, in that the scattered signal will be Doppler shifted by a degree detectable with these high resolutions.²³⁴ While the accuracy of such a particle velocity measurement cannot compete with VISAR, it would comprise a near instantaneous measurement within the material, rather than relying on measurement of a surface or interface velocity.

Alongside an understanding of the plasticity that gives rise to the major part of the temperature increase under uniaxial compression, we consider the development of techniques to measure such temperature rises accurately *in situ* to be an area ripe for further development. As we have noted above, each technique proposed to date appears to have its advantages and disadvantages, but as of yet no clear favored candidate has emerged.

D. Phase boundaries under dynamic compression

As noted previously, it has long been known that the locations of the phase boundaries between different high-pressure phases can be dependent on the rate of compression.¹⁷⁵ However, early structural studies on Bi and Sb at the LCLS,^{121,176} which have directly determined the different structural forms obtained on shock compression, have shown that not only do the phase boundaries move, but also that one can obtain structures under dynamic compression that are not been seen in longer-timescale DAC experiments (see Fig. 11). Similarly, early FEL experiments have also shown phases that are seen in static compression studies are sometimes not seen on dynamic compression. One example is in H₂O, where ice-VI, the tetragonal form of H₂O ice seen above 1 GPa on the slow compression of liquid H₂O at 300 K, is not seen on compression on either millisecond²³⁶ or nanosecond²³⁷ timescales, but rather that super-compressed H₂O crystallises directly into the higher-pressure ice-VII at ~2 GPa. Further ramp-compression experiments over 100 s of ns at the Z-machine²³⁸ have shown homogeneous crystallization of the liquid directly into ice VII at 7 GPa, while nanosecond isentropic compression at OMEGA reported the liquid-ice-VII transition to occur at least 8 GPa.²³⁹ The ability to determine the actual crystal structures observed under dynamic compression is providing important new light on the behavior of such materials. However, we have yet to determine when, why, and how the changes in phase boundary locations and structures are obtained in materials under uniaxial compression and this is a topic under active investigation. Such changes might be driven by shear effects or they might be a kinetic effect that is related to the timescale of the experiment. The observation that ice-VI is “missing” in both nanosecond and millisecond timescale experiments provides invaluable input to our current understanding. In any case, great care must obviously be taken in assuming that the structures and physical properties obtained from short-lived experiments can be applied without caveats to our understanding of geoplanetary bodies, the internal structures of which have evolved on geological timescales.

It is likely that the effects of material strength and shear will be relevant to developing our understanding in this area. Such effects might be mitigated by the use of novel target designs—e.g., by the use of non-planar compression (see below), or by embedding materials of interest in a “weak” matrix,¹²⁴ much as DACs use

a pressure transmitting medium in order to obtain more hydrostatic conditions. Further insight will be gained from more systematic studies of P-T space in order to map phase boundaries over extended ranges. At present, phase transitions have been determined mostly along either the Hugoniot or a (quasi)-isentropes (see Fig. 1). Locating phase transitions at other locations (such as location “A” in Fig. 1) will require both the inventive use of pulse shaping, in order to move away from the Hugoniot and isentropes, and a solution to the problem of measuring the sample temperature, an issue discussed in Sec. IV C.

E. Prospects for the study of the structure of liquids at ultrahigh pressures

The study of liquid phases and liquid-liquid phase transitions has long been a topic of active interest in the static compression community. While first-order transitions are commonplace in solids, they are very much rarer in liquids. The clearest such transition at high pressures has been seen in phosphorous, where there is a transition from a molecular-liquid to polymeric form at ~1 GPa and ~1400 K.²⁴⁰ While there have been numerous other claims for liquid-liquid transitions in a range of other materials at high pressure,²⁴¹ both the evidence for, and nature of, the transitions is less clear than in the case of phosphorous.

When trying to determine the existence and nature of such transitions using diffraction, the key issues in static compression experiments are the limited sample volume, the need to contain the liquid sample over extended periods while preventing chemical reactions with the gasket/diamonds, the structured background arising from Compton scattering from the diamond anvils, and the limited Q-range of the diffraction data, which is constrained by the pressure cell housing and the choice of x-ray wavelength.²⁴² As a result, x-ray data are typically only collected to a maximum-Q of 8–10 Å^{−1}, and sometime much lower,²⁴³ as opposed to the ranges of 25 Å^{−1} used in ambient-pressure x-ray studies, and values of 30–50 Å^{−1} obtained in neutron studies.²⁴⁴

Studies of liquid phases of a number of materials have already been made at the LCLS to P-T conditions of 190 GPa and 10 000 K,^{121,179,245,246} and changes in coordination have been reported in Bi¹²¹ and Sn.¹⁷⁹ Such studies have revealed some of the inherent advantages of using dynamic compression techniques at FELs to conduct such experiments. First, the accessible P-T conditions are greatly extended over those available in a laser-heated DAC, and the timescale of the FEL experiments precludes reactions between the sample and its surrounding,²⁴⁷ even at these extreme temperatures. Second, the volume of the dynamically compressed sample is much greater than that compressed in a DAC, and the incident x-ray beam is also typically larger, so the diffraction signal is much greater. Third, the scattering from the sample is not constrained by the target environment. And finally, the absence of the diamond anvils, and the vacuum in which dynamic compression experiments are conducted, means that anvil and air scattering are absent. Only scattering from the low-Z ablator, if present, and x rays resulting from the ablator plasma, provides additional background. Despite these advantages, the Q-range of the liquid data that has been collected at the LCLS to date is very similar to that

collected from samples in DACs as a result of the current limitations in the lower x-ray wavelengths at FELs.

Such limitations will be less constraining in the future, with the availability of higher-energy radiation at both FELs such as EuXFEL and LCLS-HE, and synchrotrons such as PETRA-IV. On the HED beamline at EuXFEL, a Q -range up to 12 \AA^{-1} can be obtained using a 20 keV x-ray energy, which, while an improvement, is still well short of the range accessible at ambient conditions of $25\text{--}30 \text{ \AA}^{-1}$.²⁴⁴

While the use of higher energy x-ray harmonics from the FEL and synchrotron undulators would provide access to an extended Q -range,²⁴⁸ this would be accompanied by a decrease in flux and scattering intensity (which scales as λ^3). While the latter could be compensated for by using thicker samples made possible by the reduced x-ray absorption at higher energies, compressing such samples homogeneously would be more difficult. For molten phases, especially hot molten phases accessible along a Hugoniot, there is probably little point in extending the Q -range to 25 \AA^{-1} and above as there will be no structural features in the data at these momentum transfers. But data at high values of Q do aid data normalization as they help in scaling the scattering data to follow the average total scattering curve of the sample. This means that the high- Q limit of the scattering is better behaved and, as a result, the Fourier-transformed pair distribution function will contain fewer of the Fourier truncation ripples that arise through the limited Q -range of the data.

F. Novel material synthesis

The recovery of cubic diamond from shocked graphite was first reported in 1961, sparking great interest in shock-induced transitions in carbon.²⁴⁹ The possibilities of using shock compression to generate novel polymorphs were given further impetus in 1967 by the discovery of a shock-induced hexagonal form of diamond,²⁵⁰ which had also been synthesized using static techniques,²⁵¹ and later named lonsdaleite,²⁵² in fragments recovered from Barringer Crater in Arizona. Since these pioneering studies, shock compression has become a standard technique for synthesizing micro polycrystalline diamond powders (see, for example, Ref. 253), as well as being used to synthesize other industrially useful polymorphs,²⁵⁴ while recent experiments at the LCLS have shown that diamond can be formed directly from plastics using double shock compression techniques.¹⁹⁷

The successful generation and subsequent recovery of shock-generated high-pressure forms clearly requires the relevant polymorphs to exist at extreme conditions, and then be stable, or perhaps more likely metastable, at ambient conditions. While early studies utilized a “shock and look” approach to synthesis, the advent of electronic structure calculations, coupled to structure searching, now enables novel structural forms to be “found” on the computer, and their (meta)stability at ambient conditions established prior to experimental study.²⁵⁵

A key example is the so-called BC8 phase of carbon, a metastable structural form long known to be created on pressure decrease from the high-pressure phases of Si and Ge.^{256,257} The same BC8 structure is calculated to be the stable and metallic form of diamond above 1.2 TPa,^{258,259} and so its equation of state and

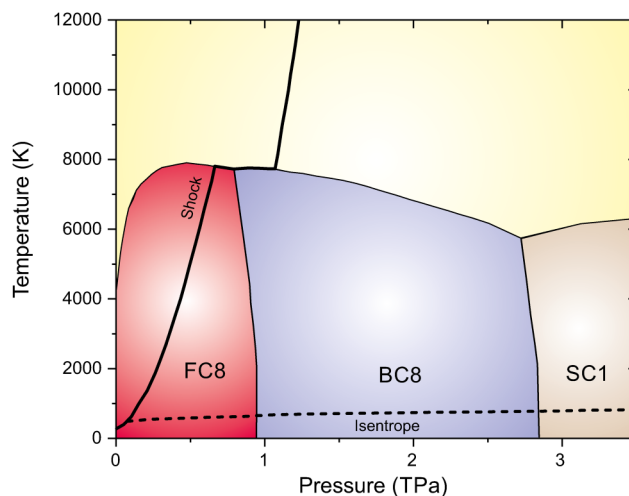


FIG. 15. The phase diagram of carbon to 3.5 TPa and 12 000 K, showing the DFT predicted phase boundaries between the diamond (FC8), cubic-BC8 and cubic-SC1 phases, and the Hugoniot and isentrope. Adapted from Fig. 1 in Ref. 3.

physical properties are of great importance for devising models of Neptune, Uranus, and white dwarf stars, as well as of carbon-rich exoplanets.^{260,261} BC8-C is also calculated to be a superhard material and to be metastable at ambient conditions.²⁶² Its synthesis might, thus, provide a new important industrial abrasive. A schematic of the carbon phase diagram is shown in Fig. 15.

Experimental searches for BC8-C have so far been unsuccessful to pressures as high as 2 TPa, well in excess of the calculated equilibrium phase transition pressures of 1 TPa.³ At present, only ramp-compression experiments at MJ-class lasers such as NIF and LMJ are capable of generating the P-T conditions necessary for synthesizing BC8-C on compression. And if such experiments are successful in making the high-density phase, then the sample volume recovered will be measured in μm^3 .

The recent development of high repetition rate lasers now offers the exciting opportunity for the mass production of shock-synthesized materials at lower pressures. For example, silicon possesses a number of dense polymorphs that can be recovered as metastable phases at ambient pressure after initial compression to $>15 \text{ GPa}$.²⁶³ The dense R8 polymorph of Si, a rhombohedral distortion of BC8-Si, is a narrow bandgap semiconductor, which is predicted to have a greater light absorption overlap with the solar spectrum than diamond-structure Si,¹⁰⁶ making it well matched for solar power conversion. As said, the DiPOLE laser installed on the HED beamline at the European XFEL has a repetition rate of 10 Hz, and with suitable targets will enable high-density Si polymorphs to be recovered in cm^3 volumes.

Our ability to predict what phases will be observed in such experiments has been greatly improved by the widespread use of structure prediction methods to determine the lowest enthalpy structure at a particular pressure.^{255,264} Such predictions have been made to multi-TPa pressures in some materials, and even to a

petapascal in carbon,²⁶⁵ well in excess of those currently accessible via experiment. However, such calculations are typically conducted at 0 K.

Fortunately, many structure searching studies also now publish lists of candidate structures which, while not having the lowest enthalpy (at 0 K) at any pressure, are competitive in enthalpy—see, for example, Refs. 266 and 267. Such structures then offer finite-temperature alternatives to those identified at zero-temperature. By precalculating the diffraction patterns from such structures, and comparing them to those observed in experiments, it will be possible to interpret the high rep-rate diffraction data in real time.

G. Small angle scattering and line-profile analysis

We note that the diffraction that we have been discussing up to now has been either wide angle scattering (WAXS) from crystal-line materials, that is to say Bragg diffraction, allowing the discernment of crystal structure, or scattering from liquids. In addition to such scattering, however, information obtained with much lower momentum transfer could also be of great use in dynamic compression studies, as small angle scattering (SAXS) provides information on irregularities within the crystal that exist on length scales far greater than the lattice spacing. To date, very little work has been performed with FELs using SAXS to study shock or ramp-compressed samples, however, that which has been undertaken has been highly successful. Coakley *et al.* used SAXS (in combination with WAXS) to monitor void evolution and growth during the rarefaction and spall phase that ensued when a laser-shocked copper target unloaded.²⁶⁸

One immediate lesson from the work of Coakley *et al.* is that the targets they were shock compressing, having been manufactured by vapor deposition, and were not initially fully dense—that is to say, voids were present from the start. This could be deduced from the SAXS signal of the unshocked target. Indeed, their data show these voids closing up as the target was initially compressed. This void closure will itself lead to another heating mechanism, beyond standard plastic work.

A further question of interest is to what degree can we learn about the dislocation densities present under shock conditions from an analysis of the line profiles in WAXS? The strained regions of the crystal that surround dislocations give rise to distinctive changes in the line profiles of the diffracted x rays, and there is a long history of using line-profile analysis in static experiments to deduce dislocation density. Furthermore, in the particular case of stacking faults in face-centered metals, the faults give rise to angular shifts in lines with certain values of $\{hkl\}$ which can be used to determine stacking fault densities.^{269,270} This comes about as a stacking fault that looks like a thin sheet of hcp material embedded in the fcc lattice, and as such each fault introduces a phase difference between the x rays and bulk fcc material. Indeed, an analysis of x-ray line shifts and line profiles has allowed stacking fault densities to be measured in laser-shocked gold at pressures up to 150 GPa using 100 ps pulses of x rays from a synchrotron source.⁸¹

We envisage that a combination of knowledge of defect density gleaned from line profiles, alongside information on the

slip systems which are active, and the overall degree of plastic strain, will provide a rich array of information that can inform higher-level plasticity models and our understanding of the dynamic deformation processes. In addition to providing information on defect densities, the line profile of the diffracted x rays can also provide information on the size of the diffracting crystallites and, hence, can give insight into the mechanisms and rates of phase transformations. For example, Gleason *et al.* have already used this technique at LCLS to monitor the nanosecond-timescale nucleation and growth of nanocrystalline stishovite grains in laser-shocked amorphous fused silica.²⁷¹ We show the results of those experiments in Figs. 16 and 17. Figure 16 shows the diffraction from the amorphous silica sample and the evolution on a nanosecond timescale of the distinct diffraction peaks from the crystalline stishovite phase. There is clearly a narrowing of these peaks as a

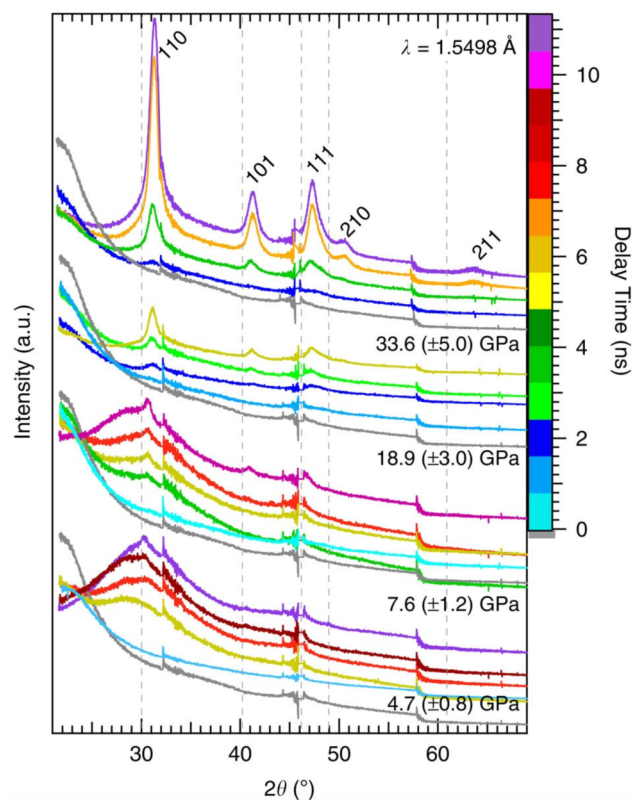


FIG. 16. Diffraction data showing the emergence of the stishovite crystalline phase from shock compressed amorphous silica for various shock pressures as a function of time. The stishovite peaks are labeled at the top; ambient condition positions (gray dashed lines). The traces are clustered according to applied pressure where each color indicates a different delay time (gray is x ray only—i.e., the unshocked amorphous phase). The data are offset along the y-axis for viewing clarity. Discontinuities in the traces are seen at scattering angles (2θ) of 32.5° , 46.0° , and 58.0° are due to spacing between the application-specific integrated circuits of the detectors. From A. E. Gleason *et al.*, Nat. Commun. **6**, 8191 (2015). Copyright 2015 Author(s), licensed under a Creative Commons Attribution (CC BY) license.

function of time and an analysis of their width enabled Gleason *et al.* to deduce the growth of the nanometer-scale grains as a function of time, as shown in Fig. 17.

H. Convergent geometries

The combination of dynamical compression techniques with ultrafast x-ray diffraction has, to date, been undertaken almost exclusively in planar geometries, with the diameter of the laser pulse being far greater than the thickness of the material of study, ensuring that the material is compressed under conditions of uniaxial strain. We have discussed above how it is the relief of the large shear stresses induced by this approach that leads to

significant plastic work heating of the target. However, planar compression is inherently inefficient at producing high pressures, and it is well known that pressure amplification occurs in convergent geometries—indeed, this is the basis of the underlying physics behind the design of experiments aimed at achieving laser-driven inertial confinement fusion (ICF),^{92,272} where keeping the fuel on a low adiabat (i.e., closer to an isentrope) is also of importance. The question, thus, arises as to why such a planar geometry is exclusively used? Our view would be that perhaps the primary reason is that such a geometry allows the use of the VISAR diagnostic (see Sec. II B) for pressure measurements, and if such a direct measure of pressure were to be sacrificed for the achievement of higher

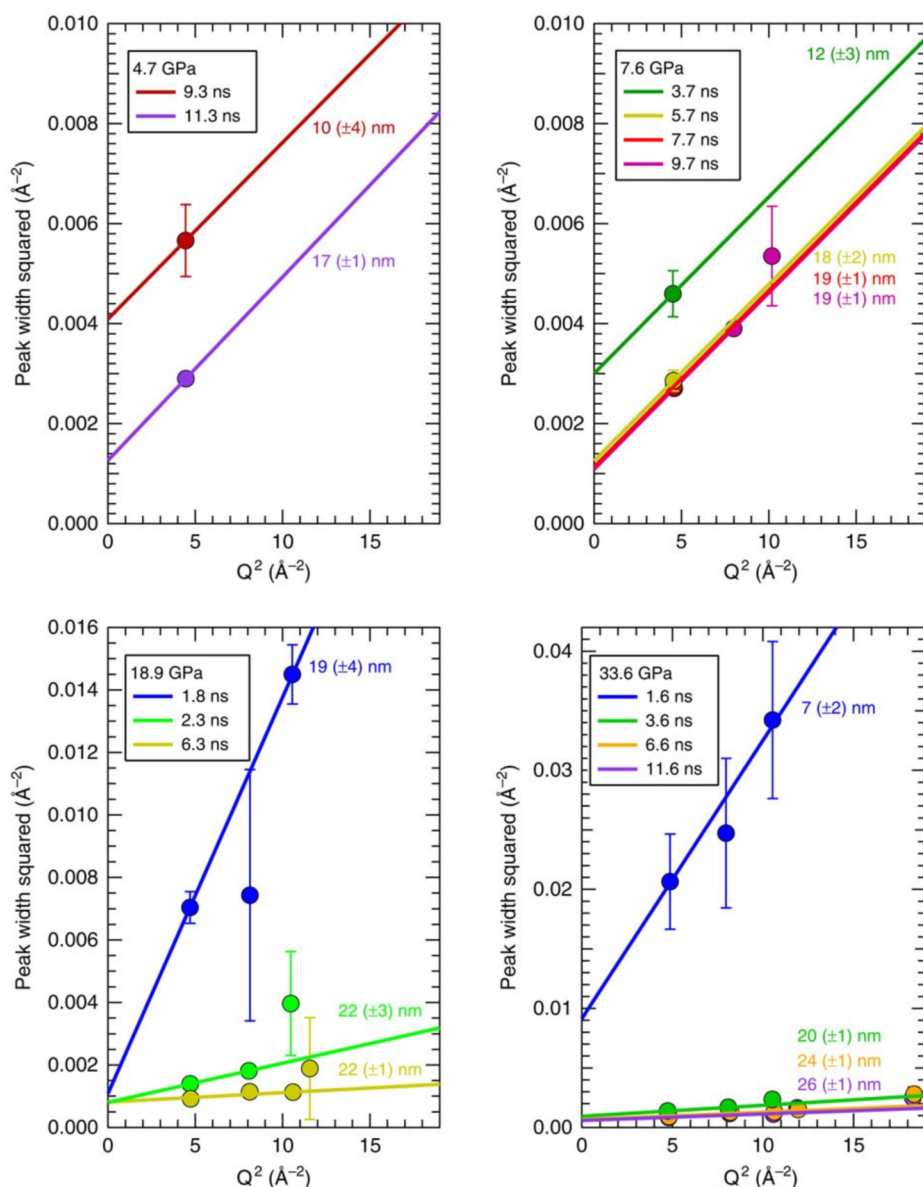


FIG. 17. The results of an analysis of the peak widths in Fig. 16 showing the peak width as various pressures and times as a function of the momentum transfer, $Q = 4\pi \sin \theta / \lambda$. The solid lines indicate expected peak widths for various grain sizes of the stishovite phase. From A. E. Gleason *et al.* Nat. Commun. **6**, 8191 (2015). Copyright 2015 Author(s), licensed under a Creative Commons Attribution (CC BY) license.

pressures, there may be some merit in considering non-planar geometries for future studies. While such a suggestion might be considered somewhat speculative, we note that the study of high energy density matter up to 50 TPa in the plasma state has been possible in such a geometry, albeit under shock compression.^{273,274} If such an approach were to be used, one might be able to make some reasonable estimates of the pressure if diffraction pressure standards could be developed in this regime—for example by establishing the pressure-density equations of state of materials known not to change phase to TPa pressures and then extrapolating these to higher pressures still. A measurement of the sample density via x-ray diffraction would then enable the pressure to be estimated, once suitable corrections were made for the different temperatures. In this regard, we note recent work at NIF and on the Z machine that has utilized shockless dynamic compression, combined with velocimetry measurements, to establish 298 K isotherms for copper, gold, and platinum up to TPa pressures with the explicit aim of establishing secondary pressure scale at such pressures.^{275,276}

It is also the case that the vast majority of simulation studies at the atomistic level—that is to say MD simulations—have also almost exclusively concentrated on planar loading, though a small number of studies of other geometries are starting to be made,²⁷⁷ and once more we consider this an area ripe for further exploration.

I. Complementary techniques: RIXS

We have discussed above the role that femtosecond x-ray diffraction can play in identifying the crystal structure of novel materials that can be produced under transient high-pressure compression. As noted above, many of these materials, under such conditions, are thought to have interesting electronic properties—e.g., transforming to electrodes, topological insulators, or superconductors. Furthermore, it is well known that pressure can transform metals to insulators and vice versa.^{278,279} The distribution of the electrons in real space (which is essentially the information gleaned by the elastic x-ray scattering process of diffraction) does not of itself provide information on these electrical properties—for that we will need to be able to probe the actual electronic structure of the material while it is under high pressure. In the past, electrical or optical properties of matter under transient compression have been gleaned from surface reflectivity measurements²¹⁶ but the information gathered by this means is extremely limited.

One potential method of gathering far more information about the electronic structure, which has been proven in principle on the pertinent timescales, is RIXS:²⁸⁰ resonant inelastic x-ray scattering. While x-ray diffraction relies on elastic scattering of the incident photons by the electrons in the system, be they bound or free (and, thus, is effectively Thomson scattering), RIXS is an inelastic scattering technique where the outgoing photon has lower energy than the incident FEL photon. The process is shown schematically in Fig. 18.

We can model the interaction of x rays with the electrons in matter by noting that the vector potential of the electromagnetic field of the x rays gives rise to an interaction Hamiltonian containing the terms

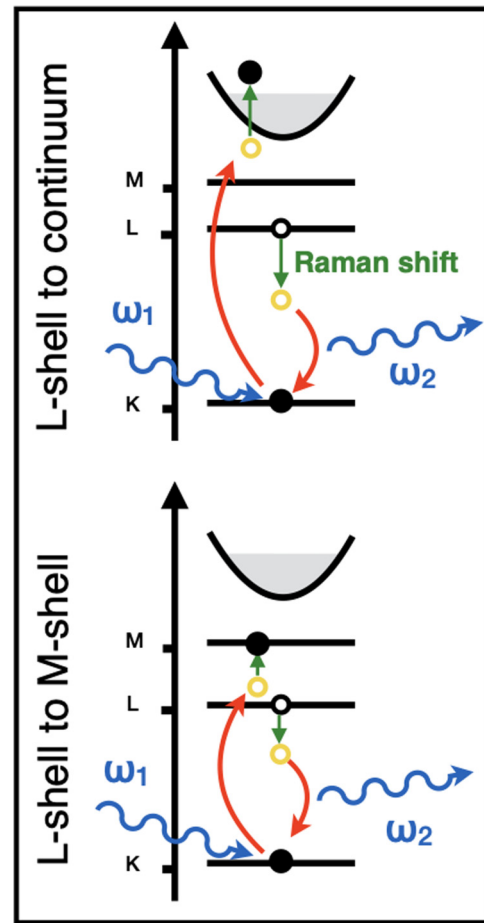


FIG. 18. A schematic diagram of resonant inelastic x-ray scattering (RIXS). Empty states in the continuum (upper plot) or in a bound level (lower plot) can be probed by observing the intensity of outgoing Raman-shifted x-ray photons. The figure is reproduced with permission from the work of O. Humphries *et al.*, *Phys. Rev. Lett.* **125**, 195001 (2020). Copyright 2020 APS.

$$H_I = -\frac{\alpha}{2}(\vec{p} \cdot \vec{A} + \vec{A} \cdot \vec{p}) + \frac{\alpha^2}{2} \vec{A} \cdot \vec{A}, \quad (15)$$

where α is the fine structure constant. When applied as a perturbation in first order, the $\vec{A} \cdot \vec{A}$ term gives rise to Thomson scattering^{281,282} and the $\vec{A} \cdot \vec{p}$ term photon absorption or emission (these being separate processes). RIXS, being a single process that gives rise to a photon-in and a photon-out, is a term that is second order in α (like Thomson scattering), but in contrast arises from the second order perturbation of the $\vec{A} \cdot \vec{p}$ term and, thus, depends on the electronic structure of the material.

As an example, and as can be seen from Fig. 18, if the x rays are tuned below the K-edge of a material to an intermediate state, then an electron can be excited into the valence band, and simultaneously, to conserve energy, a photon is then emitted with an

energy lower than the center of the $K\alpha$ energy. If the lifetime of this process is dominated by the K -shell core-hole lifetime, and considering the process whereby an electron is excited into the valence band, for FEL photons of frequency Ω , photons at lower energies ω are scattered with a cross section that is proportional to a Lorentzian profile dictated by the natural lifetime of the $K\alpha$, and the empty density of states of the valence bands (multiplied by an appropriate dipole matrix element). As such, the empty density of states (DOS) of the valence band can be probed by such scattering in a single few-femtosecond shot over a wide range of energy. Indeed, the first experiments demonstrated that the DOS could be probed over several hundred eV in this way.²⁸⁰ These proof of principle experiments used an FEL pulse with a wide spectral bandwidth (~ 30 eV at a photon energy of ~ 8 keV), dictated by the SASE nature of the beam and, thus, although the spectrometer used had a resolution of order 2 eV,²⁸³ the SASE bandwidth meant that the final resolution would have been insufficient to see features such as the opening or closing of bandgaps. However, similar numbers of FEL photons can now be produced in seeded beams with bandwidths closer to 0.5 eV or below,⁸⁵ and thus exploring such electronic properties in this way does seem feasible, although they will also require spectrometers that themselves have resolutions in this regime.

It is also worth noting that such an increase in spectral resolution could also potentially give access to a measurement of the temperature of the electrons in metallic systems (assuming it is low compared with the Fermi temperature), in that population of bound states in the band will be determined by the temperature-dependent Fermi function. With improvements in the bandwidth of the FEL pulses, RIXS may thus provide a complementary means of measuring temperature within a system compared with those already discussed in Sec. IV C. In certain cases, temperature might also be inferred from the depopulation of bound states via ionization, as depicted in the lower plot in Fig. 18. Indeed, it was this method that was used to determine temperatures in the initial FEL RIXS experiments.²⁸⁰

Care will need to be taken that the x-ray beam itself does not significantly perturb the electron distribution function of the system, which will place an upper limit on the intensity of the FEL pulse on the target of interest. In the preliminary experiment described above, the FEL beam was deliberately focused on a small spot (down to a diameter of $2\mu\text{m}$) in order to heat the system to temperatures in the few eV regime. Given that for many laser compression experiments diameters of more than $100\mu\text{m}$ would be more appropriate, and absorption is by definition low as one remains below an absorption edge, it should be possible to keep the heating effect of the scattering beam such that it does not overly perturb the system.

Ideally, one would wish to employ RIXS at the same time as obtaining structural information via x-ray diffraction. This may not always be possible, or conflicts may arise, because diffraction will require high energy x rays in order to probe a sufficiently large volume of reciprocal space (leading to high spatial resolution), whereas RIXS relies on tuning the x rays to a particular energy based on the atomic number of the element of interest. It may thus not be possible to employ both techniques with a single color FEL pulse, but may require simultaneous probing of the sample with

two different FEL pulses of two different photon energies, if and when such technology becomes available.

V. TECHNICAL DEVELOPMENTS

The evolution of our ability to study materials that have been dynamically compressed to high pressures via femtosecond x-ray diffraction has been reliant on the astonishing development of x-ray FELs and upon the optical drivers required for the compression process. We, thus, conclude our perspectives by noting that future advances within this field will themselves be influenced largely by further advancements in the underpinning FEL and driver technologies.

Our first comment is to note the huge disparity to date in the repetition rate between the x-ray sources and the optical lasers that provide the ablation pressure to compress the sample. When it first came online in operating mode, LCLS could provide x-ray pulses at 120 Hz. In contrast, the several 10 s of Joules nanosecond-pulse-length laser that operated at the Materials in Extreme Conditions (MEC) end-station, allowing dynamic compression, is a two-arm system, where each arm of the laser can only produce a shot once every 3 min. We note that FELs based on superconducting accelerator technologies, such as the European XFEL,¹¹ have even higher x-ray repetition rates, bringing the disparity between the rate at which the optical laser can create samples under compression, and that at which the x-ray FEL probe such samples, into even starker relief. It is in this context recent development in driver technologies should be viewed, whereby the use of diodes to pump the gain media of the drive lasers (as opposed to flashlamps), combined with active cooling of the amplifying media, has led to the development of 100 J class nanosecond optical lasers that have repetition rates of 10 Hz. Specifically, the DiPOLE laser^{129,235} that has recently been sited at the European XFEL has been shown to exceed the parameters described above. Furthermore, it has been developed such that the temporal profile of the laser pulse can be sculpted in time to a user-defined shape in order to allow ramped pressure pulses to be applied to the target in order to keep it closer to an isentrope, as described in Sec. IV A. The system as a whole also incorporates adaptive optics with the aim of optimizing the spatial uniformity of the beam at focus on the target. At the time of writing, this system has yet to be fully commissioned, but we anticipate it being able to vastly increase the number of experiments that can be performed, and the amount of data collected. The capacity to vary the temporal shape of the driving pulse in real time, and thus the rate of loading, should influence the final temperatures reached in the target. In addition, repetition rates of this order will be necessary if techniques that are photon-hungry from the x-ray perspective are also going to be exploited—e.g., the inelastic scattering from phonons discussed in Sec. IV C. The full exploitation of these higher repetition rates will itself be reliant on novel methods of mass-producing the targets to be compressed, as discussed in Sec. II C.

A further advantage of high repetition rate experiments will be the ability to monitor, via VISAR, the size and planarity of the compressed region in these uniaxial experiments. As has been discussed previously, owing to the finite size of the optical spot that produces the ablation pressure at the surface of the target,

refraction from the edges of the compressed region occurs as the compression wave advances into the target, and in order to probe a well-defined region, the x rays must be focused on within a region where such refraction has yet to occur—indeed the ability of the FEL output to be so focused (to μm or tens of μm diameters) is one of the advantages of this approach and means that relatively low optical laser energies can be employed (as the spot size can be minimized) for a given pressure, as has been discussed in Sec. III A. What the final limits will be on the pressures attainable by such modest lasers in both ramp and shock compression experiments has yet to be determined, and clearly a whole range of 2D simulations would be most welcome as a future direction in the field, and we look forward to the commissioning of the DiPOLE system at XFEL where such ideas can be explored empirically.

While drivers with increased repetition rate comprise one obvious direction for the field, we also consider that drivers with increased overall energy will have a significant future impact. The nanosecond lasers that have been placed alongside FELs to date have been in the 10–100 J class. For the experiments that have been conducted thus far—i.e., those in planar geometry—the requirements to have laser spot sizes far greater than the sample thickness, along with a laser pulse length itself determined largely by the target thickness and sound speed—leads to an overall limit on the peak laser intensity that can be achieved on the target to be compressed, and thus a limit on the pressures achievable (see above). While it will be a sample-dependent figure, realistically we would estimate that the peak pressures achievable, at least for shock compression combined with x-ray diffraction, will be of order 0.5 TPa for a 100 J class optical laser, and similar pressures might be achievable with ramp or multiple-shock compression depending upon target design. As shown in Sec. II A, simple ablation physics models show that the applied pressure scales approximately as the intensity to the two-thirds power, i.e., less than linearly, implying that a kJ class system will be required to enable multi-TPa physics to be explored, unless splitting of the beams to enable convergent geometry compressions, as described in Sec. IV H is implemented.

In the context of the suggestion above that increased laser energies (and intensities) will lead to high pressures, an interesting question that has yet to be addressed in any great detail is what the ultimate limitations might be of this approach. The laser-ablation technique by its very nature produces a high temperature plasma at the target surface, and the temperatures reached can easily attain a few hundred eV to a keV for intensities associated with multi-TPa pressures (note 1 eV is about 11 000 K). This plasma, thus, acts as a source of copious x rays that can preheat the underlying material, which would render unusable the whole approach. Furthermore, it is well known from studies of relevance to ICF that laser-plasma instabilities can lead to the production of electrons with energies far greater than those in the mean thermal background, and these “hot electrons” can also be a source of preheat.²⁸⁴ It is for these reasons that in experiments on the NIF discussed in Sec. I B the targets have often incorporated a thin layer of gold between the ablation surface and the material of interest, to act as an x-ray absorber, and we consider such shielding will be required in most targets as higher pressures are sought, and knowledge gleaned from the ICF community, where the DT fuel needs to be kept cool during laser ablation, will prove extremely useful in future target designs.

In addition to the advances in drive laser technology discussed above, advancements in the performance and operational modes of the FELs themselves will no doubt advance the field, and we have already commented on the impact of several of these in previous parts of this paper. Moving from SASE operation to self-seeded operation can reduce the bandwidth of the FEL from about several 10 s of eV with irreproducible multimode structure to several eV FWHM and a nearly Fourier-transform limited bandwidth.^{85,86,285} This advance will allow much improved high resolution spectroscopy (HRIXS) and higher-resolution diffraction. In Sec. IV C, we emphasized that extremely high spectral resolution is required to discern inelastic scattering from phonons and, thus, increases in FEL spectral brightness by seeding methods—providing similar numbers of phonons in a greatly reduced spectral bandwidth—will be extremely beneficial.^{85,86} Such advances provide similar benefits for the RIXS measurements discussed in Sec. IV I.

In Sec. IV E, we noted that the operation of FELs at higher photon energies will significantly improve our understanding of high pressure liquids by enabling higher- Q data to be collected above the current limiting value of $10\text{--}12\text{ \AA}^{-1}$. A lower Q limit of 15 \AA^{-1} would be both achievable and provide useful structural data. With 20 keV x rays, this requires data to $2\theta \sim 95^\circ$ while with 25 keV x rays it would require data to $2\theta \sim 73^\circ$. It should be noted that the next generation of diffraction limited synchrotrons, such as ESRF-EBS, APS-U, and PETRA-IV, will produce extremely intense ($10^8\text{--}10^9$ ph/pulse), essentially monochromatic ($\Delta E/E \sim 5 \times 10^{-3}$) x-ray pulses at energies up to 60 keV. While the peak brightness from such storage rings will still be below that obtainable at a FEL, the difference is reduced at 60 keV.

Finally, the new ability at LCLS and elsewhere to operate in a double or multi-bunch mode where x-ray pulses are separated by intervals on the 10 s or 100 s of ps timescales,^{286,287} and the future optimization of area detectors capable of single-bunch isolation,²⁸⁸ will revolutionize the study of time-resolved phase transformation and many other pump-probe type experiments including isochoric heating with subsequent compression and probing by the following pulses.

VI. SUMMARY

In summary, our ability to study the structure and deformation pathways of laser-shock-compressed matter, and, via ramp compression, solids created via laser-ablation at pressures exceeding those that can be achieved by any diamond anvil cell has advanced enormously over the past few years. These advances have been made possible by the attendant developments in technology, in that exquisitely temporally tailored laser pulses allow us to compress materials on the timescales of several nanoseconds, before the wave has steepened into a shock. Structural diagnosis of materials on ultra-fast timescales has been revolutionized by the development of x-ray FELs. These two areas are starting to converge with the siting of new high repetition-rate optical drive lasers alongside FEL facilities.

While much has been learned over the past decade since the LCLS produced its first x rays, in many ways the field is still in its infancy, and many questions still remain. Within this article, we have attempted to outline our perspectives on those issues we deem

to be the most pertinent. From the early FEL experiments that have been performed much is starting to be understood, at least for a few materials, on what the underlying deformation processes are at the lattice level that lead to the relief of high shear stresses induced by the uniaxial compression process. That said, our overall understanding of plastic deformation as a function of both strain rate and strain is clearly far from complete. As it is the amount of plastic work to which the sample is subject that dominates the temperature rise in the target, these gaps in our knowledge clearly need to be addressed. However, not only are there uncertainties in how much heating may be taking place in these types of experiments, but reliable wide-ranging and accurate measurements of temperature of dynamically compressed samples are lacking.

In addition to our inability to know accurately the temperature, it is also clear that rapid compression, albeit by shock or by ramp, leads to the observation that phase boundaries for polymorphic transitions often do not match those seen in static cases, and indeed certain phases may appear absent, or new unexpected ones may emerge. The degree to which these observations can be accounted for by residual shear stresses (or the non-hydrostatic pathway taken to a largely hydrostatic state) or kinetic effects, or both, is a question that has not, in our view, received as much attention as it might eventually merit. However, if we wish to apply findings about the structure of dynamically created high-pressure matter to environments where high pressures exist on longer time-scales, for example, within the interior of planets, then a more nuanced understanding of the states reached on these short time-scales is surely in order.

Finally, we note that the increased understanding of the response of matter at the lattice level to rapidly applied pressure that has been gleaned over the last decade or so has been largely driven by the spectacular improvements and developments in both optical lasers and x-ray FELs, along with concomitant improvements in simulation and diagnostic techniques: the furtherance of this burgeoning field will no doubt be shaped by the future evolution of these underpinning technologies.

ACKNOWLEDGMENTS

J.S.W. is grateful to Dr. Patrick Heighway of the University of Oxford for useful discussions about the details of plasticity at ultrahigh strain rates and for support from AWE through the Oxford Centre for High Energy Density Science (OxCHEDS). He is further grateful to EPSRC for support under Grant No. EP/S025065/1. M.I.M. would like to thank Professor David Keen of Rutherford Appleton Laboratory and Professor Graeme Ackland of the University of Edinburgh for useful discussions about structural studies of liquids and DFT calculations, respectively. He is further grateful to EPSRC for support under Grant Nos. EP/J017256/1 and EP/S022155/1. J.H.E. would like to thank Dr. Peter Celliers for useful discussions about VISAR analysis and to acknowledge that his work was performed under the auspices of the U.S. Department of Energy by Lawrence Livermore National Laboratory under Contract No. DE-AC52-07NA27344 and was supported by the LLNL-LDRD Program under Project No. 21-ERD-032.

AUTHOR DECLARATIONS

Conflict of Interest

The authors have no conflicts to disclose.

Author Contributions

Justin S. Wark: Conceptualization (equal); Writing – original draft (equal); Writing – review & editing (equal). **Malcolm I. McMahon:** Conceptualization (equal); Writing – original draft (equal); Writing – review & editing (equal). **Jon H. Eggert:** Conceptualization (equal); Writing – original draft (equal); Writing – review & editing (equal).

DATA AVAILABILITY

Data sharing is not applicable to this article as no new data were created or analyzed in this study.

REFERENCES

- ¹T. S. Duffy and R. F. Smith, “Ultra-high pressure dynamic compression of geological materials,” *Front. Earth Sci.* **7**, 23 (2019).
- ²R. F. Smith, J. H. Eggert, R. Jeanloz, T. S. Duffy, D. G. Braun, J. R. Patterson, R. E. Rudd, J. Biener, A. E. Lazicki, A. V. Hamza, J. Wang, T. Braun, L. X. Benedict, P. M. Celliers, and G. W. Collins, “Ramp compression of diamond to five terapascals,” *Nature* **511**, 330–333 (2014).
- ³A. Lazicki, D. McGonigle, J. R. Rygg, D. G. Braun, D. C. Swift, M. G. Gorman, R. F. Smith, P. G. Heighway, A. Higginbotham, M. J. Sugitt, D. E. Fratanduono, F. Coppari, C. E. Wehrenberg, R. G. Kraus, D. Erskine, J. V. Bernier, J. M. McNaney, R. E. Rudd, G. W. Collins, J. H. Eggert, and J. S. Wark, “Metastability of diamond ramp-compressed to 2 terapascals,” *Nature* **589**, 532–535 (2021).
- ⁴R. Helled, J. D. Anderson, M. Podolak, and G. Schubert, “Interior models of Uranus and Neptune,” *Astrophys. J.* **726**, 15 (2010).
- ⁵W. Hubbard, J. MacFarlane, J. Anderson, G. Null, and E. Biller, “Interior structure of Saturn inferred from Pioneer 11 gravity data,” *J. Geophys. Res.: Space Phys.* **85**, 5909–5916, <https://doi.org/10.1029/JA085iA11p05909> (1980).
- ⁶P. Emma, R. Akre, J. Arthur, R. Bionta, C. Bostedt, J. Bozek, A. Brachmann, P. Bucksbaum, R. Coffee, F.-J. Decker, Y. Ding, D. Dowell, S. Edstrom, A. Fisher, J. Frisch, S. Gilevich, J. Hastings, G. Hays, P. Hering, Z. Huang, R. Iverson, H. Loos, M. Messerschmidt, A. Miahnahri, S. Moeller, H.-D. Nuhn, G. Pile, D. Ratner, J. Rzepiela, D. Schultz, T. Smith, P. Stefan, H. Tompkins, J. Turner, J. Welch, W. White, J. Wu, G. Yocky, and J. Galayda, “First lasing and operation of an ångström-wavelength free-electron laser,” *Nat. Photonics* **4**, 641–647 (2010).
- ⁷T. Ishikawa, H. Aoyagi, T. Asaka, Y. Asano, N. Azumi, T. Bizen, H. Ego, K. Fukami, T. Fukui, Y. Furukawa, S. Goto, H. Hanaki, T. Hara, T. Hasegawa, T. Hatsui, A. Higashiya, T. Hirono, N. Hosoda, M. Ishii, T. Inagaki, Y. Inubushi, T. Itoga, Y. Joti, M. Kago, T. Kameshima, H. Kimura, Y. Kirihaara, A. Kiyomichi, T. Kobayashi, C. Kondo, T. Kudo, H. Maesaka, X. M. Maréchal, T. Masuda, S. Matsubara, T. Matsumoto, T. Matsushita, S. Matsui, M. Nagasono, N. Nariyama, H. Ohashi, T. Ohata, T. Ohshima, S. Ono, Y. Otake, C. Saji, T. Sakurai, T. Sato, K. Sawada, T. Seike, K. Shirasawa, T. Sugimoto, S. Suzuki, S. Takahashi, H. Takebe, K. Takeshita, K. Tamasaku, H. Tanaka, R. Tanaka, T. Tanaka, T. Togashi, K. Togawa, A. Tokuhisa, H. Tomizawa, K. Tono, S. Wu, M. Yabashi, M. Yamaga, A. Yamashita, K. Yanagida, C. Zhang, T. Shintake, H. Kitamura, and N. Kumagai, “A compact x-ray free-electron laser emitting in the sub-ångström region,” *Nat. Photonics* **6**, 540–544 (2012).
- ⁸E. Allaria, R. Appio, L. Badano, W. A. Barletta, S. Bassanese, S. G. Biedron, A. Borgia, E. Busetto, D. Castronovo, P. Cinquegrana, S. Cleva, D. Cocco, M. Cornacchia, P. Craievich, I. Cudin, G. D’Auria, M. Dal Forno,

- M. B. Danailov, R. De Monte, G. De Ninno, P. Delgiusto, A. Demidovich, S. Di Mitri, B. Diviacco, A. Fabris, R. Fabris, W. Fawley, M. Ferianis, E. Ferrari, S. Ferry, L. Froehlich, P. Furlan, G. Gaio, F. Gelmetti, L. Giannessi, M. Giannini, R. Gobessi, R. Ivanov, E. Karantzoulis, M. Lonza, A. Lutman, B. Mahieu, M. Milloch, S. V. Milton, M. Musardo, I. Nikolov, S. Noe, F. Parmigiani, G. Penco, M. Petronio, L. Pivet, M. Predonzani, F. Rossi, L. Rumiz, A. Salom, C. Scafuri, C. Serpico, P. Sigalotti, S. Spampinati, C. Spezzani, M. Svandrlik, C. Svetina, S. Tazzari, M. Trovo, R. Umer, A. Vascotto, M. Veronese, R. Visintini, M. Zaccaria, D. Zangrando, and M. Zangrando, "Highly coherent and stable pulses from the Fermi seeded free-electron laser in the extreme ultraviolet," *Nat. Photonics* **6**, 699–704 (2012).
- ⁹J. Park, I. Eom, T.-H. Kang, S. Rah, K. H. Nam, J. Park, S. Kim, S. Kwon, S. H. Park, K. S. Kim, H. Hyun, S. N. Kim, E. H. Lee, H. Shin, S. Kim, M. jin Kim, H.-J. Shin, D. Ahn, J. Lim, C.-J. Yu, C. Song, H. Kim, D. Y. Noh, H. S. Kang, B. Kim, K.-W. Kim, I. S. Ko, M.-H. Cho, and S. Kim, "Design of a hard x-ray beamline and end-station for pump and probe experiments at Pohang Accelerator Laboratory X-ray Free Electron Laser Facility," *Nucl. Instrum. Methods Phys. Res., Sect. A* **810**, 74–79 (2016).
- ¹⁰C. J. Milne, T. Schietinger, M. Aiba, A. Alarcon, J. Alex, A. Anghel, V. Arsov, C. Beard, P. Beaud, S. Bettoni, M. Bopp, H. Brands, M. Brönnimann, I. Brunnenkant, M. Calvi, A. Citterio, P. Craievich, M. Csati Divall, M. Dällenbach, M. D'Amico, A. Dax, Y. Deng, A. Dietrich, R. Dinapoli, E. Divall, S. Dordevic, S. Ebner, C. Erny, H. Fitze, U. Flechsig, R. Follath, F. Frei, F. Gärtner, R. Ganter, T. Garvey, Z. Geng, I. Gorgisyan, C. Gough, A. Haufl, C. P. Hauri, N. Hiller, T. Humar, S. Hunziker, G. Ingold, R. Ischebeck, M. Janousch, P. Juranic, M. Jurcic, M. Kaiser, B. Kalantari, R. Kalt, B. Keil, C. Kittel, G. Knopp, W. Koprek, H. T. Lemke, T. Lippuner, D. Llorente Sancho, F. Löh, C. Lopez-Cuenca, F. Märki, F. Marcellini, G. Marinkovic, I. Martiel, R. Menzel, A. Mozzanica, K. Nass, G. L. Orlandi, C. Ozkan Loch, E. Panepucci, M. Paraliyev, B. Patterson, B. Pedrini, M. Pedrozzi, P. Pollet, C. Pradervand, E. Prat, P. Radi, J.-Y. Ragun, S. Redford, J. Rehanek, J. Réhault, S. Reiche, M. Ringe, J. Rittmann, L. Rivkin, A. Romann, M. Ruat, C. Ruder, L. Sala, L. Schebächer, T. Schilcher, V. Schlott, T. Schmidt, B. Schmitt, X. Shi, M. Stadler, L. Stingelin, W. Sturzenegger, J. Szlachetko, D. Thattil, D. M. Treyer, A. Trisorio, W. Tron, S. Vetter, C. Vicario, D. Voulot, M. Wang, T. Zamoj, C. Zellweger, R. Zennaro, E. Zimoch, R. Abela, L. Patthey, and H.-H. Braun, "SwissFEL: The Swiss x-ray free electron laser," *Appl. Sci.* **7**, 720 (2017).
- ¹¹W. Decking, S. Abeghyan, P. Abramian, A. Abramsky, A. Aguirre, C. Albrecht, P. Alou, M. Altarelli, P. Altmann, K. Amyan, V. Anashin, E. Apostolov, K. Appel, D. Auguste, V. Ayvazyan, S. Baark, F. Babies, N. Baboi, P. Bak, V. Balandin, R. Baldinger, B. Baranasic, S. Barbanotti, O. Belikov, V. Belokurov, L. Belova, V. Belyakov, S. Berry, M. Bertucci, B. Beutner, A. Block, M. Blöcher, T. Böckmann, C. Bohm, M. Böhner, V. Bondar, E. Bondarchuk, M. Bonezzi, P. Borowiec, C. Bösch, U. Bösenberg, A. Bosotti, R. Böspflug, M. Bousonville, E. Boyd, Y. Bozhko, A. Brand, J. Branlard, S. Briechle, F. Brinker, S. Brinker, R. Brinkmann, S. Brockhauser, O. Brovko, H. Brück, A. Brüdgam, L. Butkowski, T. Büttner, J. Calero, E. Castro-Carballo, G. Cattalanotto, J. Charrier, J. Chen, A. Cherepenko, V. Cheskidov, M. Chiodini, A. Chong, S. Choroba, M. Chorowski, D. Churanov, W. Cichalewski, M. Clausen, W. Clement, C. Cloué, J. A. Cobos, N. Coppola, S. Cunis, K. Czuba, M. Czwalianna, B. D'Almagne, J. Dammann, H. Danared, A. de Zubiurre Wagner, A. Delfs, T. Delfs, F. Dietrich, T. Dietrich, M. Dohlus, M. Dommach, A. Donat, X. Dong, N. Doynikov, M. Dressel, M. Duda, P. Duda, H. Eckoldt, W. Ehsan, J. Eidam, F. Eints, C. Engling, U. Englisch, A. Ermakov, K. Escherich, J. Eschke, E. Saldin, M. Faesing, A. Fallou, M. Felber, M. Fenner, B. Fernandes, J. M. Fernández, S. Feuker, K. Filippakopoulos, K. Floettmann, V. Fogel, M. Fontaine, A. Francés, I. F. Martin, W. Freund, T. Freyermuth, M. Friedland, L. Fröhlich, M. Fuseti, J. Fydrich, A. Gallas, O. García, L. Garcia-Tabares, G. Geloni, N. Gerasimova, C. Gerth, P. Geffler, V. Gharibyan, M. Gloor, J. Glowinkowski, A. Goessel, Z. Gołębiewski, N. Golubeva, W. Grabowski, W. Graeff, A. Grebentsov, M. Grecki, T. Grevsmühl, M. Gross, U. Grosse-Wortmann, J. Grünert, S. Grunewald, P. Grzegory, G. Feng, H. Guler, G. Gusev, J. L. Gutierrez, L. Hagge, M. Hamberg, R. Hanneken, E. Harms, I. Hartl, A. Hauberg, S. Hauf, J. Hauschildt, J. Hauser, J. Havlicek, A. Hedqvist, N. Heidbrook, F. Hellberg, D. Henning, O. Hensler, T. Hermann, A. Hidvégi, M. Hierholzer, H. Hintz, F. Hoffmann, M. Hoffmann, M. Hoffmann, Y. Holler, M. Hüning, A. Ignatenko, M. Ilchen, A. Iluk, J. Iversen, M. Izquierdo, L. Jachmann, N. Jardon, U. Jastrow, K. Jensch, J. Jensen, M. Ježabek, M. Jidda, H. Jin, N. Johansson, R. Jonas, W. Kaabi, D. Kaefer, R. Kammering, H. Kapitza, S. Karabekyan, S. Karstensen, K. Kasprzak, V. Katalev, D. Keese, B. Keil, M. Kholopov, M. Killenberger, B. Kitaev, Y. Klimchenko, R. Klos, L. Knebel, A. Koch, M. Koepke, S. Köhler, W. Köhler, N. Kohlstrunk, Z. Konopkova, A. Konstantinov, W. Kook, W. Koprek, M. Körfer, O. Korth, A. Kosarev, K. Kosiński, D. Kostin, Y. Kot, A. Kotarba, T. Kozak, V. Kozak, R. Kramert, M. Krasilnikov, A. Krasnov, B. Krause, L. Kravchuk, O. Krebs, R. Kretschmer, J. Kreutzkamp, O. Kröplin, K. Krzysik, G. Kube, H. Kuehn, N. Kujala, V. Kulikov, V. Kuzminych, D. La Civita, M. Lacroix, T. Lamb, A. Lancetov, M. Larsson, D. Le Pivdic, S. Lederer, T. Lensch, D. Lenz, A. Leuschner, F. Levenhagen, Y. Li, J. Liebing, L. Lilje, T. Limberg, D. Lipka, B. List, J. Liu, S. Liu, B. Lorbeer, J. Lorkiewicz, H. H. Lu, F. Ludwig, K. Machau, W. Maciocha, C. Madec, C. Magueur, C. Maiano, I. Maksimova, K. Malcher, T. Maltezopoulos, E. Mamoshkina, B. Manschwetus, F. Marcellini, G. Marinkovic, T. Martinez, H. Martirosyan, W. Maschmann, M. Maslov, A. Matheisen, U. Mavric, J. Meißner, K. Meissner, M. Messerschmidt, N. Meyners, G. Michalski, P. Michelato, N. Mildner, M. Moe, F. Moglia, C. Mohr, S. Mohr, W. Möller, M. Mommerz, L. Monaco, C. Montiel, M. Moretti, I. Morozov, P. Morozov, and D. Mross, "A MHz-repetition-rate hard x-ray free-electron laser driven by a superconducting linear accelerator," *Nat. Photonics* **14**, 391–397 (2020).
- ¹²Z. Zhao, D. Wang, Q. Gu, L. Yin, M. Gu, Y. Leng, and B. Liu, "Status of the SFXEL facility," *Appl. Sci.* **7**, 607 (2017).
- ¹³E. A. Seddon, J. A. Clarke, D. J. Dunning, C. Masciovecchio, C. J. Milne, F. Parmigiani, D. Rugg, J. C. H. Spence, N. R. Thompson, K. Ueda, S. M. Vinko, J. S. Wark, and W. Wurth, "Short-wavelength free-electron laser sources and science: A review," *Rep. Prog. Phys.* **80**, 115901 (2017).
- ¹⁴S. M. Vinko, O. Ciricosta, B. I. Cho, K. Engelhorn, H.-K. Chung, C. R. D. Brown, T. Burian, J. Chalupsky, R. W. Falcone, C. Graves, V. Hájková, A. Higginbotham, L. Juha, J. Krzywinski, H. J. Lee, M. Messerschmidt, C. D. Murphy, Y. Ping, A. Scherz, W. Schlotter, S. Toleikis, J. J. Turner, L. Vysin, T. Wang, B. Wu, U. Zastrau, D. Zhu, R. W. Lee, P. A. Heimann, B. Nagler, and J. S. Wark, "Creation and diagnosis of a solid-density plasma with an x-ray free-electron laser," *Nature* **482**, 59–62 (2012).
- ¹⁵P. W. Bridgman, *Collected Experimental Papers by P.W. Bridgman* (Harvard University Press, 1964).
- ¹⁶P. W. Bridgman, *The Physics of High Pressure* (Bell, London, 1931).
- ¹⁷P. F. McMillan, "Pressing on: The legacy of Percy W. Bridgman," *Nat. Mater.* **4**, 715–718 (2005).
- ¹⁸R. A. Forman, G. J. Piermarini, J. D. Barnett, and S. Block, "Pressure measurement made by the utilization of ruby sharp-line luminescence," *Science* **176**, 284–285 (1972).
- ¹⁹A. Jayaraman, "Diamond anvil cell and high-pressure physical investigations," *Rev. Mod. Phys.* **55**, 65–108 (1983).
- ²⁰G. J. Piermarini, "High pressure x-ray crystallography with the diamond cell at NIST/NBS," *J. Res. Natl. Inst. Stand. Technol.* **106**, 889–920 (2001).
- ²¹M. I. Eremets, A. P. Drozdov, P. P. Kong, and H. Wang, "Semimetallic molecular hydrogen at pressure above 350 GPa," *Nat. Phys.* **15**, 1246–1249 (2019).
- ²²A. Dewaele, P. Loubeyre, F. Occelli, O. Marie, and M. Mezouar, "Toroidal diamond anvil cell for detailed measurements under extreme static pressures," *Nat. Commun.* **9**, 2913 (2018).
- ²³Z. Jenei, E. F. O'Bannon, S. T. Weir, H.-C. Cynn, M. J. Lipp, and W. J. Evans, "Single crystal toroidal diamond anvils for high pressure experiments beyond 5 mbar," *Nat. Commun.* **9**, 3563 (2018).
- ²⁴L. Dubrovinsky, N. Dubrovinskaia, V. B. Prakapenka, and A. M. Abakumov, "Implementation of micro-ball nanodiamond anvils for high-pressure studies above 6 mbar," *Nat. Commun.* **3**, 1163 (2012).
- ²⁵T. Sakai, T. Yagi, T. Irifune, H. Kadobayashi, N. Hirao, T. Kunimoto, H. Ohfuchi, S. Kawaguchi-Imada, Y. Ohishi, S. Tateno, and K. Hirose, "High

pressure generation using double-stage diamond anvil technique: Problems and equations of state of rhenium," *High Pressure Res.* **38**, 107–119 (2018).

²⁶N. Dubrovinskaia, L. Dubrovinsky, N. A. Solopova, A. Abakumov, S. Turner, M. Hanfland, E. Bykova, M. Bykov, C. Prescher, V. B. Prakapenka, S. Petitgirard, I. Chuvashova, B. Gasharova, Y.-L. Mathis, P. Ershov, I. Snigireva, and A. Snigirev, "Terapascal static pressure generation with ultrahigh yield strength nanodiamond," *Sci. Adv.* **2**, e1600341 (2016).

²⁷E. Velikhov, *History of the Soviet Atomic Project* (Atomic Science and Technology Publishing House, Moscow, 1997).

²⁸L. Al'tshuler, "Development of dynamical methods of investigation of high pressures in Russia," in *High-Pressure Shock Compression of Solids VII* (Springer, 2004), pp. 1–37.

²⁹S. Minshall, "Properties of elastic and plastic waves determined by pin contactors and crystals," *J. Appl. Phys.* **26**, 463–469 (1955).

³⁰D. Bancroft, E. L. Peterson, and S. Minshall, "Polymorphism of iron at high pressure," *J. Appl. Phys.* **27**, 291–298 (1956).

³¹J. M. Walsh and R. H. Christian, "Equation of state of metals from shock wave measurements," *Phys. Rev.* **97**, 1544–1556 (1955).

³²L. Al'tshuler, K. Krupnikov, B. Ledenev, V. Zhuchikhin, and M. Brazhnik, "Dynamic compressibility and equation of state of iron under high pressure," *Sov. Phys. JETP* **34**, 874–885 (1958).

³³M. Rice, R. McQueen, and J. Walsh, "Compression of solids by strong shock waves," in *Advances in Research and Applications*, Solid State Physics Vol. 6, edited by F. Seitz and D. Turnbull (Academic Press, 1958), pp. 1–63.

³⁴Y. B. Zel'dovich and Y. P. Raizer, *Physics of Shock Waves and High-Temperature Hydrodynamic Phenomena* (Courier Corporation, 2002).

³⁵W. J. M. Rankine, "XV. On the thermodynamic theory of waves of finite longitudinal disturbance," *Philos. Trans. R. Soc. London* **160**, 277–288 (1870).

³⁶P. H. Hugoniot, "Memoire sur la propagation du mouvement dans les corps et plus spécialement dans les gaz parfaits, 1^e partie," *J. Ecol. Polytech.* **57**, 3–97 (1887).

³⁷G. I. Kerley, "The linear up-up relation in shock-wave physics," [arXiv:1306.6916](https://arxiv.org/abs/1306.6916) [cond-mat.mtrl-sci] (2013).

³⁸W. J. Nellis, *Encyclopedia Appl. Phys.* **18**, 541 (1997).

³⁹P. W. Bridgman, "High pressure polymorphism of iron," *J. Appl. Phys.* **27**, 659 (1956).

⁴⁰A. S. Balchan and H. G. Drickamer, "High pressure electrical resistance cell, and calibration points above 100 kilobar," *Rev. Sci. Instrum.* **32**, 308–313 (1961).

⁴¹R. B. Jacobs, "X-ray diffraction of substances under high pressures," *Phys. Rev.* **54**, 325–331 (1938).

⁴²J. C. Jamieson and A. W. Lawson, "X-ray diffraction studies in the 100 kilobar pressure range," *J. Appl. Phys.* **33**, 776–780 (1962).

⁴³Q. Johnson, R. N. Keeler, and J. W. Lyle, "X-ray diffraction experiments in nanosecond time intervals," *Nature* **213**, 1114–1115 (1967).

⁴⁴Q. Johnson, A. Mitchell, R. N. Keeler, and L. Evans, "X-ray diffraction during shock-wave compression," *Phys. Rev. Lett.* **25**, 1099–1101 (1970).

⁴⁵Q. Johnson and A. C. Mitchell, "First X-ray diffraction evidence for a phase transition during shock-wave compression," *Phys. Rev. Lett.* **29**, 1369–1371 (1972).

⁴⁶G. A. Akar'yan and E. M. Moroz, "Pressure on evaporation of matter in a radiation beam," *Sov. J. Exp. and Theor. Phys.* **16**, 1638 (1963).

⁴⁷R. J. Trainor, J. W. Shaner, J. M. Auerbach, and N. C. Holmes, "Ultrahigh-pressure laser-driven shock-wave experiments in aluminum," *Phys. Rev. Lett.* **42**, 1154–1157 (1979).

⁴⁸J. S. Wark, R. R. Whitlock, A. Hauer, J. E. Swain, and P. J. Solone, "Shock launching in silicon studied with use of pulsed x-ray diffraction," *Phys. Rev. B* **35**, 9391–9394 (1987).

⁴⁹J. S. Wark, R. R. Whitlock, A. A. Hauer, J. E. Swain, and P. J. Solone, "Subnanosecond x-ray diffraction from laser-shocked crystals," *Phys. Rev. B* **40**, 5705–5714 (1989).

⁵⁰J. Hawreliak, H. E. Lorenzana, B. A. Remington, S. Lukezic, and J. S. Wark, "Nanosecond x-ray diffraction from polycrystalline and amorphous materials in

a pinhole camera geometry suitable for laser shock compression experiments," *Rev. Sci. Instrum.* **78**, 083908 (2007).

⁵¹J. R. Rygg, J. H. Eggert, A. E. Lazicki, F. Coppari, J. A. Hawreliak, D. G. Hicks, R. F. Smith, C. M. Sorce, T. M. Uphaus, B. Yaakobi, and G. W. Collins, "Powder diffraction from solids in the terapascal regime," *Rev. Sci. Instrum.* **83**, 113904 (2012).

⁵²F. Coppari, R. F. Smith, D. B. Thorn, J. R. Rygg, D. A. Liedahl, R. G. Kraus, A. Lazicki, M. Millot, and J. H. Eggert, "Optimized x-ray sources for x-ray diffraction measurements at the omega laser facility," *Rev. Sci. Instrum.* **90**, 125113 (2019).

⁵³J. R. Rygg, R. F. Smith, A. E. Lazicki, D. G. Braun, D. E. Fratanduono, R. G. Kraus, J. M. McNaney, D. C. Swift, C. E. Wehrenberg, F. Coppari, M. F. Ahmed, M. A. Barrios, K. J. M. Blobaum, G. W. Collins, A. L. Cook, P. Di Nicola, E. G. Dzenitis, S. Gonzales, B. F. Heidl, M. Hohenberger, A. House, N. Izumi, D. H. Kalantar, S. F. Khan, T. R. Kohut, C. Kumar, N. D. Masters, D. N. Polsin, S. P. Regan, C. A. Smith, R. M. Vignes, M. A. Wall, J. Ward, J. S. Wark, T. L. Zobrist, A. Arsenlis, and J. H. Eggert, "X-ray diffraction at the National Ignition Facility," *Rev. Sci. Instrum.* **91**, 043902 (2020).

⁵⁴O. Hurricane and M. Herrmann, "High-energy-density physics at the National Ignition Facility," *Annu. Rev. Nucl. Part. Sci.* **67**, 213–230 (2017).

⁵⁵T. Boehly, D. Brown, R. Craxton, R. Keck, J. Knauer, J. Kelly, T. Kessler, S. Kumpan, S. Loucks, S. Letzring, F. Marshall, R. McCrory, S. Morse, W. Seka, J. Soures, and C. Verdon, "Initial performance results of the omega laser system," *Opt. Commun.* **133**, 495–506 (1997).

⁵⁶V. Malka, F. Amiranoff, C. Chénais-Popovics, J.-C. Gauthier, C. Labaune, E. Dalimier, C. Sauteret, and A. Migus, "Status and overview of research programs at LULI 2000," *Proc. SPIE* **4424**, 70–77 (2001).

⁵⁷A. Denoeud, J.-A. Hernandez, T. Vinci, A. Benuzzi-Mounaix, S. Brygoo, A. Berlioux, F. Lefevre, A. Sollier, L. Videau, A. Ravasio, M. Guarguaglini, L. Duthoit, D. Loison, and E. Brambrink, "X-ray powder diffraction in reflection geometry on multi-beam kj-type laser facilities," *Rev. Sci. Instrum.* **92**, 013902 (2021).

⁵⁸C. Yamanaka, Y. Kato, Y. Izawa, K. Yoshida, T. Yamanaka, T. Sasaki, M. Nakatsuka, T. Mochizuki, J. Kuroda, and S. Nakai, "Nd-doped phosphate glass laser systems for laser-fusion research," *IEEE J. Quantum Electron.* **17**, 1639–1649 (1981).

⁵⁹K. Mima, Y. Kato, H. Azechi, K. Shigemori, H. Takabe, N. Miyanaga, T. Kanabe, T. Norimatsu, H. Nishimura, H. Shiraga, M. Nakai, R. Kodama, K. A. Tanaka, M. Takagi, M. Natatsuka, K. Nishihara, T. Yamanaka, and S. Nakai, "Recent progress of implosion experiments with uniformity improved GEKKO XII laser facility at the Institute of Laser Engineering, Osaka University," *Phys. Plasmas* **3**, 2077–2083 (1996).

⁶⁰P. J. Wisoff, M. W. Bowers, G. V. Erbert, D. F. Browning, and D. R. Jedlovec, "NIF injection laser system," *Proc. SPIE* **5341**, 146–155 (2004).

⁶¹E. Feigenbaum, R. A. Sacks, and M. J. Shaw, "Enhancing the pulse shaping precision of energetic high aspect ratio infrared pulses in the national ignition facility laser system," in *CLEO: 2013, OSA Technical Digest* (online) (Optica Publishing Group, 2013), pp. 1–2.

⁶²H. F. Robey, B. J. MacGowan, O. L. Landen, K. N. LaFortune, C. Widmayer, P. M. Celliers, J. D. Moody, J. S. Ross, J. Ralph, S. LePape, L. F. Berzak Hopkins, B. K. Spears, S. W. Haan, D. Clark, J. D. Lindl, and M. J. Edwards, "The effect of laser pulse shape variations on the adiabat of NIF capsule implosions," *Phys. Plasmas* **20**, 052707 (2013).

⁶³F. Coppari, R. F. Smith, J. H. Eggert, J. Wang, J. R. Rygg, A. Lazicki, J. A. Hawreliak, G. W. Collins, and T. S. Duffy, "Experimental evidence for a phase transition in magnesium oxide at exoplanet pressures," *Nat. Geosci.* **6**, 926–929 (2013).

⁶⁴J. Wang, F. Coppari, R. F. Smith, J. H. Eggert, A. E. Lazicki, D. E. Fratanduono, J. R. Rygg, T. R. Boehly, G. W. Collins, and T. S. Duffy, "X-ray diffraction of molybdenum under shock compression to 450 GPa," *Phys. Rev. B* **92**, 174114 (2015).

⁶⁵A. Lazicki, J. R. Rygg, F. Coppari, R. Smith, D. Fratanduono, R. G. Kraus, G. W. Collins, R. Briggs, D. G. Braun, D. C. Swift, and J. H. Eggert, "X-ray diffraction of solid tin to 1.2 TPa," *Phys. Rev. Lett.* **115**, 075502 (2015).

- ⁶⁶J. Wang, F. Coppari, R. F. Smith, J. H. Eggert, A. E. Lazicki, D. E. Fratanduono, J. R. Rygg, T. R. Boehly, G. W. Collins, and T. S. Duffy, "X-ray diffraction of molybdenum under ramp compression to 1 TPa," *Phys. Rev. B* **94**, 104102 (2016).
- ⁶⁷A. Denoeud, N. Ozaki, A. Benuzzi-Mounaix, H. Uranishi, Y. Kondo, R. Kodama, E. Brambrink, A. Ravasio, M. Bocoum, J.-M. Boudenne, M. Harmand, F. Guyot, S. Mazevet, D. Riley, M. Makita, T. Sano, Y. Sakawa, Y. Inubushi, G. Gregori, M. Koenig, and G. Morard, "Dynamic x-ray diffraction observation of shocked solid iron up to 170 GPa," *Proc. Natl. Acad. Sci.* **113**, 7745–7749 (2016).
- ⁶⁸D. N. Polsin, D. E. Fratanduono, J. R. Rygg, A. Lazicki, R. F. Smith, J. H. Eggert, M. C. Gregor, B. J. Henderson, X. Gong, J. A. Delettrez, R. G. Kraus, P. M. Celliers, F. Coppari, D. C. Swift, C. A. McCoy, C. T. Seagle, J.-P. Davis, S. J. Burns, G. W. Collins, and T. R. Boehly, "X-ray diffraction of ramp-compressed aluminum to 475 GPa," *Phys. Plasmas* **25**, 082709 (2018).
- ⁶⁹J. K. Wicks, R. F. Smith, D. E. Fratanduono, F. Coppari, R. G. Kraus, M. G. Newman, J. R. Rygg, J. H. Eggert, and T. S. Duffy, "Crystal structure and equation of state of Fe-Si alloys at super-earth core conditions," *Sci. Adv.* **4**, eaao5864 (2018).
- ⁷⁰D. H. Kalantar, J. F. Belak, G. W. Collins, J. D. Colvin, H. M. Davies, J. H. Eggert, T. C. Germann, J. Hawreliak, B. L. Holian, K. Kadau, P. S. Lomdahl, H. E. Lorenzana, M. A. Meyers, K. Rosolankova, M. S. Schneider, J. Sheppard, J. S. Stölkén, and J. S. Wark, "Direct observation of the α - ϵ transition in shock-compressed iron via nanosecond x-ray diffraction," *Phys. Rev. Lett.* **95**, 075502 (2005).
- ⁷¹J. Hawreliak, J. D. Colvin, J. H. Eggert, D. H. Kalantar, H. E. Lorenzana, J. S. Stölkén, H. M. Davies, T. C. Germann, B. L. Holian, K. Kadau, P. S. Lomdahl, A. Higginbotham, K. Rosolankova, J. Sheppard, and J. S. Wark, "Analysis of the x-ray diffraction signal for the α - ϵ transition in shock-compressed iron: Simulation and experiment," *Phys. Rev. B* **74**, 184107 (2006).
- ⁷²J. A. Hawreliak, B. El-Dasher, H. Lorenzana, G. Kimminau, A. Higginbotham, B. Nagler, S. M. Vinko, W. J. Murphy, T. Whitcher, J. S. Wark, S. Rothman, and N. Park, "In situ x-ray diffraction measurements of the c/a ratio in the high-pressure ϵ phase of shock-compressed polycrystalline iron," *Phys. Rev. B* **83**, 144114 (2011).
- ⁷³T. d'Almeida, M. Di Michiel, M. Kaiser, T. Buslaps, and A. Fanget, "Time-resolved x-ray diffraction measurements on cds shocked along the c axis," *J. Appl. Phys.* **92**, 1715–1717 (2002).
- ⁷⁴K.-D. Liss, T. d'Almeida, M. Kaiser, R. Hock, A. Magerl, and J. F. Eloy, "Time-resolved x-ray diffraction study of laser-induced shock and acoustic waves in single crystalline silicon," *J. Appl. Phys.* **106**, 044914 (2009).
- ⁷⁵K. Ichiyanagi, S.-I. Adachi, S. Nozawa, Y. Hironaka, K. G. Nakamura, T. Sato, A. Tomita, and S.-Y. Koshihara, "Shock-induced lattice deformation of CdS single crystal by nanosecond time-resolved Laue diffraction," *Appl. Phys. Lett.* **91**, 231918 (2007).
- ⁷⁶K. Ichiyanagi and G. K. Nakamura, "Structural dynamics of materials under shock compression investigated with synchrotron radiation," *Metals* **6**, 17 (2016).
- ⁷⁷J. Hu, K. Ichiyanagi, T. Doki, A. Goto, T. Eda, K. Norimatsu, S. Harada, D. Horiuchi, Y. Kabasawa, S. Hayashi, S.-I. Uozumi, N. Kawai, S. Nozawa, T. Sato, S.-I. Adachi, and K. G. Nakamura, "Complex structural dynamics of bismuth under laser-driven compression," *Appl. Phys. Lett.* **103**, 161904 (2013).
- ⁷⁸X. Wang, P. Rigg, J. Sethian, N. Sinclair, N. Weir, B. Williams, J. Zhang, J. Hawreliak, Y. Toyoda, Y. Gupta, Y. Li, D. Broege, J. Bromage, R. Earley, D. Guy, and J. Zuegel, "The laser shock station in the dynamic compression sector. I," *Rev. Sci. Instrum.* **90**, 053901 (2019).
- ⁷⁹R. Briggs, F. Coppari, M. G. Gorman, R. F. Smith, S. J. Tracy, A. L. Coleman, A. Fernandez-Pañella, M. Millot, J. H. Eggert, and D. E. Fratanduono, "Measurement of body-centered cubic gold and melting under shock compression," *Phys. Rev. Lett.* **123**, 045701 (2019).
- ⁸⁰S. M. Sharma, S. J. Turneaure, J. M. Winey, Y. Li, P. Rigg, A. Schuman, N. Sinclair, Y. Toyoda, X. Wang, J. Zhang, and Y. M. Gupta, "Structural transformation and melting in gold shock compressed to 355 GPa," *Phys. Rev. Lett.* **123**, 045702 (2019).
- ⁸¹S. M. Sharma, S. J. Turneaure, J. M. Winey, P. A. Rigg, N. Sinclair, X. Wang, Y. Toyoda, and Y. M. Gupta, "Real-time observation of stacking faults in gold shock compressed to 150 GPa," *Phys. Rev. X* **10**, 011010 (2020).
- ⁸²S. M. Sharma, S. J. Turneaure, J. M. Winey, and Y. M. Gupta, "What determines the fcc-bcc structural transformation in shock compressed noble metals?," *Phys. Rev. Lett.* **124**, 235701 (2020).
- ⁸³M. T. Beason, A. Mandal, and B. J. Jensen, "Direct observation of the hcp-bcc phase transition and melting along the principal Hugoniot of Mg," *Phys. Rev. B* **101**, 024110 (2020).
- ⁸⁴M. Cornacchia, "Linac Coherent Light Source (LCLS) design study report," 1998. <https://doi.org/10.2172/10128>.
- ⁸⁵J. Amann, W. Berg, V. Blank, F.-J. Decker, Y. Ding, P. Emma, Y. Feng, J. Frisch, D. Fritz, J. Hastings, Z. Huang, J. Krzywinski, R. Lindberg, H. Loos, A. Lutman, H.-D. Nuhn, D. Ratner, J. Rzepiela, D. Shu, Y. Shvyd'ko, S. Spampinati, S. Stoupin, S. Terentyev, E. Trakhtenberg, D. Walz, J. Welch, J. Wu, A. Zholents, and D. Zhu, "Demonstration of self-seeding in a hard-x-ray free-electron laser," *Nat. Photonics* **6**, 693–698 (2012).
- ⁸⁶I. Inoue, T. Osaka, T. Hara, T. Tanaka, T. Inagaki, T. Fukui, S. Goto, Y. Inubushi, H. Kimura, R. Kinjo, H. Ohashi, K. Togawa, K. Tono, M. Yamaga, H. Tanaka, T. Ishikawa, and M. Yabashi, "Generation of narrow-band x-ray free-electron laser via reflection self-seeding," *Nat. Photonics* **13**, 319–322 (2019).
- ⁸⁷B. Nagler, B. Arnold, G. Bouchard, R. F. Boyce, R. M. Boyce, A. Callen, M. Campell, R. Curiel, E. Galtier, J. Garofoli, E. Granados, J. Hastings, G. Hays, P. Heimann, R. W. Lee, D. Milathianaki, L. Plummer, A. Schropp, A. Wallace, M. Welch, W. White, Z. Xing, J. Yin, J. Young, U. Zastra, and H. J. Lee, "The matter in extreme conditions instrument at the Linac coherent light source," *J. Synchrotron Radiat.* **22**, 520–525 (2015).
- ⁸⁸T. Yabuuchi, A. Kon, Y. Inubushi, T. Togahi, K. Sueda, T. Itoga, K. Nakajima, H. Habara, R. Kodama, H. Tomizawa, and M. Yabashi, "An experimental platform using high-power, high-intensity optical lasers with the hard X-ray free-electron laser at SACLA," *J. Synchrotron Radiat.* **26**, 585–594 (2019).
- ⁸⁹B. Albertazzi, N. Ozaki, V. Zhakhovsky, A. Faenov, H. Habara, M. Harmand, N. Hartley, D. Ilnitsky, N. Inogamov, Y. Inubushi, T. Ishikawa, T. Katayama, T. Koyama, M. Koenig, A. Krygier, T. Matsuoka, S. Matsuyama, E. McBride, K. P. Migdal, G. Morard, H. Ohashi, T. Okuchi, T. Pikuz, N. Purejav, O. Sakata, Y. Sano, T. Sato, T. Sekine, Y. Seto, K. Takahashi, K. Tanaka, Y. Tange, T. Togashi, K. Tono, Y. Umeda, T. Vinci, M. Yabashi, T. Yabuuchi, K. Yamauchi, H. Yumoto, and R. Kodama, "Dynamic fracture of tantalum under extreme tensile stress," *Sci. Adv.* **3**, e1602705 (2017).
- ⁹⁰N. Ozaki, "Shock compression experiments using SACLA-XFEL behavior of materials at ultrahigh pressures and ultrahigh energy densities," *Hoshako* **33**, 258–265 (2020).
- ⁹¹U. Zastra, K. Appel, C. Baetz, O. Baehr, L. Batchelor, A. Berghäuser, M. Banjafar, E. Brambrink, V. Cerantola, T. E. Cowan, H. Damker, S. Dietrich, S. Di Dio Cafiso, J. Dreyer, H.-O. Engel, T. Feldmann, S. Findeisen, M. Foese, D. Fulla-Marsa, S. Göde, M. Hassan, J. Hauser, T. Herrmannsdörfer, H. Höppner, J. Kaa, P. Kaever, K. Knöfel, Z. Konôpková, A. Laso García, H.-P. Liermann, J. Mainberger, M. Makita, E.-C. Martens, E. E. McBride, D. Möller, M. Nakatsutsumi, A. Pelka, C. Plueckthun, C. Prescher, T. R. Preston, M. Röper, A. Schmidt, W. Seidel, J.-P. Schwinkendorf, M. O. Schoelmerich, U. Schramm, A. Schropp, C. Stroh, K. Sukharnikov, P. Talkovski, I. Thorpe, M. Toncian, T. Toncian, L. Wollenweber, S. Yamamoto, and T. Tschentscher, "The high energy density scientific instrument at the European XFEL," *J. Synchrotron Radiat.* **28**, 1393–1416 (2021).
- ⁹²J. Lindl, "Development of the indirect-drive approach to inertial confinement fusion and the target physics basis for ignition and gain," *Phys. Plasmas* **2**, 3933–4024 (1995).
- ⁹³M. G. Haines, "Review of inertial confinement fusion," *Astrophys. Space Sci.* **256**, 125–139 (1997).
- ⁹⁴R. G. Evans, "Laser generation of ultra high pressure," *Plasma Phys. Control. Fusion* **28**, 157–164 (1986).
- ⁹⁵W. Kruer, *The Physics of Laser Plasma Interactions* (CRC Press, 2019).

- ⁹⁶L. Schlessinger and J. Wright, "Inverse-bremsstrahlung absorption rate in an intense laser field," *Phys. Rev. A* **20**, 1934–1945 (1979).
- ⁹⁷T. Goldsack, J. Kilkenny, B. MacGowan, S. Veats, P. Cunningham, C. Lewis, M. Key, P. Rumsby, and W. Toner, "The variation of mass ablation rate with laser wavelength and target geometry," *Opt. Commun.* **42**, 55–59 (1982).
- ⁹⁸G. Mennerat, O. Bonville, B. Le Garrec, P. Villeval, S. Durst, D. Lupinski, A. Kokh, N. Kononova, V. Vlezko, and K. Kokh, "Frequency doubling and tripling for future fusion drivers," in Paper NTHA2 (Optica Publishing Group, 2011).
- ⁹⁹See <https://www.lanl.gov/org/ddste/aldsc/theoretical/physics-chemistry-materials/sesamedatabase.php> for tabular data of equations of state.
- ¹⁰⁰L. M. Barker and R. E. Hollenbach, "Laser interferometer for measuring high velocities of any reflecting surface," *J. Appl. Phys.* **43**, 4669–4675 (1972).
- ¹⁰¹P. M. Celliers, D. K. Bradley, G. W. Collins, D. G. Hicks, T. R. Boehly, and W. J. Armstrong, "Line-imaging velocimeter for shock diagnostics at the OMEGA laser facility," *Rev. Sci. Instrum.* **75**, 4916–4929 (2004).
- ¹⁰²D. H. Dolan, "Foundations of VISAR analysis," 2006. doi:10.2172/886901.
- ¹⁰³W. F. Hemsing, "Velocity sensing interferometer (VISAR) modification," *Rev. Sci. Instrum.* **50**, 73–78 (1979).
- ¹⁰⁴D. J. Erskine, R. F. Smith, C. A. Bolme, P. M. Celliers, and G. W. Collins, "Two-dimensional imaging velocity interferometry: Data analysis techniques," *Rev. Sci. Instrum.* **83**, 043116 (2012).
- ¹⁰⁵D. J. Erskine, R. F. Smith, C. A. Bolme, S. J. Ali, P. M. Celliers, and G. W. Collins, "Holographic and time-resolving ability of pulse-pair two-dimensional velocity interferometry," *Rev. Sci. Instrum.* **85**, 063115 (2014).
- ¹⁰⁶B. D. Malone, J. D. Sau, and M. L. Cohen, "Ab initio study of the optical properties of Si-XII," *Phys. Rev. B* **78**, 161202 (2008).
- ¹⁰⁷D. Hayes, "Unsteady compression waves in interferometer windows," *J. Appl. Phys.* **89**, 6484–6486 (2001).
- ¹⁰⁸M. D. Knudson and M. P. Desjarlais, "Adiabatic release measurements in α -quartz between 300 and 1200 GPa: Characterization of α -quartz as a shock standard in the multimegabar regime," *Phys. Rev. B* **88**, 184107 (2013).
- ¹⁰⁹S. Brygoo, M. Millot, P. Loubeyre, A. E. Lazicki, S. Hamel, T. Qi, P. M. Celliers, F. Coppari, J. H. Eggert, D. E. Fratanduono, D. G. Hicks, J. R. Rygg, R. F. Smith, D. C. Swift, G. W. Collins, and R. Jeanloz, "Analysis of laser shock experiments on precompressed samples using a quartz reference and application to warm dense hydrogen and helium," *J. Appl. Phys.* **118**, 195901 (2015).
- ¹¹⁰D. E. Fratanduono, P. M. Celliers, D. G. Braun, P. A. Sterne, S. Hamel, A. Shamp, E. Zurek, K. J. Wu, A. E. Lazicki, M. Millot, and G. W. Collins, "Equation of state, adiabatic sound speed, and Grüneisen coefficient of boron carbide along the principal Hugoniot to 700 GPa," *Phys. Rev. B* **94**, 184107 (2016).
- ¹¹¹B. J. Jensen, D. B. Holtkamp, P. A. Rigg, and D. H. Dolan, "Accuracy limits and window corrections for photon doppler velocimetry," *J. Appl. Phys.* **101**, 013523 (2007).
- ¹¹²A. Dewaele, J. H. Eggert, P. Loubeyre, and R. Le Toullec, "Measurement of refractive index and equation of state in dense He, H₂, H₂O, and Ne under high pressure in a diamond anvil cell," *Phys. Rev. B* **67**, 094112 (2003).
- ¹¹³Y. J. Kim, P. M. Celliers, J. H. Eggert, A. Lazicki, and M. Millot, "Interferometric measurements of refractive index and dispersion at high pressure," *Sci. Rep.* **11**, 5610 (2021).
- ¹¹⁴J.-P. Davis, M. D. Knudson, L. Shulenburg, and S. D. Crockett, "Mechanical and optical response of [100] lithium fluoride to multi-megabar dynamic pressures," *J. Appl. Phys.* **120**, 165901 (2016).
- ¹¹⁵L. E. Kirsch, S. J. Ali, D. E. Fratanduono, R. G. Kraus, D. G. Braun, A. Fernandez-Pañella, R. F. Smith, J. M. McNaney, and J. H. Eggert, "Refractive index of lithium fluoride to 900 GPa and implications for dynamic equation of state measurements," *J. Appl. Phys.* **125**, 175901 (2019).
- ¹¹⁶A. Nikroo, "A growing family of targets for the National Ignition Facility," *Sci. Technol. Rev.* 2016, 4–11; available at <https://str.llnl.gov/january-2016>
- ¹¹⁷I. Principe, J. Fuchs, S. Pascarelli, D. W. Schumacher, R. B. Stephens, N. B. Alexander, R. Briggs, M. Büscher, M. O. Cernaianu, A. Choukourou, M. D. Marco, A. Erbe, J. Fassbender, G. Fiquet, P. Fitzsimmons, C. Gheorghiu, J. Hund, L. G. Huang, M. Harmand, N. J. Hartley, A. Irman, T. Kluge, Z. Konopkova, S. Kraft, D. Kraus, V. Leca, D. Margarone, J. Metzkes, K. Nagai, W. Nazarov, P. Lutoslawski, D. Papp, M. Passoni, A. Pelka, J. P. Perin, J. Schulz, M. Smid, C. Spindloe, S. Steinke, R. Torchio, C. Vass, T. Wiste, R. Zaffino, K. Zeil, T. Tschentscher, U. Schramm, and T. E. Cowan, "Targets for high repetition rate laser facilities: Needs, challenges and perspectives," *High Power Laser Sci. Eng.* **5**, 1–31 (2017).
- ¹¹⁸R. Jeanloz, P. M. Celliers, G. W. Collins, J. H. Eggert, K. K. M. Lee, R. S. McWilliams, S. Brygoo, and P. Loubeyre, "Achieving high-density states through shock-wave loading of precompressed samples," *Proc. Natl. Acad. Sci.* **104**, 9172–9177 (2007).
- ¹¹⁹P. M. Celliers, M. Millot, S. Brygoo, R. S. McWilliams, D. E. Fratanduono, J. R. Rygg, A. F. Goncharov, P. Loubeyre, J. H. Eggert, J. L. Peterson, N. B. Meezan, S. Le Pape, G. W. Collins, R. Jeanloz, and H. R. J., "Insulator-metal transition in dense fluid deuterium," *Science* **361**, 677–682 (2018).
- ¹²⁰M. Millot, F. Coppari, J. R. Rygg, A. Correa-Barrios, S. Hamel, D. C. Swift, and J. H. Eggert, "Nanosecond x-ray diffraction of shock-compressed superionic water ice," *Nature* **569**, 251–255 (2019).
- ¹²¹M. G. Gorman, A. L. Coleman, R. Briggs, R. S. McWilliams, D. McGonegle, C. A. Bolme, A. E. Gleason, E. Galtier, H. J. Lee, E. Granados, M. Šliwa, C. Sanloup, S. Rothman, D. E. Fratanduono, R. F. Smith, G. W. Collins, J. H. Eggert, J. S. Wark, and M. I. McMahon, "Femtosecond diffraction studies of solid and liquid phase changes in shock-compressed bismuth," *Sci. Rep.* **8**, 16927 (2018).
- ¹²²M. G. Gorman, D. McGonegle, S. J. Tracy, S. M. Clarke, C. A. Bolme, A. E. Gleason, S. J. Ali, S. Hok, C. W. Greeff, P. G. Heighway, K. Hulpach, B. Glam, E. Galtier, H. J. Lee, J. S. Wark, J. H. Eggert, J. K. Wicks, and R. F. Smith, "Recovery of a high-pressure phase formed under laser-driven compression," *Phys. Rev. B* **102**, 024101 (2020).
- ¹²³C. E. Wehrenberg, D. McGonegle, C. Bolme, A. Higginbotham, A. Lazicki, H. J. Lee, B. Nagler, H.-S. Park, B. A. Remington, R. E. Rudd, M. Sliwa, M. Suggit, D. Swift, F. Tavella, L. Zepeda-Ruiz, and J. S. Wark, "In situ x-ray diffraction measurement of shock-wave-driven twinning and lattice dynamics," *Nature* **550**, 496–499 (2017).
- ¹²⁴R. F. Smith, V. Rastogi, A. E. Lazicki, M. G. Gorman, R. Briggs, A. L. Coleman, C. Davis, S. Singh, D. McGonegle, S. M. Clarke, T. Volz, T. Hutchinson, C. McGuire, D. E. Fratanduono, D. C. Swift, E. Folsom, C. A. Bolme, A. E. Gleason, F. Coppari, H. J. Lee, B. Nagler, E. Cunningham, E. Granados, P. Heimann, R. G. Kraus, R. E. Rudd, T. S. Duffy, J. H. Eggert, and J. K. Wicks, "Development of slurry targets for high repetition-rate XFEL experiments," *arXiv:2201.04254* [hep-ex] (2022).
- ¹²⁵J. T. Larsen and S. M. Lane, "HYADES—A plasma hydrodynamics code for dense plasma studies," *J. Quant. Spectrosc. Radiat. Transfer* **51**, 179–186 (1994).
- ¹²⁶K.-J. Boehm, N. Alexander, J. Anderson, L. Carlson, and M. Farrell, "Assembly and metrology of NIF target subassemblies using robotic systems," *High Power Laser Sci. Eng.* **5**, e25 (2017).
- ¹²⁷C. Spindloe, Y. Fukuda, P. Fitzsimmons, K. Du, and C. Danson, "Review of HPLSE special issue on target fabrication," *High Power Laser Sci. Eng.* **6**, e13 (2018).
- ¹²⁸See https://www.ga.com/inertial-fusion/img/target_dev_and_fabrication_Target_1102_0919_vfinal2.pdf for information on targets to be used at high repetition rates.
- ¹²⁹P. Mason, S. Banerjee, J. Smith, T. Butcher, J. Phillips, H. Höppner, D. Möller, K. Ertel, M. De Vido, I. Hollingham, A. Norton, S. Tomlinson, T. Zata, J. S. Merchan, C. Hooker, M. Tyldesley, T. Toncian, C. Hernandez-Gomez, C. Edwards, and J. Collier, "Development of a 100 J, 10 Hz laser for compression experiments at the high energy density instrument at the European XFEL," *High Power Laser Sci. Eng.* **6**, e65 (2018).
- ¹³⁰R. Kraus, S. Stewart, A. Seifter, and A. Obst, "Shock and post-shock temperatures in an ice-quartz mixture: Implications for melting during planetary impact events," *Earth Planet. Sci. Lett.* **289**, 162–170 (2010).
- ¹³¹J. R. Asay, G. R. Fowles, G. E. Durrall, M. H. Miles, and R. F. Tinder, "Effects of point defects on elastic precursor decay in LiF," *J. Appl. Phys.* **43**, 2132–2145 (1972).

- ¹³²G. I. Kanel, "Unusual behaviour of usual materials in shock waves," *J. Phys.: Conf. Ser.* **500**, 012001 (2014).
- ¹³³E. M. Bringa, K. Rosolankova, R. E. Rudd, B. A. Remington, J. S. Wark, M. Duchaineau, D. H. Kalantar, J. Hawreliak, and J. Belak, "Shock deformation of face-centred-cubic metals on subnanosecond timescales," *Nat. Mater.* **5**, 805–809 (2006).
- ¹³⁴E. Orowan, "A type of plastic deformation new in metals," *Nature* **149**, 643–644 (1942).
- ¹³⁵V. Dupont and T. C. Germann, "Strain rate and orientation dependencies of the strength of single crystalline copper under compression," *Phys. Rev. B* **86**, 134111 (2012).
- ¹³⁶D. Milathianaki, S. Boutet, G. J. Williams, A. Higginbotham, D. Ratner, A. E. Gleason, M. Messerschmidt, M. M. Seibert, D. C. Swift, P. Hering, J. Robinson, W. E. White, and J. S. Wark, "Femtosecond visualization of lattice dynamics in shock-compressed matter," *Science* **342**, 220–223 (2013).
- ¹³⁷H. T. Philipp, M. Hromalik, M. Tate, L. Koerner, and S. M. Gruner, "Pixel array detector for x-ray free electron laser experiments," *Nucl. Instrum. Methods Phys. Res., Sect. A* **649**, 67–69 (2011).
- ¹³⁸G. Blaj, P. Caragiulo, G. Carini, S. Carron, A. Dragone, D. Freytag, G. Haller, P. Hart, J. Hasi, R. Herbst, S. Herrmann, C. Kenney, B. Markovic, K. Nishimura, S. Osier, J. Pines, B. Reese, J. Segal, A. Tomada, and M. Weaver, "X-ray detectors at the Linac Coherent Light Source," *J. Synchrotron Radiat.* **22**, 577–583 (2015).
- ¹³⁹J. S. Wark, A. Higginbotham, D. Milathianaki, and A. Gleason, "Combined hydrodynamic and diffraction simulations of femtosecond x-ray scattering from laser-shocked crystals," *J. Phys.: Conf. Ser.* **500**, 152016 (2014).
- ¹⁴⁰D. McGonegle, D. Milathianaki, B. A. Remington, J. S. Wark, and A. Higginbotham, "Simulations of *in situ* x-ray diffraction from uniaxially compressed highly textured polycrystalline targets," *J. Appl. Phys.* **118**, 065902 (2015).
- ¹⁴¹E. Schmid, "Über die schubverfestigung von einkristallen bei plastischer deformation," *Z. Phys.* **40**, 54–74 (1926).
- ¹⁴²E. Schmid and W. Boas, *Kristallplastizität: Mit Besonderer Berücksichtigung der Metalle* (Springer-Verlag, Berlin, 1935), pp. 59–62.
- ¹⁴³M. Sliwa, D. McGonegle, C. Wehrenberg, C. A. Bolme, P. G. Heighway, A. Higginbotham, A. Lazicki, H. J. Lee, B. Nagler, H. S. Park, R. E. Rudd, M. J. Suggit, D. Swift, F. Tavella, L. Zepeda-Ruiz, B. A. Remington, and J. S. Wark, "Femtosecond x-ray diffraction studies of the reversal of the microstructural effects of plastic deformation during shock release of tantalum," *Phys. Rev. Lett.* **120**, 265502 (2018).
- ¹⁴⁴P. G. Heighway, M. Sliwa, D. McGonegle, C. Wehrenberg, C. A. Bolme, J. Eggert, A. Higginbotham, A. Lazicki, H. J. Lee, B. Nagler, H.-S. Park, R. E. Rudd, R. F. Smith, M. J. Suggit, D. Swift, F. Tavella, B. A. Remington, and J. S. Wark, "Nonisotropic release of a shocked solid," *Phys. Rev. Lett.* **123**, 245501 (2019).
- ¹⁴⁵M. J. MacDonald, E. E. McBride, E. Galtier, M. Gauthier, E. Granados, D. Kraus, A. Krygier, A. L. Levitan, A. J. MacKinnon, I. Nam, W. Schumaker, P. Sun, T. B. van Driel, J. Vorberger, Z. Xing, R. P. Drake, S. H. Glenzer, and L. B. Fletcher, "Using simultaneous x-ray diffraction and velocity interferometry to determine material strength in shock-compressed diamond," *Appl. Phys. Lett.* **116**, 234104 (2020).
- ¹⁴⁶W. H. Gust and E. B. Royce, "Axial yield strengths and two successive phase transition stresses for crystalline silicon," *J. Appl. Phys.* **42**, 1897–1905 (1971).
- ¹⁴⁷A. Loveridge-Smith, A. Allen, J. Belak, T. Boehly, A. Hauer, B. Holian, D. Kalantar, G. Kyrala, R. W. Lee, P. Lomdahl, M. A. Meyers, D. Paisley, S. Pollaine, B. Remington, D. C. Swift, S. Weber, and J. S. Wark, "Anomalous elastic response of silicon to uniaxial shock compression on nanosecond time scales," *Phys. Rev. Lett.* **86**, 2349–2352 (2001).
- ¹⁴⁸S. J. Turneaure and Y. M. Gupta, "Inelastic deformation and phase transformation of shock compressed silicon single crystals," *Appl. Phys. Lett.* **91**, 201913 (2007).
- ¹⁴⁹S. J. Turneaure and Y. M. Gupta, "X-ray diffraction and continuum measurements in silicon crystals shocked below the elastic limit," *Appl. Phys. Lett.* **90**, 051905 (2007).
- ¹⁵⁰R. F. Smith, R. W. Minich, R. E. Rudd, J. H. Eggert, C. A. Bolme, S. L. Bryggo, A. M. Jones, and G. W. Collins, "Orientation and rate dependence in high strain-rate compression of single-crystal silicon," *Phys. Rev. B* **86**, 245204 (2012).
- ¹⁵¹G. Mogni, A. Higginbotham, K. Gaál-Nagy, N. Park, and J. S. Wark, "Molecular dynamics simulations of shock-compressed single-crystal silicon," *Phys. Rev. B* **89**, 064104 (2014).
- ¹⁵²A. Higginbotham, P. G. Stubble, A. J. Comley, J. H. Eggert, J. M. Foster, D. H. Kalantar, D. McGonegle, S. Patel, L. J. Peacock, S. D. Rothman, R. F. Smith, M. J. Suggit, and J. S. Wark, "Inelastic response of silicon to shock compression," *Sci. Rep.* **6**, 24211 (2016).
- ¹⁵³E. E. McBride, A. Krygier, A. Ehnes, E. Galtier, M. Harmand, Z. Konôpková, H. J. Lee, H.-P. Liermann, B. Nagler, A. Pelka, M. Rödel, A. Schropp, R. F. Smith, C. Spindloe, D. Swift, F. Tavella, S. Toleikis, T. Tschentscher, J. S. Wark, and A. Higginbotham, "Phase transition lowering in dynamically compressed silicon," *Nat. Phys.* **15**, 89–94 (2019).
- ¹⁵⁴M. I. McMahon, R. J. Nelves, N. G. Wright, and D. R. Allan, "Pressure dependence of the Imma phase of silicon," *Phys. Rev. B* **50**, 739–743 (1994).
- ¹⁵⁵M. C. Gupta and A. L. Ruoff, "Static compression of silicon in the [100] and in the [111] directions," *J. Appl. Phys.* **51**, 1072–1075 (1980).
- ¹⁵⁶S. Pandolfi, S. B. Brown, P. G. Stubble, A. Higginbotham, C. A. Bolme, H. J. Lee, B. Nagler, E. Galtier, R. Sandberg, W. Yang, W. L. Mao, J. S. Wark, and A. Gleason, "Ultra-fast visualization of deformation mechanism for dynamically-compressed silicon," *arXiv:2106.06108 [cond-mat.mtrl-sci]* (2021).
- ¹⁵⁷S. J. Turneaure, N. Sinclair, and Y. M. Gupta, "Real-time examination of atomistic mechanisms during shock-induced structural transformation in silicon," *Phys. Rev. Lett.* **117**, 045502 (2016).
- ¹⁵⁸R. J. Nelves, D. R. Allan, M. I. McMahon, and S. A. Belmonte, "Self-hosting incommensurate structure of barium IV," *Phys. Rev. Lett.* **83**, 4081–4084 (1999).
- ¹⁵⁹M. I. McMahon, O. Degtyareva, and R. J. Nelves, "Ba-IV-type incommensurate crystal structure in group-V metals," *Phys. Rev. Lett.* **85**, 4896–4899 (2000).
- ¹⁶⁰K. Takemura, K. Sato, H. Fujihisa, and M. Onoda, "Modulated structure of solid iodine during its molecular dissociation under high pressure," *Nature* **423**, 971–974 (2003).
- ¹⁶¹C. Hejny and M. I. McMahon, "Large structural modulations in incommensurate Te-III and Se-IV," *Phys. Rev. Lett.* **91**, 215502 (2003).
- ¹⁶²L. F. Lundegaard, E. Gregoryanz, M. I. McMahon, C. Guillaume, I. Loa, and R. J. Nelves, "Single-crystal studies of incommensurate Na to 1.5 Mbar," *Phys. Rev. B* **79**, 064105 (2009).
- ¹⁶³M. I. McMahon, R. J. Nelves, U. Schwarz, and K. Syassen, "Composite incommensurate K-III and a commensurate form: Study of a high-pressure phase of potassium," *Phys. Rev. B* **74**, 140102 (2006).
- ¹⁶⁴M. I. McMahon, S. Rekhi, and R. J. Nelves, "Pressure dependent incommensuration in Rb-IV," *Phys. Rev. Lett.* **87**, 055501 (2001).
- ¹⁶⁵O. Degtyareva, M. I. McMahon, and R. J. Nelves, "Pressure-induced incommensurate-to-incommensurate phase transition in antimony," *Phys. Rev. B* **70**, 184119 (2004).
- ¹⁶⁶C. Hejny, L. F. Lundegaard, S. Falconi, M. I. McMahon, and M. Hanfland, "Incommensurate sulfur above 100 GPa," *Phys. Rev. B* **71**, 020101 (2005).
- ¹⁶⁷H. Fujihisa, Y. Akahama, H. Kawamura, Y. Ohishi, Y. Gotoh, H. Yamawaki, M. Sakashita, S. Takeya, and K. Honda, "Incommensurate structure of phosphorus phase IV," *Phys. Rev. Lett.* **98**, 175501 (2007).
- ¹⁶⁸T. Kume, T. Hiraoka, Y. Ohya, S. Sasaki, and H. Shimizu, "High pressure Raman study of bromine and iodine: Soft phonon in the incommensurate phase," *Phys. Rev. Lett.* **94**, 065506 (2005).
- ¹⁶⁹P. Dalladay-Simpson, J. Binns, M. Peña-Alvarez, M.-E. Donnelly, E. Greenberg, V. Prakapenka, X.-J. Chen, E. Gregoryanz, and R. T. Howie, "Band gap closure, incommensurability and molecular dissociation of dense chlorine," *Nat. Commun.* **10**, 1134 (2019).
- ¹⁷⁰H. Fujihisa, Y. Akahama, H. Kawamura, Y. Gotoh, H. Yamawaki, M. Sakashita, S. Takeya, and K. Honda, "Incommensurate composite crystal structure of scandium-II," *Phys. Rev. B* **72**, 132103 (2005).

- ¹⁷¹R. J. Husband, I. Loa, G. W. Stinton, S. R. Evans, G. J. Ackland, and M. I. McMahon, "Europium-IV: An incommensurately modulated crystal structure in the lanthanides," *Phys. Rev. Lett.* **109**, 095503 (2012).
- ¹⁷²S. Van Smalen, "Incommensurate crystal structures," *Crystallogr. Rev.* **4**, 79–202 (1995).
- ¹⁷³M. I. McMahon and R. J. Nemes, "Chain 'melting' in the composite Rb-IV structure," *Phys. Rev. Lett.* **93**, 055501 (2004).
- ¹⁷⁴E. E. McBride, K. A. Munro, G. W. Stinton, R. J. Husband, R. Briggs, H.-P. Liermann, and M. I. McMahon, "One-dimensional chain melting in incommensurate potassium," *Phys. Rev. B* **91**, 144111 (2015).
- ¹⁷⁵R. F. Smith, J. H. Eggert, M. D. Saculla, A. F. Jankowski, M. Bastea, D. G. Hicks, and G. W. Collins, "Ultrafast dynamic compression technique to study the kinetics of phase transformations in bismuth," *Phys. Rev. Lett.* **101**, 065701 (2008).
- ¹⁷⁶A. L. Coleman, M. G. Gorman, R. Briggs, R. S. McWilliams, D. McGonegle, C. A. Bolme, A. E. Gleason, D. E. Fratanduono, R. F. Smith, E. Galtier, H. J. Lee, B. Nagler, E. Granados, G. W. Collins, J. H. Eggert, J. S. Wark, and M. I. McMahon, "Identification of phase transitions and metastability in dynamically compressed antimony using ultrafast x-ray diffraction," *Phys. Rev. Lett.* **122**, 255704 (2019).
- ¹⁷⁷C. M. Pépin, A. Sollier, A. Marizy, F. Occelli, M. Sander, R. Torchio, and P. Loubeyre, "Kinetics and structural changes in dynamically compressed bismuth," *Phys. Rev. B* **100**, 060101 (2019).
- ¹⁷⁸R. Briggs, M. G. Gorman, A. L. Coleman, R. S. McWilliams, E. E. McBride, D. McGonegle, J. S. Wark, L. Peacock, S. Rothman, S. G. Macleod, C. A. Bolme, A. E. Gleason, G. W. Collins, J. H. Eggert, D. E. Fratanduono, R. F. Smith, E. Galtier, E. Granados, H. J. Lee, B. Nagler, I. Nam, Z. Xing, and M. I. McMahon, "Ultrafast x-ray diffraction studies of the phase transitions and equation of state of scandium shock compressed to 82 GPa," *Phys. Rev. Lett.* **118**, 025501 (2017).
- ¹⁷⁹R. Briggs, M. G. Gorman, S. Zhang, D. McGonegle, A. L. Coleman, F. Coppari, M. A. Morales-Silva, R. F. Smith, J. K. Wicks, C. A. Bolme, A. E. Gleason, E. Cunningham, H. J. Lee, B. Nagler, M. I. McMahon, J. H. Eggert, and D. E. Fratanduono, "Coordination changes in liquid tin under shock compression determined using *in situ* femtosecond x-ray diffraction," *Appl. Phys. Lett.* **115**, 264101 (2019).
- ¹⁸⁰R. J. Husband, E. F. O'Bannon, H.-P. Liermann, M. J. Lipp, A. S. J. Méndez, Z. Konôpková, E. E. McBride, W. J. Evans, and Z. Jenei, "Compression-rate dependence of pressure-induced phase transitions in Bi," *Sci. Rep.* **11**, 14859 (2021).
- ¹⁸¹P. Song and L. Cai, "Multiphase equation of state for lead," *Physica B* **405**, 1509–1512 (2010).
- ¹⁸²C. Dai, J. Hu, and H. Tan, "Hugoniot temperatures and melting of tantalum under shock compression determined by optical pyrometry," *J. Appl. Phys.* **106**, 043519 (2009).
- ¹⁸³F. Stacey, "High pressure equations of state and planetary interiors," *Rep. Prog. Phys.* **68**, 341 (2005).
- ¹⁸⁴R. Helled and T. Guillot, "Internal structure of giant and icy planets: Importance of heavy elements and mixing," in *Handbook of Exoplanets*, edited by H. J. Deeg and J. A. Belmonte (Springer International Publishing, Cham, 2017), pp. 1–19.
- ¹⁸⁵J. Wark, "High energy density science with x-ray free-electron lasers," *Proc. Int. Sch. Phys. "Enrico Fermi"* **199**, 147–170 (2020).
- ¹⁸⁶A. Higginbotham, J. Hawrelak, E. M. Bringa, G. Kimminau, N. Park, E. Reed, B. A. Remington, and J. S. Wark, "Molecular dynamics simulations of ramp-compressed copper," *Phys. Rev. B* **85**, 024112 (2012).
- ¹⁸⁷D. C. Swift and R. P. Johnson, "Quasi-isentropic compression by ablative laser loading: Response of materials to dynamic loading on nanosecond time scales," *Phys. Rev. E* **71**, 066401 (2005).
- ¹⁸⁸J. M. Walsh, M. H. Rice, R. G. McQueen, and F. L. Yarger, "Shock-wave compressions of twenty-seven metals. Equations of state of metals," *Phys. Rev.* **108**, 196–216 (1957).
- ¹⁸⁹D. E. Grady, "Strain rate dependence of the effective viscosity under steady wave shock compression," *Appl. Phys. Lett.* **38**, 825–826 (1981).
- ¹⁹⁰J. W. Swegle and D. E. Grady, "Shock viscosity and the prediction of shock wave rise times," *J. Appl. Phys.* **58**, 692–701 (1985).
- ¹⁹¹D. E. Grady, "Unifying role of dissipative action in the dynamic failure of solids," *J. Appl. Phys.* **117**, 165905 (2015).
- ¹⁹²A. Higginbotham, E. M. Bringa, J. Marian, N. Park, M. Suggit, and J. S. Wark, "Simulations of copper single crystals subjected to rapid shear," *J. Appl. Phys.* **109**, 063530 (2011).
- ¹⁹³R. F. Smith, J. H. Eggert, A. Jankowski, P. M. Celliers, M. J. Edwards, Y. M. Gupta, J. R. Asay, and G. W. Collins, "Stiff response of aluminum under ultrafast shockless compression to 110 GPa," *Phys. Rev. Lett.* **98**, 065701 (2007).
- ¹⁹⁴S. D. Rothman, J.-P. Davis, J. Maw, C. M. Robinson, K. Parker, and J. Palmer, "Measurement of the principal isentropes of lead and lead-antimony alloy to ~400 kbar by quasi-isentropic compression," *J. Phys. D: Appl. Phys.* **38**, 733–740 (2005).
- ¹⁹⁵D. E. Fratanduono, R. F. Smith, D. G. Braun, J. R. Patterson, R. G. Kraus, T. S. Perry, A. Arsenlis, G. W. Collins, and J. H. Eggert, "The effect of nearly steady shock waves in ramp compression experiments," *J. Appl. Phys.* **117**, 245903 (2015).
- ¹⁹⁶D. C. Swift, R. G. Kraus, E. N. Loomis, D. G. Hicks, J. M. McNaney, and R. P. Johnson, "Shock formation and the ideal shape of ramp compression waves," *Phys. Rev. E* **78**, 066115 (2008).
- ¹⁹⁷D. Kraus, J. Vorberger, A. Pak, N. Hartley, L. Fletcher, S. Frydrych, E. Galtier, E. Gamboa, D. O. Gericke, S. Glenzer, E. Granados, M. MacDonald, A. MacKinnon, E. McBride, I. Nam, P. Neumayer, M. Roth, A. M. Saunders, A. Schuster, P. Sun, T. van Driel, T. Döppner, and R. Falcone, "Formation of diamonds in laser-compressed hydrocarbons at planetary interior conditions," *Nat. Astron.* **1**, 606–611 (2017).
- ¹⁹⁸G. I. Taylor and H. Quinney, "The latent energy remaining in a metal after cold working," *Proc. R. Soc. London, Ser. A* **143**, 307–326 (1934).
- ¹⁹⁹J. Mason, A. Rosakis, and G. Ravichandran, "On the strain and strain rate dependence of the fraction of plastic work converted to heat: An experimental study using high speed infrared detectors and the Kolsky bar," *Mech. Mater.* **17**, 135–145 (1994).
- ²⁰⁰D. J. Steinberg, S. G. Cochran, and M. W. Guinan, "A constitutive model for metals applicable at high strain rate," *J. Appl. Phys.* **51**, 1498–1504 (1980).
- ²⁰¹D. L. Preston, D. L. Tonks, and D. C. Wallace, "Model of plastic deformation for extreme loading conditions," *J. Appl. Phys.* **93**, 211–220 (2003).
- ²⁰²R. E. Rudd, A. Arsenlis, N. R. Barton, R. M. Cavallo, A. J. Comley, B. R. Maddox, J. Marian, H.-S. Park, S. T. Prisbrey, C. E. Wehrenberg, L. Zepeda-Ruiz, and B. A. Remington, "Multiscale strength (MS) models: Their foundation, their successes, and their challenges," *J. Phys.: Conf. Ser.* **500**, 112055 (2014).
- ²⁰³N. R. Barton and M. Rhee, "A multiscale strength model for tantalum over an extended range of strain rates," *J. Appl. Phys.* **114**, 123507 (2013).
- ²⁰⁴B. Remington, R. Rudd, N. Barton, R. Cavallo, H.-S. Park, J. Belof, A. Comley, B. Maddox, M. May, S. Pollaine, and S. Prisbrey, "Interpretation of laser-driven V and Ta Rayleigh-Taylor strength experiments," *AIP Conf. Proc.* **1426**, 1375 (2012).
- ²⁰⁵B. A. Remington, H.-S. Park, D. T. Casey, R. M. Cavallo, D. S. Clark, C. M. Huntington, C. C. Kuran, A. R. Miles, S. R. Nagel, K. S. Raman, and V. A. Smalyuk, "Rayleigh-Taylor instabilities in high-energy density settings on the National Ignition Facility," *Proc. Natl. Acad. Sci.* **116**, 18233–18238 (2019).
- ²⁰⁶P. Avraam, D. McGonegle, P. G. Heighway, C. E. Wehrenberg, E. Floyd, A. Comley, J. M. Foster, J. Turner, S. Case, and J. S. Wark, "Crystal plasticity finite element simulation of lattice rotation and x-ray diffraction during laser shock-compression of tantalum," *arXiv:2108.05166 [cond-mat.mtrl-sci]* (2021).
- ²⁰⁷M. Suggit, A. Higginbotham, G. Moggi, G. Kimminau, P. Dunne, A. Comley, N. Park, B. Remington, and J. Wark, "Nanosecond white-light laue diffraction measurements of dislocation microstructure in shock-compressed single-crystal copper," *Nat. Commun.* **3**, 1224 (2012).
- ²⁰⁸P. G. Heighway and J. S. Wark, "Kinematics of slip-induced rotation for uni-axial shock or ramp compression," *J. Appl. Phys.* **129**, 085109 (2021).

- ²⁰⁹P. G. Heighway and J. S. Wark, "Slip competition and rotation suppression in tantalum and copper during dynamic uniaxial compression," [arXiv:2202.08813 \[cond-mat.mtrl-sci\]](#) (2022).
- ²¹⁰P. G. Heighway, D. McGonegle, N. Park, A. Higginbotham, and J. S. Wark, "Molecular dynamics simulations of grain interactions in shock-compressed highly textured columnar nanocrystals," *Phys. Rev. Mater.* **3**, 083602 (2019).
- ²¹¹F. González-Cataldo, B. K. Godwal, K. Driver, R. Jeanloz, and B. Militzer, "Model of ramp compression of diamond from *ab initio* simulations," *Phys. Rev. B* **104**, 134104 (2021).
- ²¹²D. C. Swift, O. Heuzé, A. Lazicki, S. Hamel, L. X. Benedict, R. F. Smith, J. M. McNaney, and G. J. Ackland, "Equation of state and strength of diamond in high-pressure ramp loading," *Phys. Rev. B* **105**, 014109 (2022).
- ²¹³R. G. Kraus, F. Coppari, D. E. Fratanduono, R. F. Smith, A. Lazicki, C. Wehrenberg, J. H. Eggert, J. R. Rygg, and G. W. Collins, "Melting of tantalum at multimegabar pressures on the nanosecond timescale," *Phys. Rev. Lett.* **126**, 255701 (2021).
- ²¹⁴P.-L. Hereil and C. Mabire, "Temperature measurement of tin under shock compression," *J. Phys. IV Fr.* **10**, Pr9-799–Pr9-804 (2000).
- ²¹⁵D. A. Brantley, R. S. Crum, and M. C. Akin, "Comparing temperature convergence of shocked thin films of tin and iron to a bulk temperature source," *J. Appl. Phys.* **129**, 015903 (2021).
- ²¹⁶M. Millot, S. Hamel, J. R. Rygg, P. M. Celliers, G. W. Collins, F. Coppari, D. E. Fratanduono, R. Jeanloz, D. C. Swift, and J. H. Eggert, "Experimental evidence for superionic water ice using shock compression," *Nat. Phys.* **14**, 297–302 (2018).
- ²¹⁷W. J. Murphy, A. Higginbotham, J. S. Wark, and N. Park, "Temperature measurements of shocked crystals by use of nanosecond x-ray diffraction," *AIP Conf. Proc.* **955**, 325–328 (2007).
- ²¹⁸W. J. Murphy, A. Higginbotham, J. S. Wark, and N. Park, "Molecular dynamics simulations of the Debye-Waller effect in shocked copper," *Phys. Rev. B* **78**, 014109 (2008).
- ²¹⁹Y. Ping, F. Coppari, D. G. Hicks, B. Yaakobi, D. E. Fratanduono, S. Hamel, J. H. Eggert, J. R. Rygg, R. F. Smith, D. C. Swift, D. G. Braun, T. R. Boehly, and G. W. Collins, "Solid iron compressed up to 560 GPa," *Phys. Rev. Lett.* **111**, 065501 (2013).
- ²²⁰Y. Ping and F. Coppari, "Laser shock XAFS studies at OMEGA facility," *High Pressure Res.* **36**, 303–314 (2016).
- ²²¹P. Scardi, L. Rebuffi, M. Abdellatif, A. Flor, and A. Leonardi, "Debye-Waller coefficient of heavily deformed nanocrystalline iron," *J. Appl. Crystallogr.* **50**, 508–518 (2017).
- ²²²S. M. Sharma and Y. M. Gupta, "Inherent issues regarding the use of in situ x-ray diffraction measurements to determine temperature in shock-compressed metals," *Phys. Rev. B* **104**, 064113 (2021).
- ²²³E. E. McBride, T. G. White, A. Descamps, L. B. Fletcher, K. Appel, F. P. Condamine, C. B. Curry, F. Dallari, S. Funk, E. Galtier, M. Gauthier, S. Goede, J. B. Kim, H. J. Lee, B. K. Ofori-Okai, M. Oliver, A. Rigby, C. Schoenwaelder, P. Sun, T. Tschentscher, B. B. L. Witte, U. Zastrau, G. Gregori, B. Nagler, J. Hastings, S. H. Glenzer, and G. Monaco, "Setup for meV-resolution inelastic X-ray scattering measurements and X-ray diffraction at the matter in extreme conditions endstation at the Linac coherent light source," *Rev. Sci. Instrum.* **89**, 10F104 (2018).
- ²²⁴P. Vieillefosse and J. P. Hansen, "Statistical mechanics of dense ionized matter. V. Hydrodynamic limit and transport coefficients of the classical one-component plasma," *Phys. Rev. A* **12**, 1106–1116 (1975).
- ²²⁵E. Burkel, "Phonon spectroscopy by inelastic x-ray scattering," *Rep. Prog. Phys.* **63**, 171–232 (2000).
- ²²⁶S. K. Sinha, "Theory of inelastic x-ray scattering from condensed matter," *J. Phys.: Condens. Matter* **13**, 7511–7523 (2001).
- ²²⁷T. Scopigno, G. Ruocco, and F. Sette, "Microscopic dynamics in liquid metals: The experimental point of view," *Rev. Mod. Phys.* **77**, 881–933 (2005).
- ²²⁸A. Descamps, B. K. Ofori-Okai, K. Appel, V. Cerantola, A. Comley, J. H. Eggert, L. B. Fletcher, D. O. Gericke, S. Göde, O. Humphries, O. Karnbach, A. Lazicki, R. Loetzsch, D. McGonegle, C. A. J. Palmer, C. Plueckthun, T. R. Preston, R. Redmer, D. G. Senesky, C. Strohm, I. Uschmann, T. G. White, L. Wollenweber, G. Monaco, J. S. Wark, J. B. Hastings, U. Zastrau, G. Gregori, S. H. Glenzer, and E. E. McBride, "An approach for the measurement of the bulk temperature of single crystal diamond using an x-ray free electron laser," *Sci. Rep.* **10**, 14564 (2020).
- ²²⁹L. Wollenweber, T. R. Preston, A. Descamps, V. Cerantola, A. Comley, J. H. Eggert, L. B. Fletcher, G. Geloni, D. O. Gericke, S. H. Glenzer, S. Göde, J. Hastings, O. S. Humphries, A. Jenei, O. Karnbach, Z. Konopkova, R. Loetzsch, B. Marx-Glowna, E. E. McBride, D. McGonegle, G. Monaco, B. K. Ofori-Okai, C. A. J. Palmer, C. Plueckthun, R. Redmer, C. Strohm, I. Thorpe, T. Tschentscher, I. Uschmann, J. S. Wark, T. G. White, K. Appel, G. Gregori, and U. Zastrau, "High-resolution inelastic x-ray scattering at the high energy density scientific instrument at the free-electron laser," *Rev. Sci. Instrum.* **92**, 013101 (2021).
- ²³⁰J. Feldhaus, E. Saldin, J. Schneider, E. Schneidmiller, and M. Yurkov, "Possible application of x-ray optical elements for reducing the spectral bandwidth of an X-ray SASE FEL," *Opt. Commun.* **140**, 341–352 (1997).
- ²³¹E. Saldin, E. Schneidmiller, Y. Shvyd'ko, and M. Yurkov, "X-ray FEL with a meV bandwidth," *Nucl. Instrum. Methods Phys. Res., Sect. A* **475**, 357–362 (2001).
- ²³²A. Baron, "Phonons in crystals using inelastic x-ray scattering," *J. Spectrosc. Soc. Jpn.* **58**, 205 (2009).
- ²³³C. Masciovecchio, G. Ruocco, F. Sette, M. Krisch, R. Verbeni, U. Bergmann, and M. Soltwisch, "Observation of large momentum phononlike modes in glasses," *Phys. Rev. Lett.* **76**, 3356–3359 (1996).
- ²³⁴O. Karnbach, P. G. Heighway, D. McGonegle, R. E. Rudd, G. Gregori, and J. S. Wark, "Molecular dynamics simulations of inelastic x-ray scattering from shocked copper," *J. Appl. Phys.* **130**, 125901 (2021).
- ²³⁵P. Mason, M. Divoký, K. Ertel, J. Pilař, T. Butcher, M. Hanuš, S. Banerjee, J. Phillips, J. Smith, M. De Vido, A. Lucianetti, C. Hernandez-Gomez, C. Edwards, T. Mocek, and J. Collier, "Kilowatt average power 100 J-level diode pumped solid state laser," *Optica* **4**, 438 (2017).
- ²³⁶G. W. Lee, W. J. Evans, and C.-S. Yoo, "Crystallization of water in a dynamic diamond-anvil cell: Evidence for ice VII-like local order in supercompressed water," *Phys. Rev. B* **74**, 134112 (2006).
- ²³⁷A. E. Gleason, C. A. Bolme, E. Galtier, H. J. Lee, E. Granados, D. H. Dolan, C. T. Seagle, T. Ao, S. Ali, A. Lazicki, D. Swift, P. Celliers, and W. L. Mao, "Compression freezing kinetics of water to ice VII," *Phys. Rev. Lett.* **119**, 025701 (2017).
- ²³⁸D. H. Dolan, M. D. Knudson, C. A. Hall, and C. Deeney, "A metastable limit for compressed liquid–water," *Nat. Phys.* **3**, 339–342 (2007).
- ²³⁹M. C. Marshall, M. Millot, D. E. Fratanduono, D. M. Sterbentz, P. C. Myint, J. L. Belof, Y.-J. Kim, F. Coppari, S. J. Ali, J. H. Eggert, R. F. Smith, and J. M. McNaney, "Metastability of liquid water freezing into ice VII under dynamic compression," *Phys. Rev. Lett.* **127**, 135701 (2021).
- ²⁴⁰Y. Katayama, T. Mizutani, W. Utsumi, O. Shimomura, M. Yamakata, and K.-I. Funakoshi, "A first-order liquid-liquid phase transition in phosphorus," *Nature* **403**, 170–173 (2000).
- ²⁴¹V. V. Brazhkin, S. V. Popova, and R. N. Voloshin, "High-pressure transformations in simple melts," *High Pressure Res.* **15**, 267–305 (1997).
- ²⁴²J. H. Eggert, G. Weck, P. Loubeyre, and M. Mezouar, "Quantitative structure factor and density measurements of high-pressure fluids in diamond anvil cells by x-ray diffraction: Argon and water," *Phys. Rev. B* **65**, 174105 (2002).
- ²⁴³A. Cadien, Q. Y. Hu, Y. Meng, Y. Q. Cheng, M. W. Chen, J. F. Shu, H. K. Mao, and H. W. Sheng, "First-order liquid-liquid phase transition in cerium," *Phys. Rev. Lett.* **110**, 125503 (2013).
- ²⁴⁴D. A. Keen, "Total scattering and the pair distribution function in crystallography," *Crystallogr. Rev.* **26**, 141–199 (2020).
- ²⁴⁵N. J. Hartley, J. Vorberger, T. Döppner, T. Cowan, R. W. Falcone, L. B. Fletcher, S. Frydrych, E. Galtier, E. J. Gamboa, D. O. Gericke, S. H. Glenzer, E. Granados, M. J. MacDonald, A. J. MacKinnon, E. E. McBride, I. Nam, P. Neumayer, A. Pak, K. Rohatsch, A. M. Saunders, A. K. Schuster, P. Sun, T. van Driel, and D. Kraus, "Liquid structure of shock-compressed hydrocarbons at megabar pressures," *Phys. Rev. Lett.* **121**, 245501 (2018).

- ²⁴⁶G. Morard, J.-A. Hernandez, M. Guarguaglini, R. Bolis, A. Benuzzi-Mounaix, T. Vinci, G. Fiquet, M. A. Baron, S. H. Shim, B. Ko, A. E. Gleason, W. L. Mao, R. Alonso-Mori, H. J. Lee, B. Nagler, E. Galtier, D. Sokaras, S. H. Glenzer, D. Andrault, G. Garbarino, M. Mezouar, A. K. Schuster, and A. Ravasio, "In situ x-ray diffraction of silicate liquids and glasses under dynamic and static compression to megabar pressures," *Proc. Natl. Acad. Sci. U.S.A.* **117**, 11981 (2020).
- ²⁴⁷O. Narygina, E. E. McBride, G. W. Stinton, and M. I. McMahon, "Melting curve of potassium to 22 GPa," *Phys. Rev. B* **84**, 054111 (2011).
- ²⁴⁸F. Seiboth, L. B. Fletcher, D. McGonegle, S. Anzellini, L. E. Dresselhaus-Cooper, M. Frost, E. Galtier, S. Goede, M. Harmand, H. J. Lee, A. L. Levitan, K. Miyanishi, B. Nagler, I. Nam, N. Ozaki, M. Rödel, A. Schropp, C. Spindloe, P. Sun, J. S. Wark, J. Hastings, S. H. Glenzer, and E. E. McBride, "Simultaneous 8.2 keV phase-contrast imaging and 24.6 keV x-ray diffraction from shock-compressed matter at the LCLS," *Appl. Phys. Lett.* **112**, 221907 (2018).
- ²⁴⁹P. S. DeCarli and J. C. Jamieson, "Formation of diamond by explosive shock," *Science* **133**, 1821–1822 (1961).
- ²⁵⁰R. E. Hanneman, H. M. Strong, and F. P. Bundy, "Hexagonal diamonds in meteorites: Implications," *Science* **155**, 995–997 (1967).
- ²⁵¹F. P. Bundy and J. S. Kasper, "Hexagonal diamond—A new form of carbon," *J. Chem. Phys.* **46**, 3437–3446 (1967).
- ²⁵²C. Frondel and U. B. Marvin, "Lonsdaleite, a hexagonal polymorph of diamond," *Nature* **214**, 587–589 (1967).
- ²⁵³S. Fujihara, K. Narita, Y. Saito, K. Tatsumoto, S. Fujiwara, M. Yoshida, K. Aoki, Y. Kakudate, S. Usuba, and H. Yamawaki, "Explosive shock synthesis of polycrystalline diamond powders," in *Shock Waves*, edited by K. Takayama (Springer, Berlin, 1992), pp. 367–372.
- ²⁵⁴T. Komatsu, M. Samedima, T. Awano, Y. Kakadate, and S. Fujiwara, "Creation of superhard B–C–N heterodiamond using an advanced shock wave compression technology," *J. Mater. Process. Technol.* **85**, 69–73 (1999).
- ²⁵⁵*Modern Methods of Crystal Structure Prediction*, edited by A. Oganov (John Wiley & Sons, Ltd, 2010).
- ²⁵⁶J. Wentorf and R. H. J. S. Kasper, "Two new forms of silicon," *Science* **139**, 338–339 (1963).
- ²⁵⁷R. J. Nelmes, M. I. McMahon, N. G. Wright, D. R. Allan, and J. S. Loveday, "Stability and crystal-structure of BC8 germanium," *Phys. Rev. B* **48**, 9883–9886 (1993).
- ²⁵⁸R. Biswas, R. M. Martin, R. J. Needs, and O. H. Nielsen, "Complex tetrahedral structures of silicon and carbon under pressure," *Phys. Rev. B* **30**, 3210–3213 (1984).
- ²⁵⁹R. Biswas, R. M. Martin, R. J. Needs, and O. H. Nielsen, "Stability and electronic properties of complex structures of silicon and carbon under pressure: Density-functional calculations," *Phys. Rev. B* **35**, 9559 (1987).
- ²⁶⁰N. Madhusudhan, K. K. M. Lee, and O. Mousis, "A possible carbon-rich interior in Super-Earth 55 Cancri e," *Astrophys. J.* **759**, L40 (2012).
- ²⁶¹N. Mashian and A. Loeb, "CEMP stars: Possible hosts to carbon planets in the early universe," *Mon. Not. R. Astron. Soc.* **460**, 2482–2491 (2016).
- ²⁶²C. Mailhot and A. K. McMahan, "Atmospheric-pressure stability of energetic phases of carbon," *Phys. Rev. B* **44**, 11578–11591 (1991).
- ²⁶³B. Haberl, T. A. Strobel, and J. E. Bradby, "Pathways to exotic metastable silicon allotropes," *Appl. Phys. Rev.* **3**, 040808 (2016).
- ²⁶⁴A. R. Oganov, C. J. Pickard, Q. Zhu, and R. J. Needs, "Structure prediction drives materials discovery," *Nat. Rev. Mater.* **4**, 331–348 (2019).
- ²⁶⁵M. Martinez-Canales, C. J. Pickard, and R. J. Needs, "Thermodynamically stable phases of carbon at multiterapascal pressures," *Phys. Rev. Lett.* **108**, 045704 (2012).
- ²⁶⁶C. J. Pickard and R. J. Needs, "Aluminium at terapascal pressures," *Nat. Mater.* **9**, 624–627 (2010).
- ²⁶⁷C. He, X. Shi, S. J. Clark, J. Li, C. J. Pickard, T. Ouyang, C. Zhang, C. Tang, and J. Zhong, "Complex low energy tetrahedral polymorphs of group IV elements from first principles," *Phys. Rev. Lett.* **121**, 175701 (2018).
- ²⁶⁸J. Coakley, A. Higginbotham, D. McGonegle, J. Ilavsky, T. D. Swinburne, J. S. Wark, K. M. Rahman, V. A. Vorontsov, D. Dye, T. J. Lane, S. Boutet, J. Koglin, J. Robinson, and D. Milathianaki, "Femtosecond quantification of void evolution during rapid material failure," *Sci. Adv.* **6**, eabb4434 (2020).
- ²⁶⁹B. E. Warren, *X-Ray Diffraction* (Dover Publications, Inc., New York, 1990).
- ²⁷⁰K. Rosolankova, J. S. Wark, E. M. Bringa, and J. Hawreliak, "Measuring stacking fault densities in shock-compressed FCC crystals using in situ x-ray diffraction," *J. Phys.: Condens. Matter* **18**, 6749–6757 (2006).
- ²⁷¹A. E. Gleason, C. A. Bolme, H. J. Lee, B. Nagler, E. Galtier, D. Milathianaki, J. Hawreliak, R. G. Kraus, J. H. Eggert, D. E. Fratanduono, G. W. Collins, R. Sandberg, W. Yang, and W. L. Mao, "Ultrafast visualization of crystallization and grain growth in shock-compressed SiO₂," *Nat. Commun.* **6**, 8191 (2015).
- ²⁷²J. Nuckolls, L. Wood, A. Thiessen, and G. Zimmerman, "Laser compression of matter to super-high densities: Thermonuclear (CTR) applications," *Nature* **239**, 139–142 (1972).
- ²⁷³T. Döppner, D. C. Swift, A. L. Kritcher, B. Bachmann, G. W. Collins, D. A. Chapman, J. Hawreliak, D. Kraus, J. Nilsen, S. Rothman, L. X. Benedict, E. Dewald, D. E. Fratanduono, J. A. Gaffney, S. H. Glenzer, S. Hamel, O. L. Landen, H. J. Lee, S. LePape, T. Ma, M. J. MacDonald, A. G. MacPhee, D. Milathianaki, M. Millot, P. Neumayer, P. A. Sterne, R. Tommasini, and R. W. Falcone, "Absolute equation-of-state measurement for polystyrene from 25 to 60 mbar using a spherically converging shock wave," *Phys. Rev. Lett.* **121**, 025001 (2018).
- ²⁷⁴A. L. Kritcher, D. C. Swift, T. Döppner, B. Bachmann, L. X. Benedict, G. W. Collins, J. L. DuBois, F. Elsner, G. Fontaine, J. A. Gaffney, S. Hamel, A. Lazicki, W. R. Johnson, N. Kostinski, D. Kraus, M. J. MacDonald, B. Maddox, M. E. Martin, P. Neumayer, A. Nikroo, J. Nilsen, B. A. Remington, D. Saumon, P. A. Sterne, W. Sweet, A. A. Correa, H. D. Whitley, R. W. Falcone, and S. H. Glenzer, "A measurement of the equation of state of carbon envelopes of white dwarfs," *Nature* **584**, 51–54 (2020).
- ²⁷⁵D. E. Fratanduono, R. F. Smith, S. J. Ali, D. G. Braun, A. Fernandez-Pañella, S. Zhang, R. G. Kraus, F. Coppari, J. M. McNaney, M. C. Marshall, L. E. Kirch, D. C. Swift, M. Millot, J. K. Wicks, and J. H. Eggert, "Probing the solid phase of noble metal copper at terapascal conditions," *Phys. Rev. Lett.* **124**, 015701 (2020).
- ²⁷⁶D. E. Fratanduono, M. Millot, D. G. Braun, S. J. Ali, A. F.-P. nella, C. T. Seagle, J.-P. Davis, J. L. Brown, Y. Akahama, R. G. Kraus, M. C. Marshall, R. F. Smith, E. F. O'Bannon, J. M. McNaney, and J. H. Eggert, "Establishing gold and platinum standards to 1 terapascal using shockless compression," *Science* **372**, 1063–1068 (2021).
- ²⁷⁷J. Tan, Z. Jian, S. Xiao, X. Li, K. Wang, L. Wang, B. Huang, H. Deng, W. Zhu, and W. Hu, "The mechanism of plasticity and phase transition in iron single crystals under cylindrically divergent shock loading," *Int. J. Mech. Sci.* **217**, 107032 (2021).
- ²⁷⁸N. F. Mott, "Review lecture: Metal-insulator transitions," *Proc. R. Soc. London, Ser. A* **382**, 1–24 (1982).
- ²⁷⁹Y. Ma, M. Eremets, A. R. Oganov, Y. Xie, I. Trojan, S. Medvedev, A. O. Lyakhov, M. Valle, and V. Prakapenka, "Transparent dense sodium," *Nature* **458**, 182–U3 (2009).
- ²⁸⁰O. S. Humphries, R. S. Marjoribanks, Q. Y. van den Berg, E. C. Galtier, M. F. Kasim, H. J. Lee, A. J. F. Miskampbell, B. Nagler, R. Royle, J. S. Wark, and S. M. Vinko, "Probing the electronic structure of warm dense nickel via resonant inelastic x-ray scattering," *Phys. Rev. Lett.* **125**, 195001 (2020).
- ²⁸¹L. B. Fletcher, H. J. Lee, T. Döppner, E. Galtier, B. Nagler, P. Heimann, C. Fortmann, S. LePape, T. Ma, M. Millot, A. Pak, D. Turnbull, D. A. Chapman, D. O. Gericke, J. Vorberger, T. White, G. Gregori, M. Wei, B. Barbrel, R. W. Falcone, C. C. Kao, H. Nuhn, J. Welch, U. Zastrau, P. Neumayer, J. B. Hastings, and S. H. Glenzer, "Ultrabright x-ray laser scattering for dynamic warm dense matter physics," *Nat. Photonics* **9**, 274–279 (2015).
- ²⁸²K. Voigt, M. Zhang, K. Ramakrishna, A. Amouretti, K. Appel, E. Brambrink, V. Cerantola, D. Chekrygina, T. Döppner, R. W. Falcone, K. Falk, L. B. Fletcher, D. O. Gericke, S. Göde, M. Harmand, N. J. Hartley, S. P. Hau-Riege, L. G. Huang, O. S. Humphries, M. Lokamani, M. Makita, A. Pelka, C. Prescher, A. K. Schuster, M. Šmid, T. Toncian, J. Vorberger, U. Zastrau, T. R. Preston, and

D. Kraus, "Demonstration of an x-ray Raman spectroscopy setup to study warm dense carbon at the high energy density instrument of European XFEL," *Phys. Plasmas* **28**, 082701 (2021).

²⁸³T. Preston, S. Göde, J.-P. Schwinkendorf, K. Appel, E. Brambrink, V. Cerantola, H. Höppner, M. Makita, A. Pelka, C. Prescher, K. Sukharnikov, A. Schmidt, I. Thorpe, T. Toncian, A. Amouretti, D. Chekrygina, R. Falcone, K. Falk, L. Fletcher, E. Galtier, M. Harmand, N. Hartley, S. Hau-Riege, P. Heimann, L. Huang, O. Humphries, O. Karnbach, D. Kraus, H. Lee, B. Nagler, S. Ren, A. Schuster, M. Smid, K. Voigt, M. Zhang, and U. Zastra, "Design and performance characterisation of the HAPG von Hámos spectrometer at the high energy density instrument of the European XFEL," *J. Instrum.* **15**, P11033 (2020).

²⁸⁴R. Kidder, "Hot-electron preheat of laser-driven targets," *Nucl. Fusion* **21**, 145–151 (1981).

²⁸⁵C. Emma, A. Lutman, M. W. Guetg, J. Krzywinski, A. Marinelli, J. Wu, and C. Pelle, "Experimental demonstration of fresh bunch self-seeding in an x-ray free electron laser," *Appl. Phys. Lett.* **110**, 154101 (2017).

²⁸⁶F.-J. Decker *et al.*, "Four X-ray pulses within 10 ns at LCLS," in *Proceedings of 10th International Particle Accelerator Conference (IPAC'19), Melbourne, Australia, 19–24 May 2019*, International Particle Accelerator Conference No. 10 (JACoW Publishing, Geneva, 2019), pp. 1859–1862.

²⁸⁷Y.-W. Sun, F.-J. Decker, J. Turner, S.-H. Song, A. Robert, and D.-L. Zhu, "Pulse intensity characterization of the LCLS nanosecond double-bunch mode of operation," *J. Synchrotron Radiat.* **25**, 242–249 (2018).

²⁸⁸P. Hart, A. Carpenter, L. Claus, D. Damiani, M. Dayton, F.-J. Decker, A. Gleason, P. Heimann, E. Hurd, E. McBride, S. Nelson, M. Sanchez, S.-H. Song, and D.-L. Zhu, "First x-ray test of the Icarus nanosecond-gated camera," *Proc. SPIE* **11038**, 110380Q (2019).